SEISMIC RISK ASSESSMENT OF AN INSTRUMENTED REINFORCED CONCRETE BUILDING

A THESIS SUBMITTED TO
THE GRADUATE SCHOOL OF NATURAL AND APPLIED SCIENCES
OF
MIDDLE EAST TECHNICAL UNIVERSITY

BY

FURKAN PAÇARIZI

IN PARTIAL FULFILLMENT OF THE REQUIREMENTS
FOR
THE DEGREE OF MASTER OF SCIENCE
IN
CIVIL ENGINEERING

NOVEMBER 2022

Approval of the thesis:

THESIS TITLE

submitted by **FURKAN PAÇARIZI** in partial fulfillment of the requirements for the degree of **Master of Science in Civil Engineering, Middle East Technical University** by,

Prof. Dr. Halil Kalıpçılar
Dean, Graduate School of **Natural and Applied Sciences** _____

Prof. Dr. Erdem Canbay
Head of the Department, **Civil Engineering** _____

Assoc. Prof. Dr. Ozan Cem Çelik
Supervisor, **Civil Engineering, METU** _____

Examining Committee Members:

Prof. Dr. Kağan Tuncay
Civil Engineering, METU _____

Assoc. Prof. Dr. Ozan Cem Çelik
Civil Engineering, METU _____

Prof. Dr. Yalın Arıcı
Civil Engineering, METU _____

Prof. Dr. Murat Altuğ Erberik
Civil Engineering, METU _____

Assist. Prof. Dr. Berat Feyza Soysal Albostan
Civil Engineering, Cankaya University _____

Date: 25.11.2022

I hereby declare that all information in this document has been obtained and presented in accordance with academic rules and ethical conduct. I also declare that, as required by these rules and conduct, I have fully cited and referenced all material and results that are not original to this work.

Name, Last name: Furkan Paçarizi

Signature:

ABSTRACT

SEISMIC RISK ASSESSMENT OF AN INSTRUMENTED REINFORCED CONCRETE BUILDING

Paçarizi, Furkan
Master of Science, Civil Engineering
Supervisor: Assoc. Prof. Dr. Ozan Cem Çelik

November 2022, 114 pages

The expected seismic performance of existing buildings during future earthquakes is always a concern for public administrations in pre- and post-earthquake planning as well as for general public. Seismic risk of these buildings, whether they will fulfill different performance-based design objectives when subjected to earthquake ground motions of different intensities, has to be evaluated. Such an evaluation for an existing building requires an accurate finite element model of the building. This study focuses on the first instrumented building in Turkey, for which the ambient and forced vibration test results are available to validate its finite element model. This reinforced concrete building is in close proximity to the North Anatolian Fault in Gerede, Bolu. Having survived the 1999 M_w 7.1 Duzce earthquake, the building was retrofitted in 2009 after the implementation of the 2007 Turkish Earthquake Code. The finite element models that incorporate the infill walls were developed for both the as-built and post-refrofit states of the building, and updated to reproduce the in-situ dynamic properties. Using these models, seismic risk assessments for both states of the building were performed according to the past and current building codes in Turkey. The demonstrated inadequate performance of the as-built building verified the need for the retrofit of the building. However, the post-retrofit building did not satisfy the performance objectives stated in the current building codes.

Keywords: In-Situ Dynamic Tests, Seismic Risk Assessment

ÖZ

CİHAZLANDIRILMIŞ BETONARME BİR BİNANIN SİSMİK RİSK DEĞERLENDİRMESİ

Paçarizi, Furkan
Yüksek Lisans, İnşaat Mühendisliği
Tez Yöneticisi: Doç. Dr. Ozan Cem Çelik

Kasım 2022, 114 sayfa

Gelecekteki depremler sırasında mevcut binaların beklenen sismik performansı, deprem öncesi ve sonrası planlamada kamu idarelerinin yanı sıra genel halkı da her zaman ilgilendirmektedir. Bu binaların sismik riskleri, farklı büyüklükteki deprem yer hareketlerine maruz kaldıklarında farklı performansa dayalı tasarım hedeflerini yerine getirip getiremeyecekleri, değerlendirilmelidir. Mevcut bir bina için böyle bir değerlendirme, binanın doğru bir sonlu eleman modelini gerektirir. Bu çalışma, Türkiye'nin cihazlandırılmış ilk binasına odaklanmaktadır. Binanın mevcut çevresel ve zorlamalı titreşim test sonuçları, sonlu eleman modelini doğrulamakta kullanılmıştır. Bina, Bolu Gerede'de Kuzey Anadolu Fayı'na yakın konumdadır. 1999 M_w 7,1 Düzce depremini atlatan bina, 2007 Türkiye Deprem Yönetmeliği'nin yürürlüğe girmesinden sonra 2009 yılında güçlendirilmiştir. Binanın dolgu duvarları içeren sonlu eleman modelleri, hem inşa edilmiş hem de güçlendirme sonrası durum için geliştirilmiş ve tespit edilen dinamik özellikleri verecek şekilde güncellenmiştir. Bu modeller kullanılarak, binanın her iki durumu için Türkiye'deki eski ve yeni yapı yönetmeliklerine göre sismik risk değerlendirmesi yapılmıştır. Binanın inşa edilmiş halinin gösterdiği yetersiz performans, binanın güçlendirme ihtiyacını doğrulamıştır. Ancak güçlendirilmiş bina, mevcut bina yönetmeliklerinde belirtilen performans hedeflerini karşılamamaktadır.

Anahtar Kelimeler: Dinamik Testler, Sismik Risk Değerlendirmesi

To my family,

ACKNOWLEDGMENTS

I would like to extend my deepest respect and thanks to my supervisor Dr. Ozan Cem Çelik for his guidance, advice, criticism, encouragement, and insight throughout the research.

I would also like to thank the other thesis examining committee members, Dr. Kağan Tuncay, Dr. Yalın Arıcı, Dr. Murat Altuğ Erberik and Dr. Berat Feyza Soysal Albostan for their insights and valuable suggestions.

I thank Celil Orak, Engin Ege Yormaz, Oğuzhan Gümüş and Ismayil Asgarov for their support. Their contribution to my motivation was undeniable.

To my sisters, Onur and Esra, thank you for your love, support, and unwavering belief in me.

I thank my niece Serra and my nephew Halis for their unconditional and innocent love.

I also thank my wife, Elif, who has always been there for me, giving me support, encouragement, love and constant support, for all the late nights and early mornings, and for keeping me sane over the past few months. Thank you for being my muse.

Finally, I wish to express my most profound appreciation to the most special people in my life, my father Fikret Paçarizi and my mother Birsen Paçarizi. They always have been by my side unconditionally and supported my success with their prayers. Without you, I would not be the person I am today. I believe they deserve this diploma more than me and I dedicate it to them.

TABLE OF CONTENTS

LIST OF TABLES

TABLES

LIST OF FIGURES

FIGURES

CHAPTER 1

INTRODUCTION

1.1 Background

Preventing the destructive effects of earthquakes on the built environment is the foremost aim of the field of earthquake engineering. Following a series of disastrous earthquakes, particularly those that affected densely populated areas, the expected seismic performance of existing buildings during future earthquakes has been more of a concern year after year. Seismic risk of these buildings, whether they will fulfill different performance-based design objectives when subjected to earthquake ground motions of different intensities, has to be evaluated. Seismic risk assessment procedures in building codes mostly require an analytical model of the building under investigation to quantify the level and distribution of damage that may occur in a building under those earthquake events. It is challenging to develop an accurate analytical model for existing buildings, in which stiffness and mass properties are correctly modeled. Hence, detailed information about the building is sought after.

In Turkey, seismic risk assessment methods for existing structures were first included in the 2007 Turkish Earthquake Code [MPWS 2007]. Linear elastic and nonlinear methods were introduced. Recently, the new Turkish Building Earthquake Code [AFAD 2018] has introduced more elaborate versions of these methods. Draft version of a separate document also exists for use in identifying risky buildings within the scope of the Law on Transformation of Areas under Disaster Risks [MEUCC 2021].

The seismic risk assessment of a reinforced concrete (RC) building in Gerede, Bolu is conducted in this study. The building is of particular significance. It is the first permanently instrumented building in Turkey. Middle East Technical University

instrumented the building in 1994 to record its structural response during earthquakes that would originate in the nearby North Anatolian Fault [Gulkan et al. 1994]. Having survived the 1999 M_w 7.1 Duzce earthquake, the building was retrofitted in 2009 following the implementation of the 2007 Turkish Earthquake Code. Ambient and forced vibration test records of the building are available for the as-built and post-retrofit states of the building, respectively.

1.2 Objective and Scope

The objective of this study is to evaluate the retrofit decision of a RC building near a major fault by utilizing its in-situ vibration test data in code-based seismic risk assessment. The critical steps are as listed below:

1. Develop finite element models for the as-built and post-retrofit states of the building and update these models using the in-situ dynamic test records.
2. Perform seismic risk assessment of the as-built building using rapid and linear assessment methods per building codes.
3. Perform linear and nonlinear seismic risk assessments of the post-retrofit building per building codes.

1.3 Outline

This chapter has presented the context of the research that will be addressed in the subsequent chapters.

Chapter 2 presents the previous research on in-situ dynamic tests with a particular focus on infill wall modeling.

Chapter 3 develops the three-dimensional (3-D) finite element models of the building for its as-built and post-retrofit states and updates these models using the in-situ vibration test data.

Chapter 4 performs seismic risk assessments for the as-built and post-retrofit states of the building per building codes.

Finally, Chapter 5 presents a summary of the research, conclusions drawn from this study and suggested future research.

CHAPTER 2

LITERATURE REVIEW

2.1 Introduction

This chapter presents previous research studies on in-situ dynamic tests with a particular focus on infill wall modeling. Finite element model calibration based on in-situ dynamic tests are also included.

2.2 In-Situ Dynamic Tests and Infill Wall Modeling

It is crucial to determine the dynamic properties of the buildings, such as natural vibration periods and mode shapes, to have a better understanding of the prediction of the structural response during an earthquake. Finite element models are used to predict these properties during the design phase. These finite element models are then used to simulate the building responses to different dynamic loads (e.g., strong earthquake shaking, strong winds, forced vibration, blast). The dynamic properties (for validating the finite element models) are often identified via forced or ambient vibration tests [Hudson 1970; Trifunac and Todorovska 1999; Beolchini and Vestroni 1997; Vestroni et al. 1996]. In ambient vibration testing, small amplitude vibrations mainly due to wind excitations are recorded. In forced vibration testing, the excitation is provided by a vibration generator mounted on the building. Identified dynamic properties, such as natural vibration periods and mode shapes, from in-situ dynamic tests can be used to validate and update the finite element models that will be used in seismic risk assessment of buildings.

The stiffness and strength of buildings are known to be impacted by infill walls. It is not always safe to neglect the infill wall interaction under earthquake events since the infill walls behave as diagonal struts under lateral loads, drastically increasing

the stiffness. This could change the seismic demand due to a significant decrease in the natural period of the building [El-Dakhakhni et al. 2003; 2006]. On the other hand, common justification for neglecting infill walls in structural analysis is that infill walls crack well below design level lateral loads and do not contribute to the stiffness of the building [Hashemi and Mosalam 2007; Asteris et al. 2011].

The most extensively studied instrumented building to date is Millikan Library in Pasadena, California, which has been monitored since its completion in 1967 [Clinton et al. 2006]. In the lifespan of the building, its natural vibration frequencies were identified from the recorded structural responses during strong and minor earthquake events, forced vibration tests and different weather (wind, rain, temperature) conditions. The building is a nine-story RC building with a rectangular footprint, 22.9 m along the E-W direction and 21.0 m along the N-S direction. The structural system of the building consists of moment frames and core shear walls in the E-W direction and shear walls in the N-S direction. The building is currently instrumented with 36 channels of accelerometers. The fundamental natural frequencies, as identified by forced vibration testing in 1967, were 1.45 Hz and 1.90 Hz in the E-W and N-S directions, respectively. Based on all historical data — forced vibration, ambient vibration, and strong ground motion records — the fundamental natural frequencies permanently decreased by 22% in the E-W direction and 12% in the N-S direction throughout its 36-year lifespan. Because the building mass was not changed considerably over time, this reduction in natural frequency indicates a large decrease in building stiffness. The M_w 6.1 Whittier Narrows earthquake in 1987 and the M_w 6.6 San Fernando earthquake in 1971 were the primary causes of these permanent changes in natural frequencies; the variations in natural frequencies caused by the weather conditions were temporary.

Genes et al. [2008] performed forced vibration tests on two eight-story RC frame buildings. These residential buildings have rectangular footprints, 30.7 m by 14.3 m and 30.0 m by 19.0 m. The structural systems consist of shear walls in both directions. The interior and exterior walls were constructed using hollow clay bricks. Both buildings were instrumented with 12 uniaxial accelerometers. The fundamental

natural vibration periods of the first building were identified as 0.51 s and 0.42 s in the N-S and E-W directions, respectively. For the second building, the fundamental natural vibration periods were identified as 0.36 s and 0.45 s in the N-S and E-W directions, respectively. Two 3-D finite element models were developed for each building. Only the mass of infill walls was considered in the first models, whereas the stiffness of infill walls was also considered by modeling them using compression struts in the second models. The fundamental periods for the first building were reduced from 0.76 s to 0.55 s in the N-S direction and from 0.61 s to 0.36 s in the E-W direction when infill walls were incorporated. Likewise, the fundamental periods for the second building were reduced from 0.48 s to 0.38 s in the N-S direction and from 0.48 s to 0.41 s in the E-W direction. For both buildings, when infill walls were modeled using compression struts, the fundamental periods were in good agreement with those identified from the forced vibration tests. The mode shapes were also similar, indicating further that infill wall modeling using compression struts is acceptable.

Soyoz et al. [2013] investigated the effects of seismic retrofitting on the dynamic characteristics of a six-story RC building in Istanbul, Turkey. The structural system of the building consisted of moment frames in the E-W and N-S directions and shear walls around the stairs. During the seismic retrofitting, column jacketing was applied and shear walls were added. Ambient vibration tests were performed before, during and after the retrofit. Upon demolishing the partition walls, the fundamental frequency of the building decreased from 2.98 Hz to 2.64 Hz, an 11% reduction, which showed the impact of the partition walls on the overall structural stiffness. The fundamental frequency then increased to 4.69 Hz following the seismic retrofit, a 96% increase. Damping ratios for the first three vibration modes, identified before and after the retrofit, were 0.5–1%. A forced vibration test was also performed after the retrofit. The identified natural frequencies were comparable to those identified from the ambient vibration test. However, the dependency of natural frequencies and damping ratios on the amplitude of the forced excitation was noted. In the finite element model of the building, shear walls and floor slabs were modeled using shell

elements, whereas frame elements were used for the beams and columns. The hollow-brick partition walls were modeled as diagonal struts [Mainstone 1974] and the window and door openings in the partition walls were taken into account using stiffness reduction factors [Asteris 2003]. The natural frequencies for the first three vibration modes that were determined were within 10% of those identified from ambient and forced vibration tests.

Aldemir et al. [2015] performed a forced vibration test on a two-story masonry building. The fundamental natural frequency of the building was identified as 7.97 Hz and this value agreed well with the fundamental frequency determined from the finite element model of the building that was developed using shell elements.

Chaker and Cherifati [1999] tested two adjacent three-story RC frame buildings, a bare frame and a similar frame with hollow clay brick walls. The infilled frame building had a much shorter fundamental period. Its lateral stiffness was found to be seven times that of the bare frame building. First, the finite element model for the bare frame building was developed. The natural frequencies determined from the eigenvalue analysis were in very good agreement with those identified from the experimental data. Using bare frame model as a base model, four finite element models of the infilled frame building were developed. The infill panels were represented by diagonal truss elements in three models and by plane stress isoparametric quadrilateral finite elements in the fourth model. In these three diagonal truss models, the width of the diagonal truss elements was defined per Tahar [1984], Tiruvengadam [1985] and Ciongradi [1983]. The diagonal truss models were not appropriate in reproducing the identified frequencies under small strain conditions, whereas the plane stress model was reasonably accurate.

Pan et al. [2006] performed an ambient vibration test on a 15-story RC residential building. The natural frequencies determined from the finite element model of the building, in which the brick infill walls were modeled and flexible diaphragms were defined, were close to the identified natural frequencies.

Kocak et al. [2008] performed ambient vibration tests on a 12-story RC moment-frame building. The tests were performed before and after the infill walls were constructed, and after they were plastered. Infill walls were incorporated by using diagonal struts in the finite element model. Experimental modulus of elasticity values were used: 3550 MPa for the infill walls without plaster and 6000 MPa for the infill walls with plaster. The natural frequencies determined from the finite element model and those identified from the ambient vibration tests were similar.

Celik [2016] performed a forced vibration test on a two-story RC building. The identified natural frequencies and mode shapes were reproduced with the finite element model that incorporated the infill walls using diagonal struts. To estimate the stiffness of the autoclaved aerated concrete (AAC) infill walls in the elastic range, it was advised to use a greater strut width coefficient (0.38) than in ASCE/SEI 41-06 [ASCE 2007] (0.175). The modulus of elasticity for AAC blocks was taken as 2500 MPa based on the available experimental data. Window and door openings in infill walls were considered by a stiffness reduction factor. Instead of merely comparing the natural frequencies, acceleration-frequency response curves were simulated using steady-state analysis for comparison with those from the forced vibration test. The simulated acceleration-frequency response curves were close to those identified from the forced vibration test.

2.3 Summary

In-situ dynamic tests have revealed the effect of non-structural infill walls on the dynamic characteristics of buildings. According to the above studies, including infill walls in the finite element models as equivalent diagonal struts reduces the fundamental periods by 15–40%. Moreover, in some cases, equivalent strut width coefficient given by the codes underestimated the stiffness of infill walls and this coefficient was calibrated based on the test results. Hence, the finite element models need to incorporate these infill walls for simulations in the linear elastic range. This issue will be addressed subsequently in updating the finite element models of the

instrumented building in this study for its as-built and post-retrofit states based on the available in-situ vibration test data.

CHAPTER 3

MODEL UPDATING OF THE INSTRUMENTED BUILDING

3.1 Introduction

Belkis Sabanci Dormitory is the first permanently instrumented building in Turkey [Gulkan et al. 1994]. It is located in close proximity to the North Anatolian Fault in Gerede (40.7996° N, 32.1859° E), a town with a current population of around 30,000 people located 50 km east of Bolu. This RC building was designed in 1985 in compliance with the 1975 Seismic Regulation of Turkey [MPWS 1975] and the construction was finished in 1988. Middle East Technical University instrumented the building in 1994 to record its structural response during future earthquakes [Gulkan et al. 1994]. Aside from its proximity to an active fault, the building was selected for instrumentation due to its good quality of design and construction. The building survived the 1999 M_w 7.1 Duzce earthquake, with epicenter 84 km away from the building. However, the response of the building to this earthquake was not recorded. No damage was reported. This earthquake was a warning signal for the buildings in the region that they might not survive if an event like the 1944 M_w 7.4 Gerede earthquake should occur. The building was eventually retrofitted in 2009 after the implementation of the 2007 Turkish Earthquake Code [MPWS 2007] and a forced vibration test of the building was performed in 2013 [Celik and Gulkan 2021]. Figure 3.1 shows views of the as-built and post-retrofit states of the building.

(a) (b)

Figure 3.1 View from the SE corner: (a) as-built and (b) post-retrofit buildings [Celik and Gulkan 2021].

3.2 Building Description

3.2.1 As-built properties

The building had originally six stories above ground level and two stories below ground level. The overall height of the building including basement levels was 29.6 m (see Figure 3.2). The story height was 3.6 m. Plan dimensions in the E-W (axis 1 to 9) and N-S (axis A to E) directions were 24.2 m and 23.9 m, respectively (see Figure 3.3). The structural system of the building consisted of RC moment-resisting frames along both the N-S and E-W directions, with 4.2 m long and 0.20 m thick shear walls along the N-S direction at each side of the staircase. Lower basement level B2 had 0.30 m thick peripheral shear walls, while the upper basement level B1 had shear walls only below the main entrance on the north side of the building. Figure 3.4 shows the views of the structural system from the SE and NW corners. The dimensions of the rectangular columns are presented in Table 3.1, whereas the

dimensions of all other columns and shear walls are presented in Figure 3.5. Beam dimensions are provided in Appendix A.

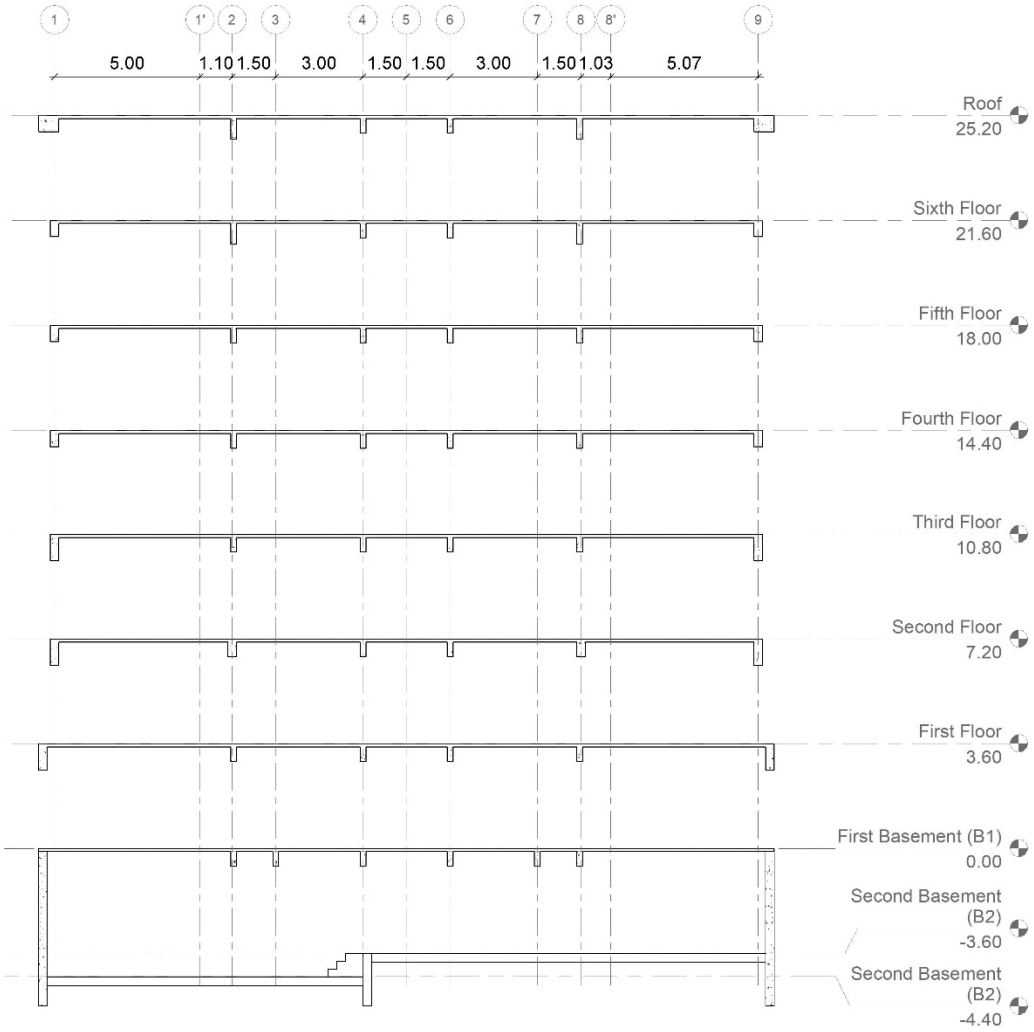

Figure 3.2 Building section A-A (see Figure 3.3; dimensions in m).

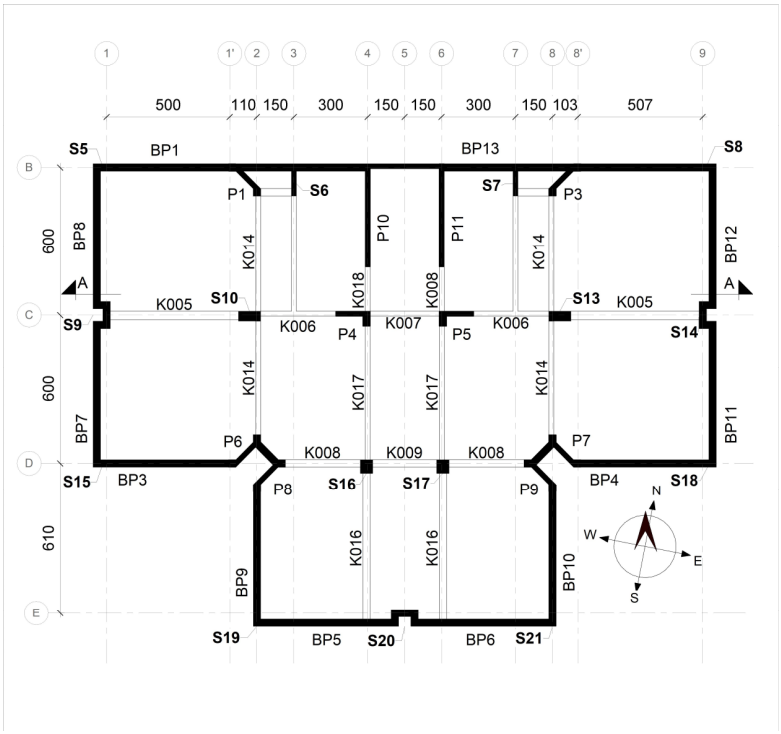

(a) First basement B1

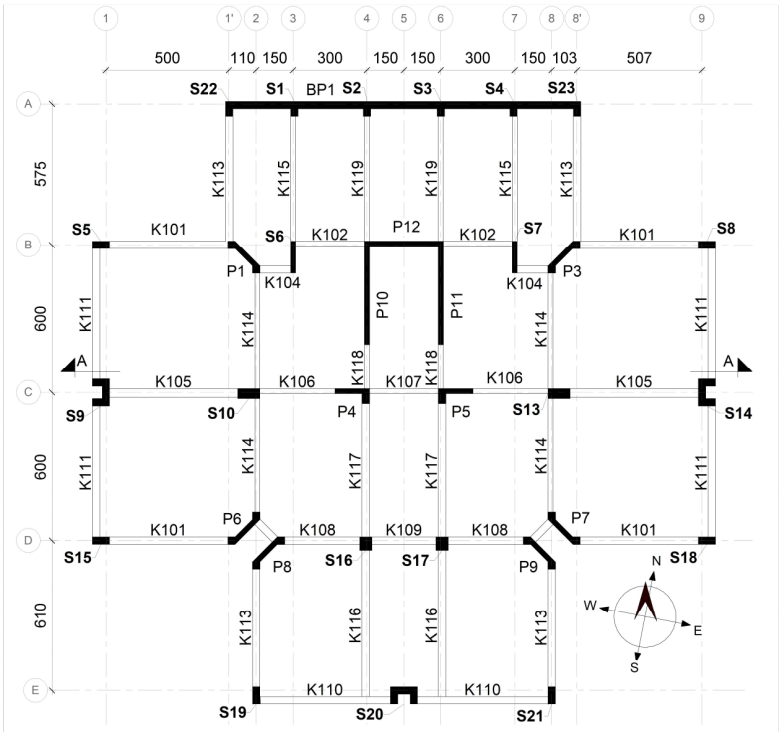

(b) First floor

Figure 3.3 As-built floor plans.

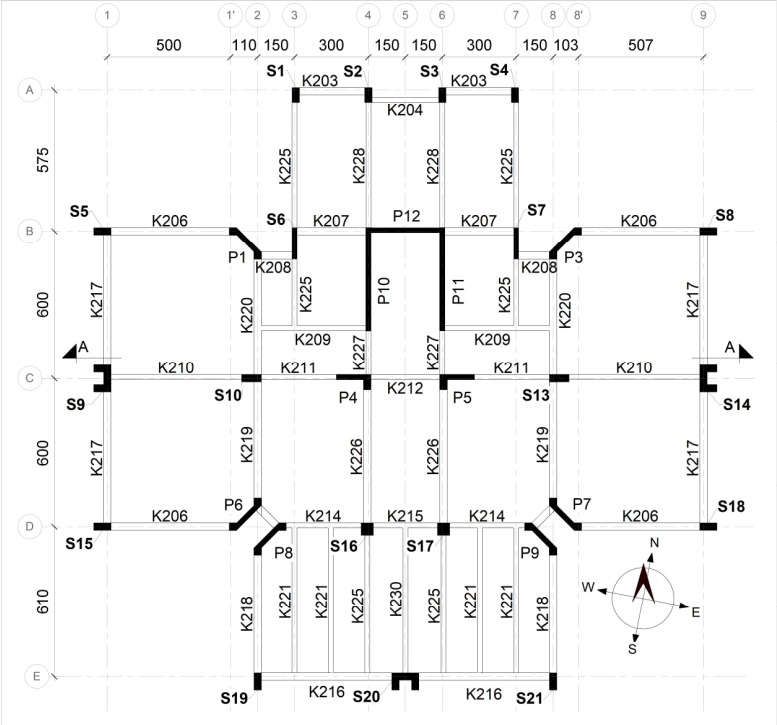

(c) Second floor

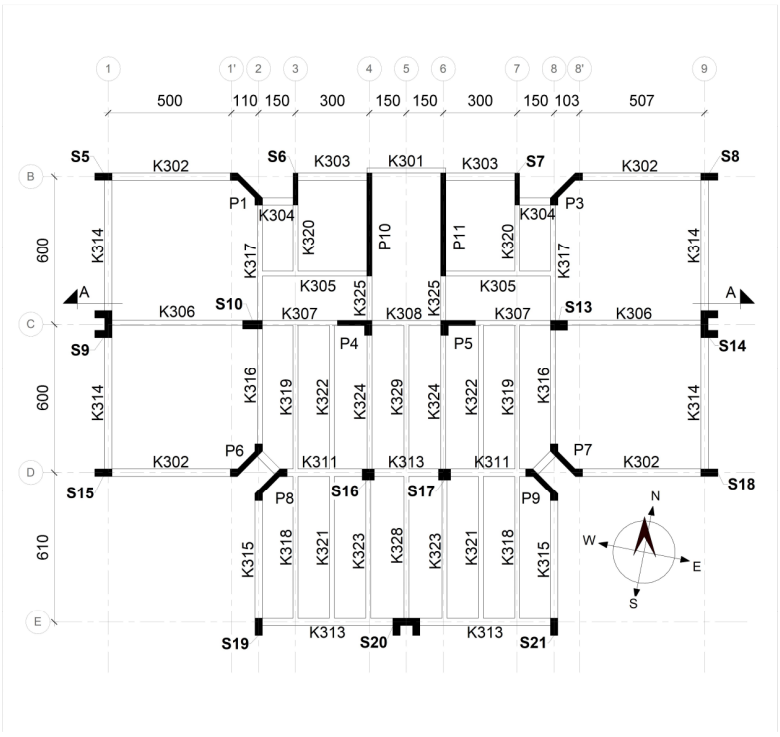

(d) Third floor

Figure 3.3 As-built floor plans (continued).

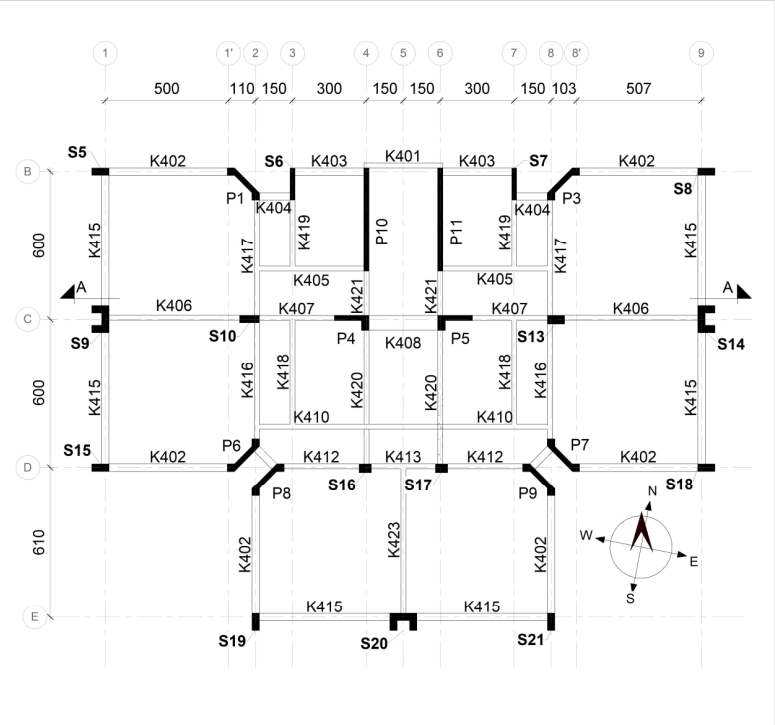

(e) Fourth floor

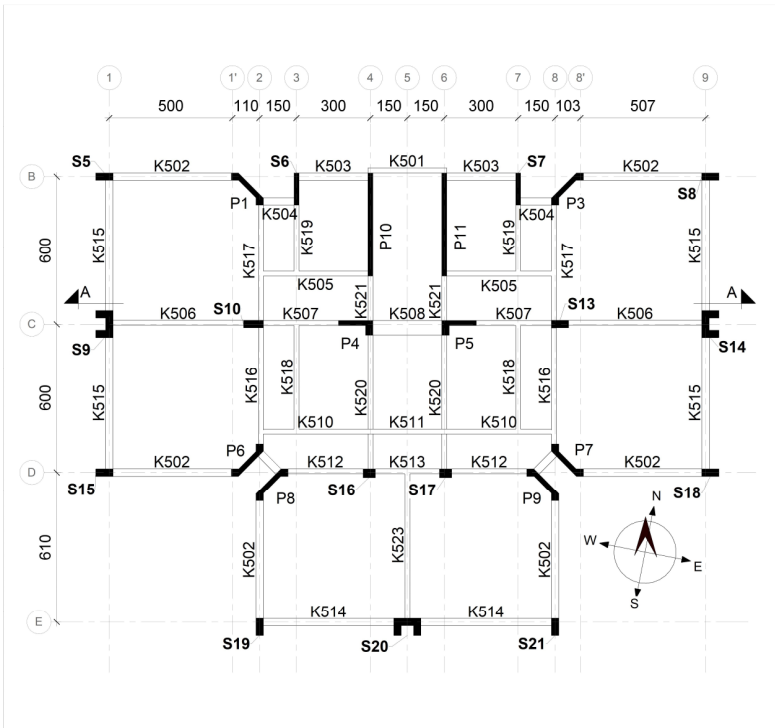

(f) Fifth floor

Figure 3.3 As-built floor plans (continued).

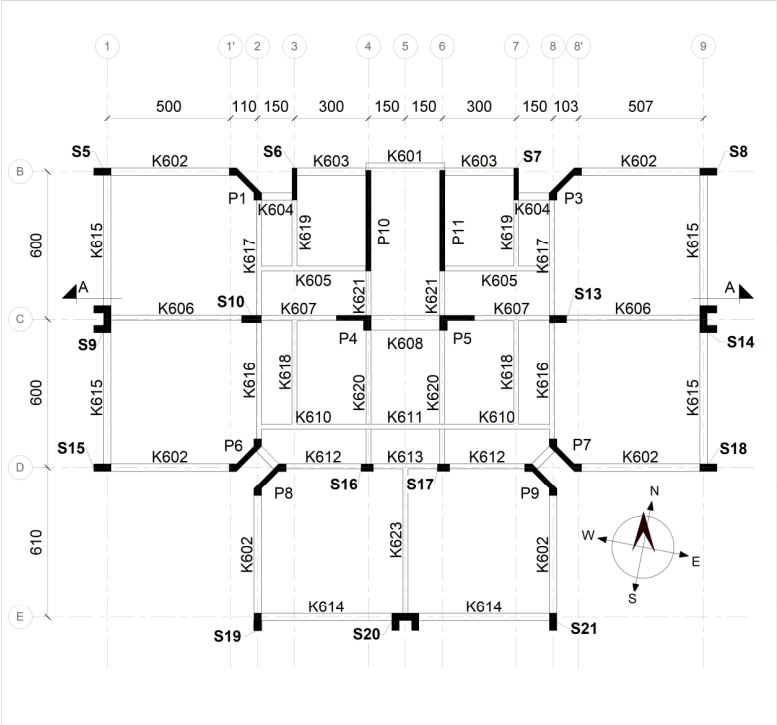

(g) Sixth floor

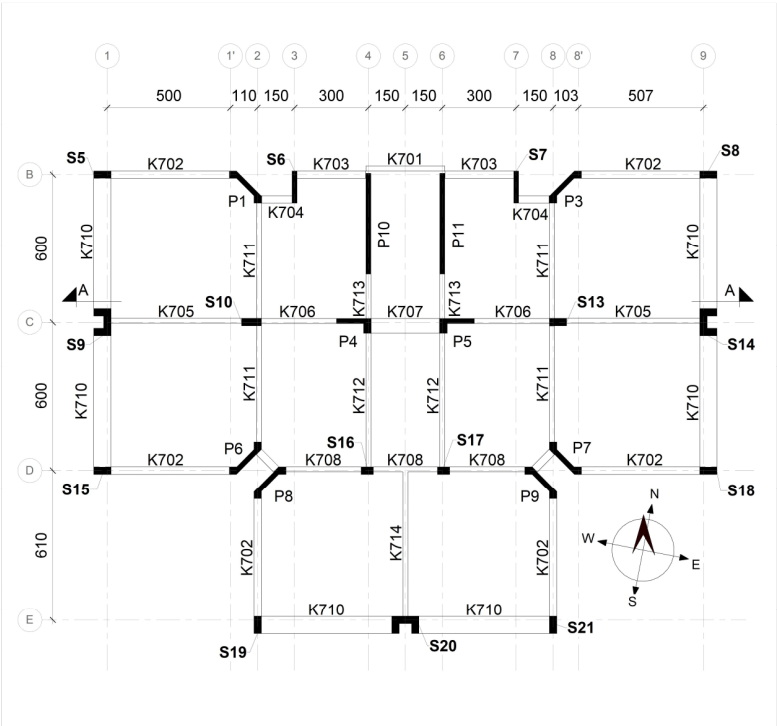

(h) Roof

Figure 3.3 As-built floor plans (continued).

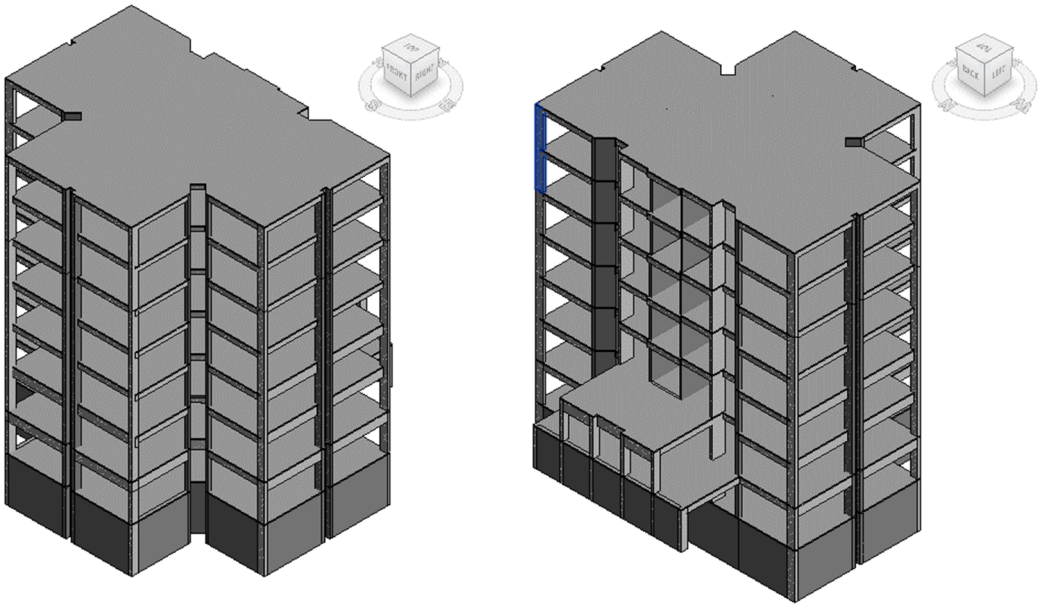

(a) (b)

Figure 3.4 Views of the structural system of the as-built building from the (a) SE and (b) NW corners.

Table 3.1 Rectangular column sizes.

Column ID	Section Dimensions (mm×mm)	Location
S1, S2, S3, S4	300×600	All floors
S5, S8, S15, S18	700×300	All floors
S6, S7	200×1300	All floors
S10, S13	900×400	Second basement B2–first floor
	800×300	First floor–third floor
	700×300	Third floor–roof
S16, S17	550×500	Second basement B2–first floor
	500×500	First floor–second floor
	500×450	Second floor–third floor
	500×350	Third floor–fifth floor
	500×300	Fifth floor–roof
S19, S21	300×700	All floors

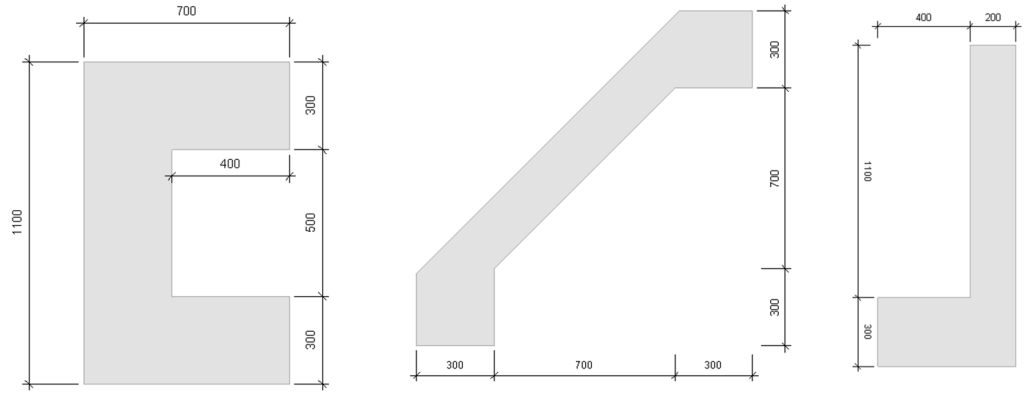

(a) (b) (c)

Figure 3.5 Section dimensions (in mm): (a) S9, S14, S20 columns, (b) P1, P3, P6, P7, P8, P9 walls and (c) P4, P5 walls.

Test for concrete strength of the building is not available. Concrete and steel grades for both the as-built and post-retrofit buildings are C25 and S420 [Turkish Standards Institute 2000], respectively [Gulkan et al. 1994]. The building has spread footings and the soil profile consists of dense sand and clay [Gulkan et al. 1994].

3.2.2 Post-retrofit properties

Top two stories of the building were removed as part of the retrofitting process. As a result, the overall height of the building was reduced to 22.4 m including the basement walls (see Figure 3.6). The structural system was strengthened by adding 0.30 m thick RC infill shear walls along both directions and 0.20 m thick shear walls around the elevator shaft (see Figure 3.7). Columns on grids D-4 and D-6 were strengthened by RC jacketing. Figure 3.8 shows the views of the structural system from the SE and NW corners. The demolished and newly added structural members are shown in Figure 3.9.

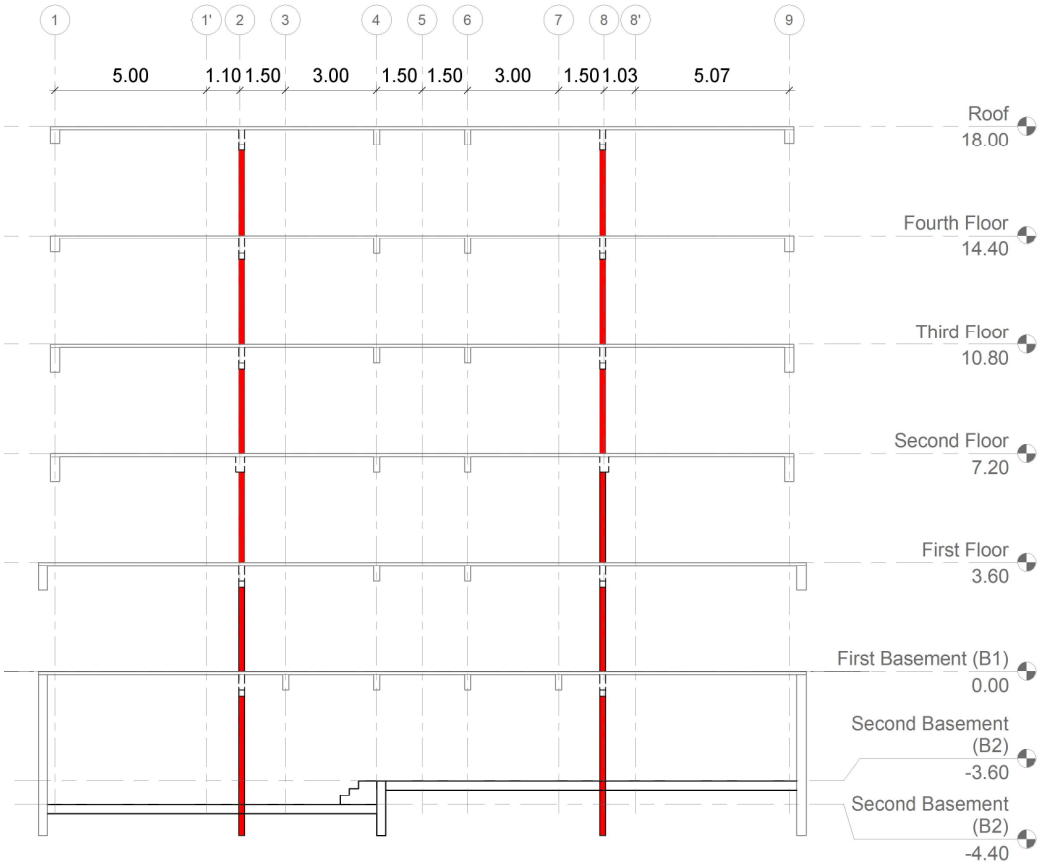

Figure 3.6 Building section A-A (see Figure 3.7; dimensions in m).

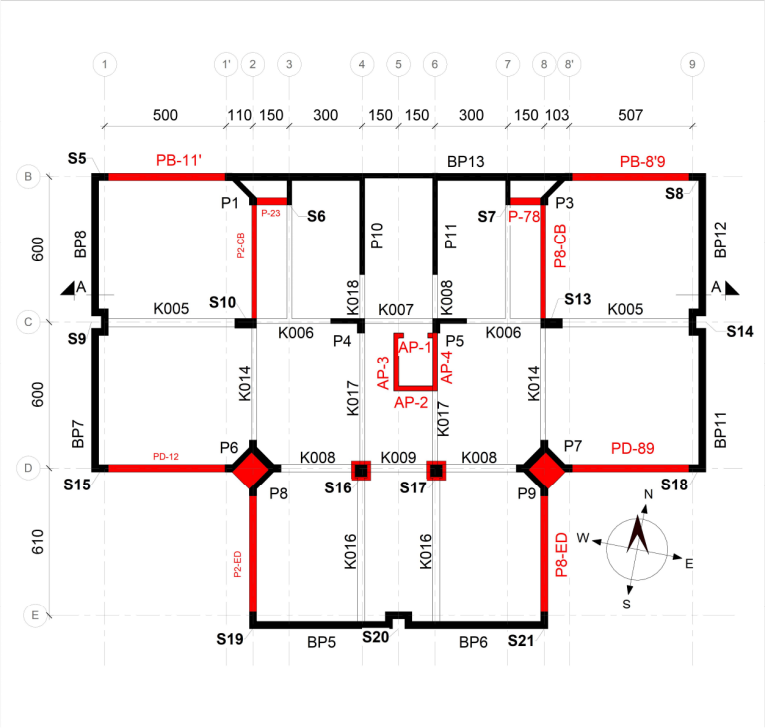

(a) First basement B1

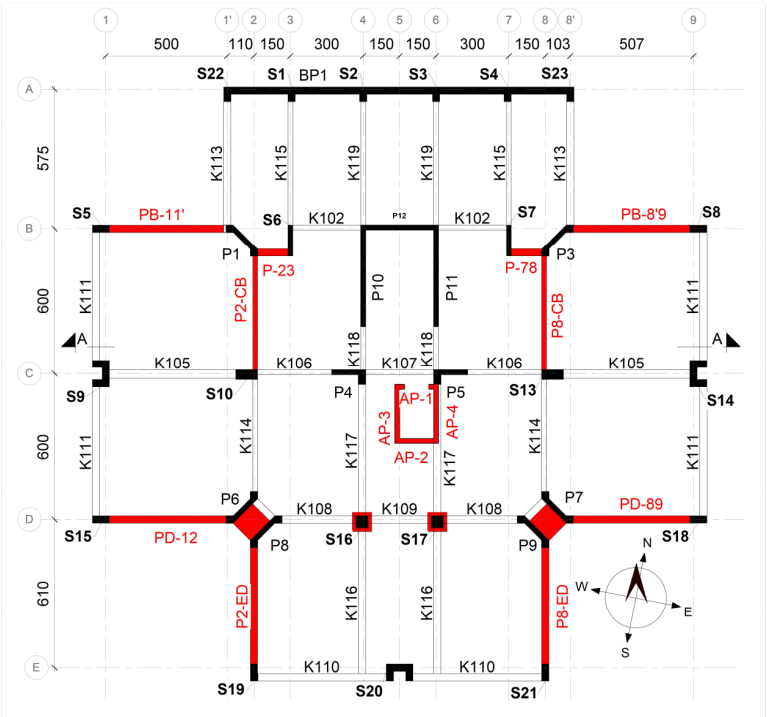

(b) First floor

Figure 3.7 Post-retrofit floor plans.

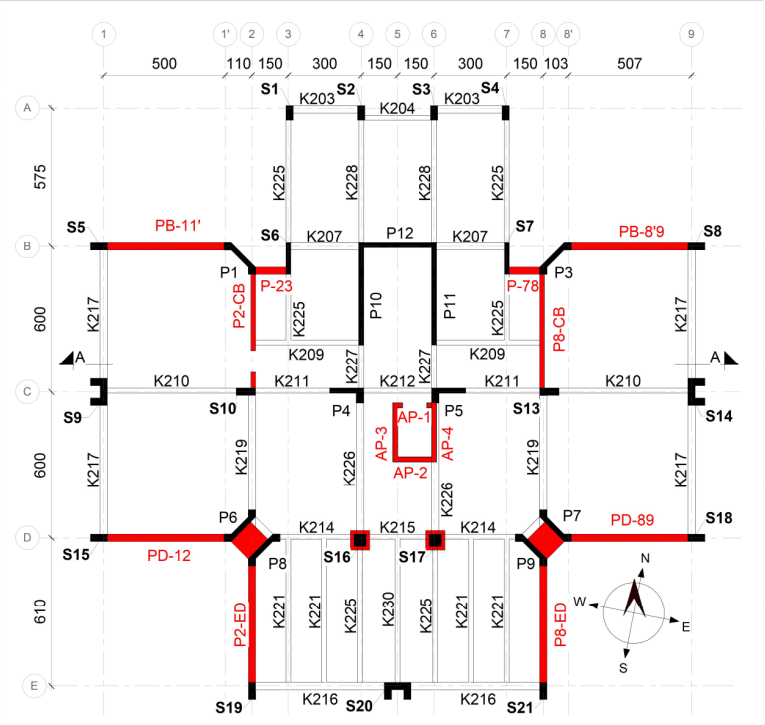

(c) Second floor

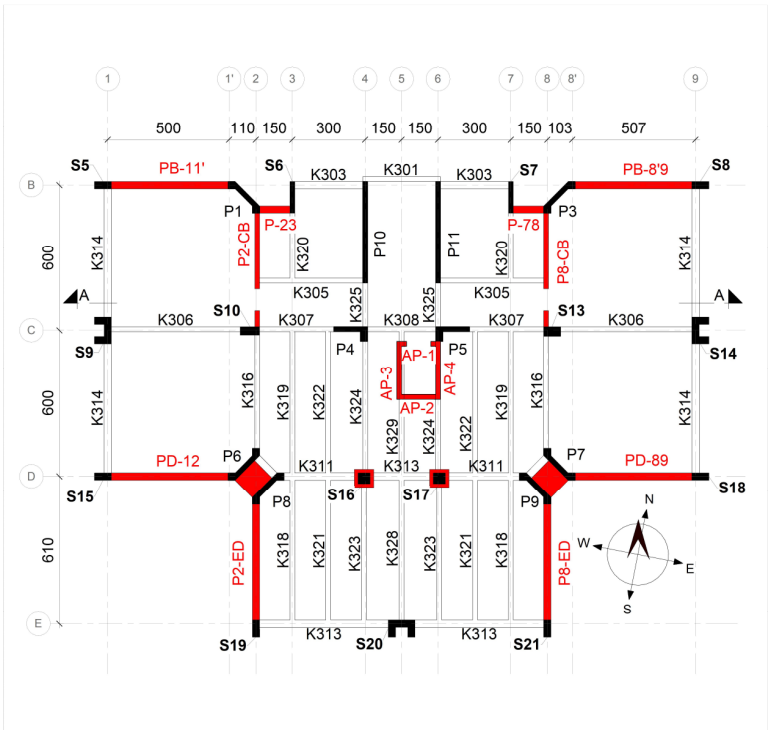

(d) Third floor

Figure 3.7 Post-retrofit floor plans (continued).

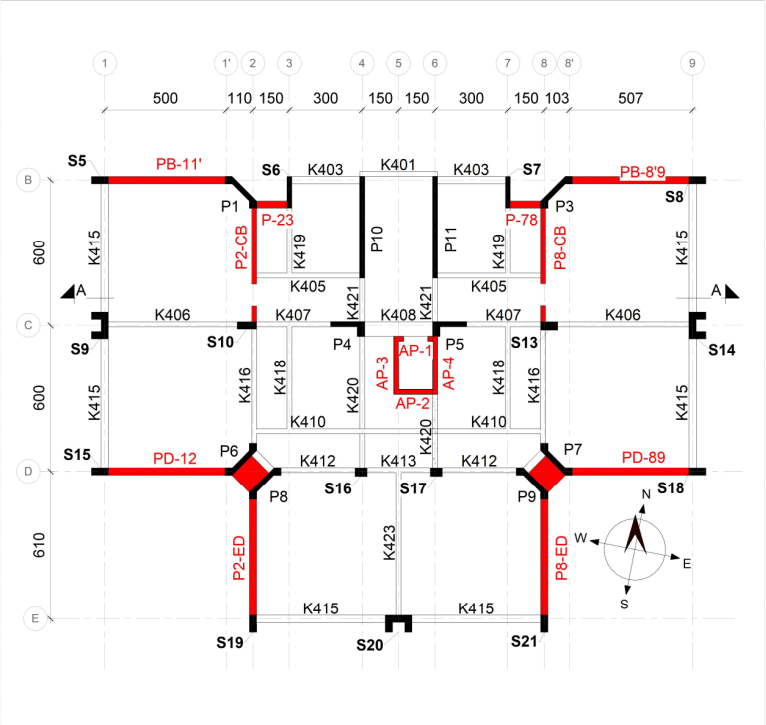

(e) Fourth floor

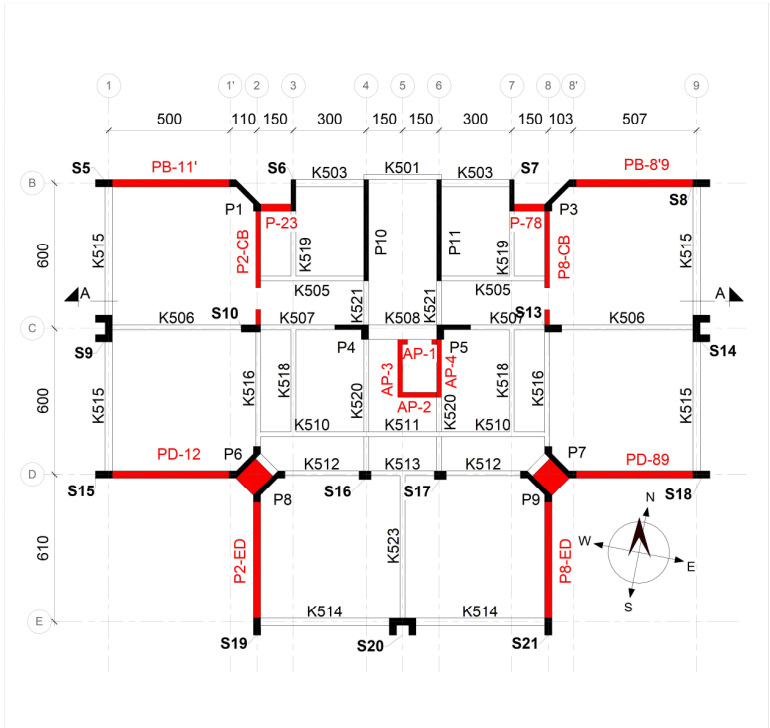

(f) Roof

Figure 3.7 Post-retrofit floor plans (continued).

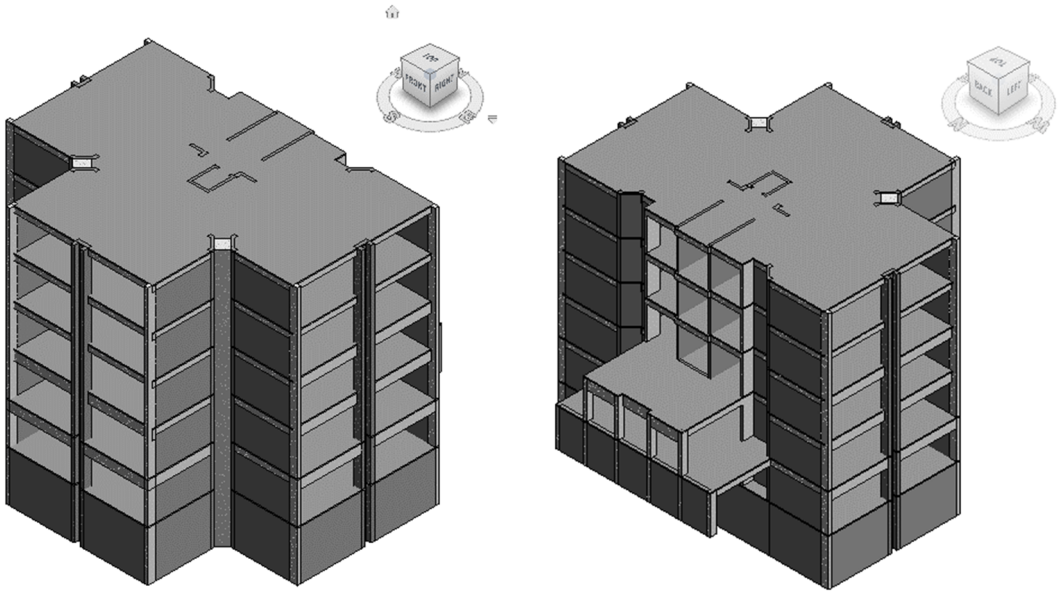

(a) (b)

Figure 3.8 Views of the structural system of the post-retrofit building from the (a) SE and (b) NW corners.

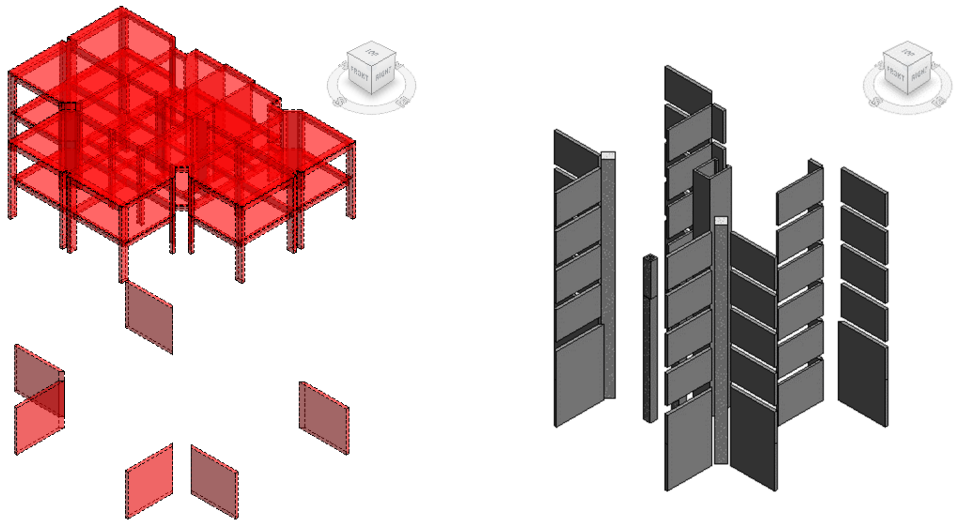

(a) (b)

Figure 3.9 Views from the SE corner of the (a) demolished and (b) newly added members.

3.3 In-Situ Structural System Dynamic Properties

3.3.1 As-built ambient vibration test data

The as-built building was instrumented as shown in Figure 3.10 [Gulkan et al. 1994]. Three uniaxial accelerometers were placed on the ceilings of the second, fourth and sixth floors. One triaxial accelerometer was placed on the floor of basement B1 and another triaxial accelerometer was placed at the free field, 25 m away from the building.

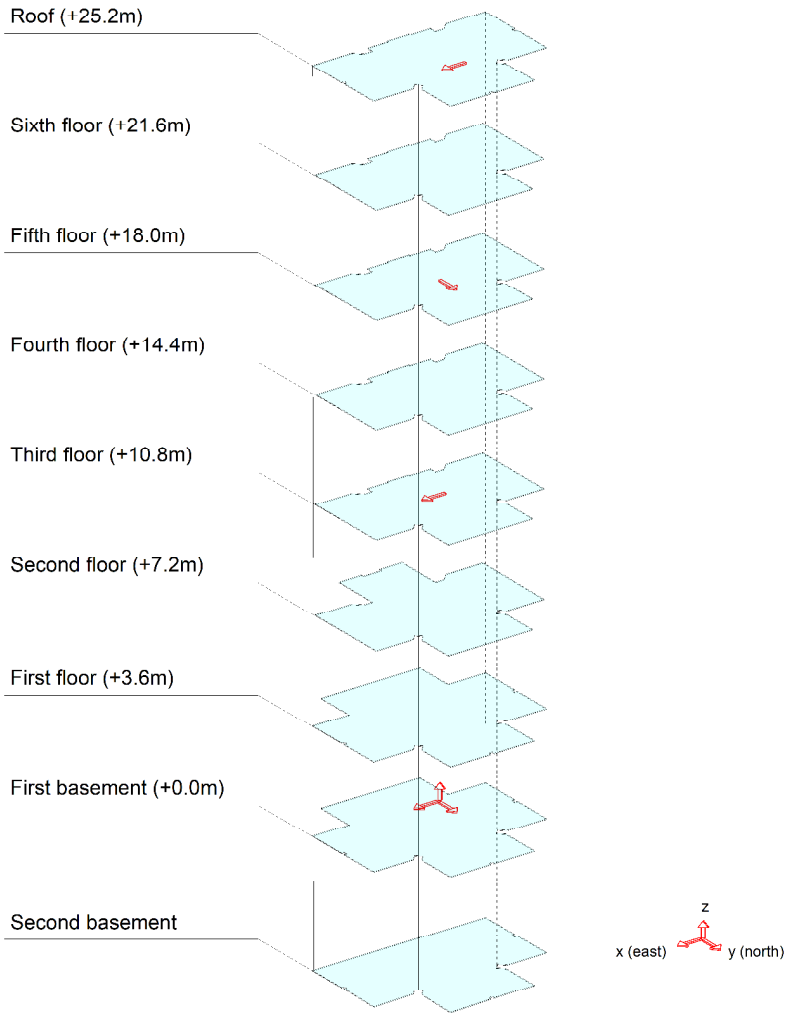

Figure 3.10 Instrumentation scheme for the as-built building.

Building responses were recorded with people moving back and forth along the building axes. Power spectra of the recorded responses are given in Figure 3.11. In the visual examination of the power spectra, it was noticed that there are two peaks at 2.5 and 3.5 Hz, roughly in the N-S direction. Other modes are unclear. On the other hand, in addition to the peak at 2.5 Hz in the E-W direction, there are peaks showing energy concentration at 4, 8 and 10 Hz. Natural vibration periods for both translational directions were identified as 0.44 s from five repeated ambient vibration tests. Associated damping ratios were reported to be 5.1% and 4.6%, respectively.

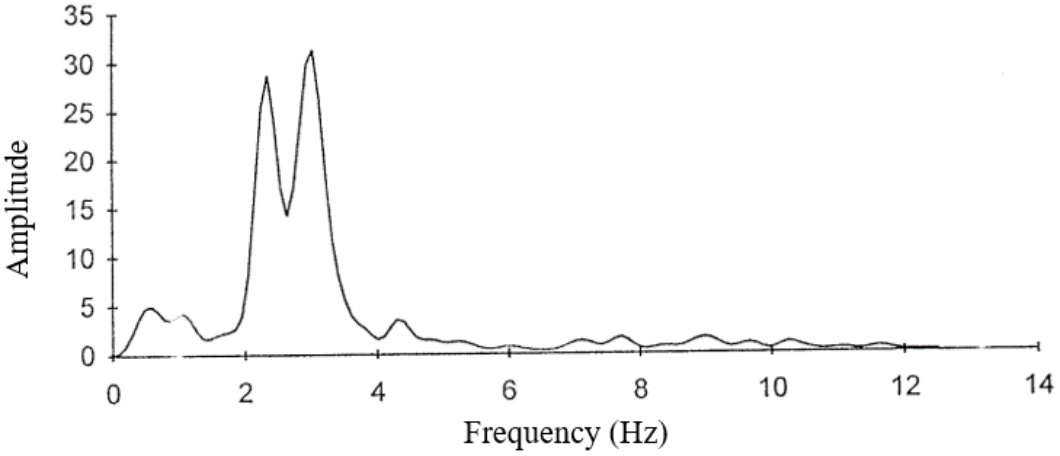

(a)

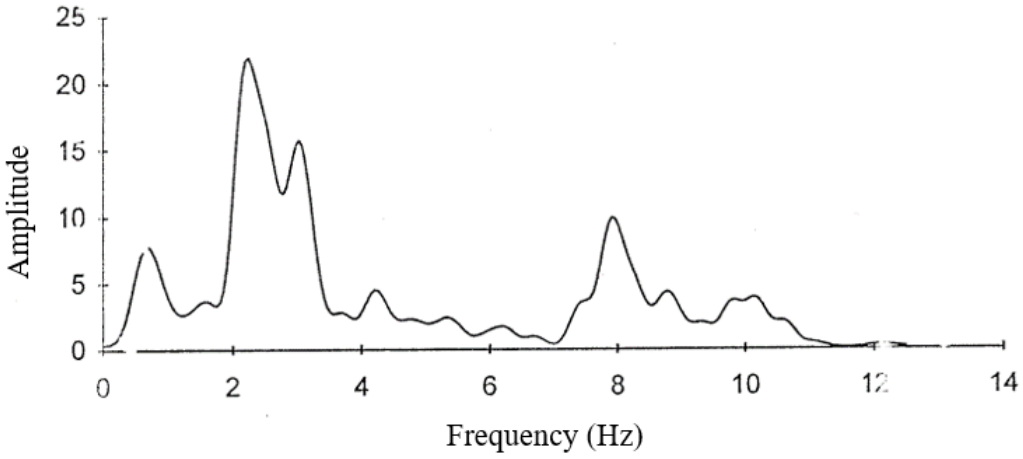

(b)

Figure 3.11 Power spectra for the (a) N-S and (b) E-W directions [Gulkan et al. 1994].

3.3.2 Post-retrofit forced vibration test data

A forced vibration test was performed on the post-retrofit building in 2013 [Celik and Gulkan 2021]. A vibration generator was anchored to the fourth-floor slab to the north of the elevator shaft. A horizontal unidirectional sinusoidal force (in kN) was applied by the vibration generator in the E-W and N-S directions, respectively:

$$p(t) = 0.24f^2 \sin(2\pi ft) \tag{3.1}$$

where f is the excitation frequency (in Hz) and t is the time (in s). 18 new uniaxial accelerometers were used to record the building response (see Figure 3.12) as those placed in 1994 were removed during the strengthening of the building. Three horizontal accelerometers were placed on the fourth and two basement floors, two parallel along the excitation direction and the third in the perpendicular direction allowing the translational and torsional responses of each of these floors to be recorded. Two horizontal accelerometers parallel to the excitation direction were placed on the first three floors. Additionally, vertical accelerometers were placed at three corners of the building on the second basement floor to monitor the rocking of the building.

A frequency sweep up to 5.0 Hz was performed in the E-W and N-S directions, with increments of usually 0.05 Hz, and frequency-response curves in the form of acceleration amplitude versus excitation frequency were obtained for the excitations in both directions (see Section 3.5). Natural vibration frequencies were determined to be 3.7 Hz for the first translational modes in both the E-W and N-S directions and 4.8 Hz for the first torsional mode. The damping ratios for the E-W, N-S and torsional directions were calculated as 6%, 9% and 6%, respectively. Dynamic properties of the building are summarized in Table 3.2.

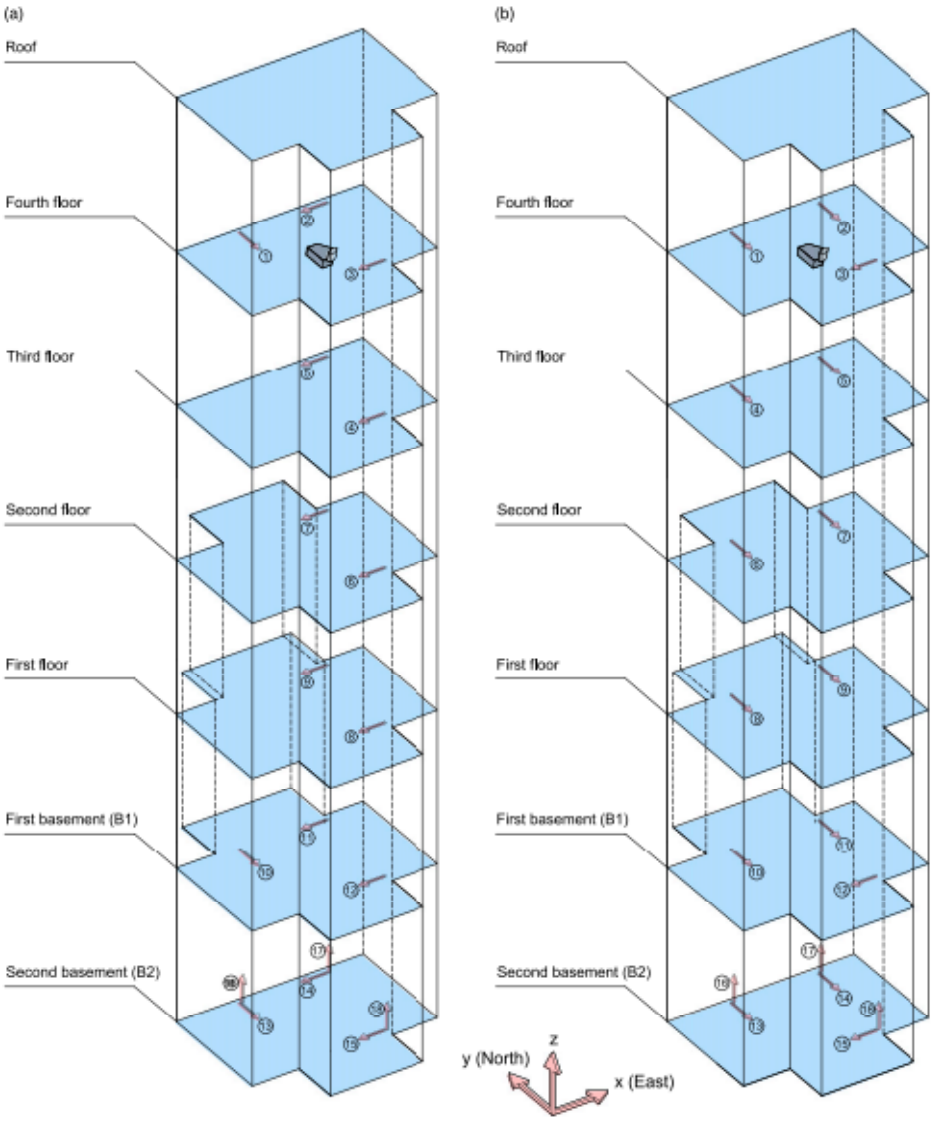

Figure 3.12 Instrumentation scheme: (a) E-W and (b) N-S excitations [Celik and Gulkan 2021].

Table 3.2 Structural system dynamic properties [Celik and Gulkan 2021].

Mode	T (s)	f (Hz)	ξ (%)	Description
1	0.27	3.7	6	E-W translation
2	0.27	3.7	9	N-S translation
3	0.21	4.8	6	Torsion

3.4 Finite Element Modeling

3-D linear elastic finite element models were developed for the as-built (see Figure 3.13) and post-retrofit (see Figure 3.14) states of the instrumented building using ETABS [Computers and Structures, Inc. 2019]. Floor plan views of the first basement and typical floors are presented in Figure 3.15 and Figure 3.16 for the as-built and post-retrofit models, respectively.

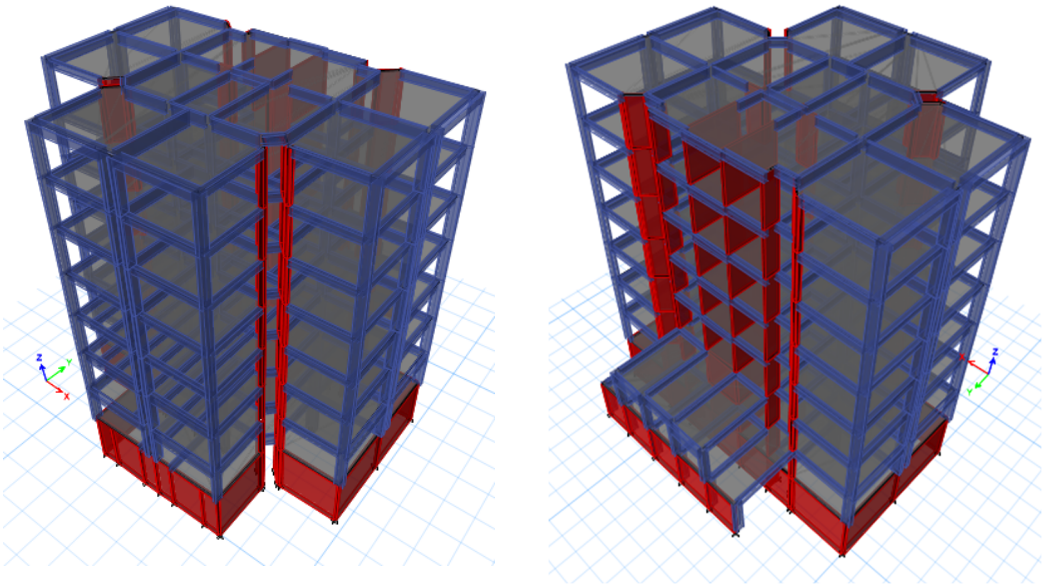

(a) (b)

Figure 3.13 3-D views of the finite element model of the as-built building from (a) SE and (b) NW corners.

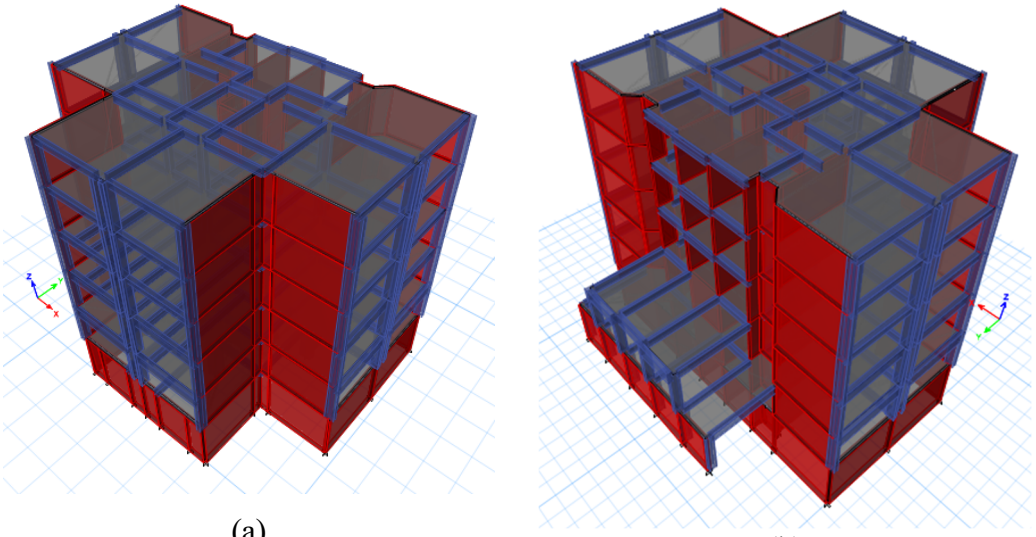

(a) (b)

Figure 3.14 3-D views of the finite element model of the post-retrofit building from (a) SE and (b) NW corners.

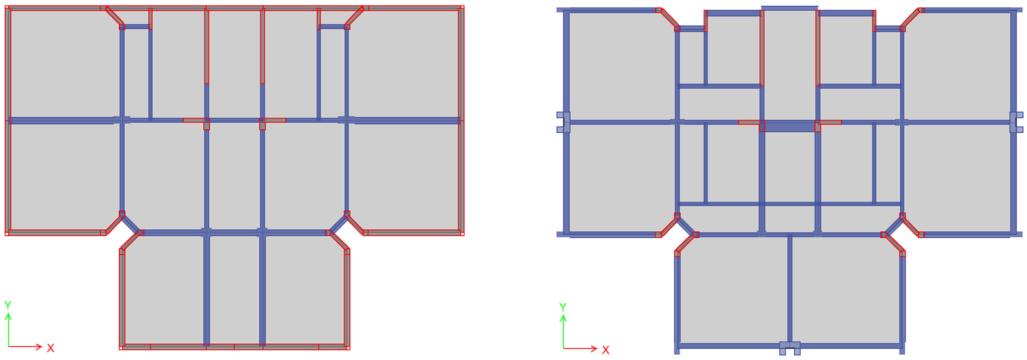

(a) (b)

Figure 3.15 Floor plan views of the (a) first basement and (b) typical (fourth floor) floors for the as-built model.

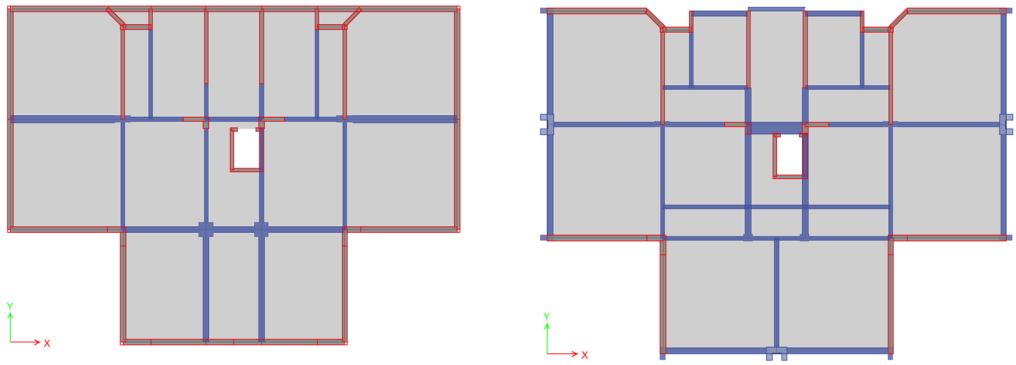

(a) (b)

Figure 3.16 Floor plan views of the (a) first basement and (b) typical (fourth floor) floors for the post-retrofit model.

Rectangular and U-shaped (S9, S14, S20) columns and beams were modeled using frame elements. Insertion points were used when there are beams that are offset from column centerlines [Computers and Structures, Inc. 2019]. Rigid end offsets were defined for beam-column connections. Rectangular, L-shaped (P4 and P5) and other (P1, P3, P6, P7, P8 and P9) shear walls and floor slabs were modeled using thin-shell elements with a maximum mesh size of 1 m × 1 m. Elevator opening in the post-retrofit building was considered. The modulus of elasticity for grade C25 concrete was taken as 30,000 MPa [Turkish Standards Institute 2000].

Mass of the building included the self-weights and superimposed dead loads but not the live loads as the dynamic tests were performed when the building was vacant. Self-weights of the structural members were calculated using the unit weight of concrete as 24 kN/m^3. Exact properties of the superimposed dead load components were not available in the structural or architectural drawings; therefore, minimum and maximum possible unit weights and thicknesses were considered in the calculations. Minimum and maximum values for the superimposed dead loads, which consisted of the weights of topping concrete, wall and floor covers, and partition walls, were calculated as 2.4 kPa and 4.2 kPa, respectively. Using these values, total dead loads for each floor of the as-built and post-retrofit buildings are as presented in Table 3.3 and Table 3.4, respectively.

Table 3.3 Dead loads for the as-built building.

Floor	Dead load (kN)	
	Minimum	Maximum
6	2900	3600
5	3200	3900
4	3200	3900
3	3200	3900
2	3400	4100
1	3900	4700
B1	4400	5200
B2	5700	6300
Total	30100	35500

Table 3.4 Dead loads for the post-retrofit building.

Floor	Dead load (kN)	
	Minimum	Maximum
4	3800	4400
3	4200	4900
2	4400	5100
1	4900	5600
B1	5300	6100
B2	6100	6800
Total	28700	32900

The interior and exterior partition walls were made of hollow factory bricks. To account for the contribution of partition walls to the lateral stiffness of the building, the equivalent diagonal strut model [Stafford Smith and Carter 1969; Mainstone 1974] adopted by AFAD [2018] was used. The width of the equivalent strut is given by

$$a_d = 0.175(\lambda_d h_k)^{-0.4} r_d \tag{3.2}$$

where λ_d is defined by

$$\lambda_d = \left[\frac{E_d t_d \sin 2\theta}{4 E_c I_k h_d}\right]^{\frac{1}{4}} \tag{3.3}$$

In Equations 3.2 and 3.3, h_k is the column length, r_d is the diagonal length of the partition wall, E_d and E_c are the moduli of elasticity of the partition wall and the frame, respectively, t_d and h_d are the thickness and height of the partition wall, respectively, θ is the slope of the diagonal and I_k is the moment of inertia of the column. The thickness and modulus of elasticity of the equivalent strut were taken as those of the partition wall. E_d is 2000 MPa for the hollow factory brick [AFAD 2018] and E_c is 30,000 MPa for grade C25 concrete [Turkish Standards Institute 2000].

The equivalent strut width for the exterior partition walls without an opening was 630 mm, which is 11% of the diagonal length of the partition wall. The equivalent strut width for the interior partition walls not surrounded by a frame was taken as 10% of the diagonal length of the partition wall [Celik 2016]. The interior and exterior partition walls have door and window openings of various sizes. Such partition walls have lower lateral stiffness compared to solid walls [Asteris 2003]. The stiffness reduction factor was used to account for the reduction in the stiffness of these partition walls. The stiffness reduction factor, α, is given by

$$\alpha = 1 - r_o \tag{3.4}$$

where r_o is the opening percentage (opening area/partition wall area) [Mosalam 1996]. Table 3.5 presents the equivalent strut model parameters for the south elevation of the building. Stiffness reduction factors are different based on the size of the openings (cf. Figure 3.17).

Table 3.5 Equivalent diagonal strut model parameters for the south elevation of the building.

Floor	a_d (mm)	α
4	627	0.64
3	627	0.64
2	627	0
1	627	0.29
B1	627	0.29
B2	NA	NA

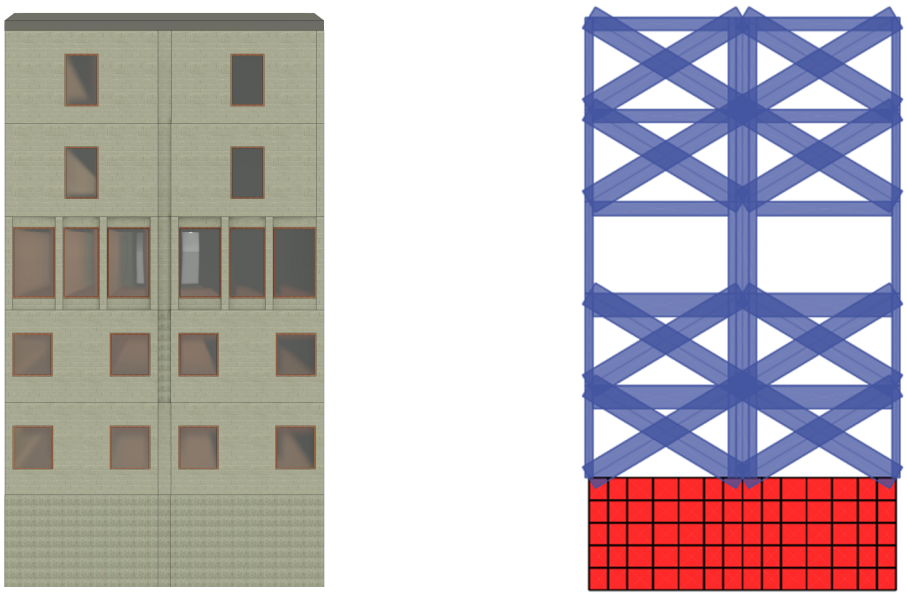

(a) (b)

Figure 3.17 (a) Architectural and (b) finite element models of the south elevation of the building.

Chrysostomou and Asteris [2012] showed that the equivalent strut width coefficient 0.175 in Equation 3.2 underestimates the stiffness of infill panels and suggested a higher coefficient of 0.27. In a recent study [Celik 2016], this coefficient was calibrated even to higher values to match the test results. In the present study, both coefficients, 0.175 and 0.27, were used.

Effective section stiffness multipliers used in modeling the structural members are also important for accurate modeling of the stiffness of the building. They are given in Table 3.6 for evaluation under service and frequent earthquakes and in Table 3.7 for earthquake load calculations [AFAD 2018].

Table 3.6 Effective section multipliers for service and frequent earthquakes [AFAD 2018].

Shear Wall - Slab (In Plane)	Axial	Shear
Shear wall	0.75	1.00
Basement shear wall	1.00	1.00
Slab	0.50	0.80
Shear Wall - Slab (Out of Plane)	Axial	Shear
Shear wall	1.00	1.00
Basement shear wall	1.00	1.00
Slab	0.50	1.00
Frame Member	Flexure	Shear
Beam	0.70	1.00
Column	0.90	1.00

Table 3.7 Effective section multipliers for earthquake load calculations [AFAD 2018].

Shear Wall - Slab (In Plane)	Axial	Shear
Shear wall	0.50	0.50
Basement shear wall	0.80	0.50
Slab	0.25	0.25
Shear Wall - Slab (Out of Plane)	Axial	Shear
Shear wall	0.25	1.00
Basement shear wall	0.50	1.00
Slab	0.25	1.00
Frame Member	Flexure	Shear
Beam	0.35	1.00
Column	0.70	1.00

3.5 Comparison of the Simulated and In-Situ Dynamic Properties

The natural vibration periods and mode shapes of the building were determined from eigenvalue analysis of the alternative structural models and compared with the in-situ dynamic properties.

3.5.1 As-built building

Dynamic properties identified from the ambient vibration test of the as-built building were compared with those determined from the finite element structural models with varying mass and stiffness properties. Table 3.8 presents the finite element model properties used in the analysis. Initially, a model was developed with no partition walls using gross section properties for the structural members. First, the effect of mass was examined. The superimposed dead loads were defined as 4.2 kPa in model #1 and 2.4 kPa in model #2. Table 3.9 compares the natural vibration periods determined with the in-situ periods. Model #1 periods were 11% longer than model #2 periods; both at least 27% longer than the in-situ periods. Hence, the contribution of partition walls to the lateral stiffness of the building is evident.

Table 3.8 Finite element model properties used for the as-built building.

	Model					
	#1	#2	#3	#4	#5	#6
Superimposed dead load (kN/m^2)	4.2	2.4	4.2	4.2	2.4	2.4
Equivalent strut width coefficient	-	-	0.175	0.27	0.175	0.27

Table 3.9 Simulated versus in-situ natural vibration periods.

		Natural vibration periods (s)		
		Ambient	Model	
Mode	Direction	Vibration	#1	#2
1	x (E-W)	0.44	0.66	0.60
2	y (N-S)	0.44	0.62	0.56
3	θ	-	0.59	0.54

Table 3.10 presents the modal mass participation ratios for the first three vibration modes for model #2. The first translational mode in the E-W direction (i.e., mode #1) and the torsional mode (i.e., mode #3) were coupled. Mode #2 was the first translational mode in the N-S direction.

Table 3.10 Modal mass participation ratios for model #2.

Mode	Modal mass participation (%)		
	x (E-W)	y (N-S)	θ
1	44	-	15
2	-	58	-
3	11	-	32

Partition walls were incorporated in models #3–6. The equivalent strut width coefficients 0.175 and 0.27 were used in models #3 and #4, respectively, where the superimposed dead loads were defined as 4.2 kPa. Models #5 and #6 were similar but the superimposed dead loads were 2.4 kPa. Table 3.11 compares the natural vibration periods determined with the in-situ periods.

Table 3.11 Simulated versus in-situ natural vibration periods.

Mode	Direction	Natural vibration periods (s)				
		Ambient Vibration	Model			
			#3	#4	#5	#6
1	y (N-S)	0.44	0.53	0.50	0.48	0.45
2	x (E-W)	0.44	0.51	0.47	0.47	0.43
3	θ	-	0.43	0.39	0.40	0.36

When the equivalent strut model was incorporated, the first mode switched from N-S to E-W direction. Using a higher strut width coefficient 0.27 resulted in 6–11% shorter natural vibration periods when compared to using the coefficient 0.175 in Equation 3.2. The natural vibration periods in the N-S and E-W directions determined from model #6 were the closest to those identified from the ambient vibration test, where the differences are about 2%. Table 3.12 presents the modal mass participation ratios for model #6. In the first three vibration modes, about 60% of the mass in translational and 50% of the mass in torsional directions were participated. Figure 3.18 presents the first three vibration mode shapes determined from model #6.

Table 3.12 Modal mass participation ratios for model #6.

Mode	Modal mass participation (%)		
	x (E-W)	y (N-S)	θ
1	-	62	-
2	48	-	15
3	10	-	37

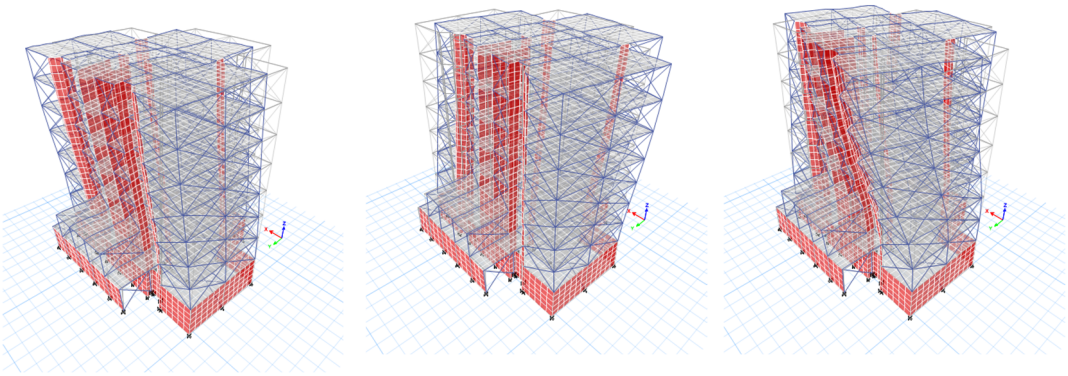

(a) (b) (c)

Figure 3.18 Vibration mode shapes from model #6: (a) mode #1, (b) mode #2, and (c) mode #3.

Models #1-6 investigated the effect of different mass and stiffness properties on the natural vibration periods of the building. Model #6 in which the superimposed dead load was 2.4 kPa and the partition walls were incorporated using an equivalent strut width coefficient of 0.27 was the closest to those identified from the ambient vibration test. Therefore, model #6 will be used as the base model in the seismic assessment of the as-built building.

3.5.2 Post-retrofit building

Dynamic properties identified from the forced vibration test of the post-retrofit building were compared with those determined from the finite element structural models with varying mass and stiffness properties. Table 3.13 presents the finite element model properties used in the analysis. Model #1 was developed using gross section properties for the structural members, with no partition walls and 2.4 kPa superimposed dead loads. Model #2 was similar with 4.2 kPa superimposed dead

loads. Table 3.14 compares the natural vibration periods determined with the in-situ periods. Model #2 periods were 5–10% longer than model #1 periods; shorter than the in-situ periods. Hence, it is evident that cracked section properties have to be incorporated in the finite element model.

Table 3.13 Finite element model properties used for the post-retrofit building.

	Model							
	#1	#2	#3	#4	#5	#6	#7	#8
Superimposed dead load (kN/m^2)	2.4	4.2	2.4	2.4	2.4	4.2	4.2	4.2
Effective section properties	-	-	Table 3.6	Table 3.7	Table 3.7	Table 3.6	Table 3.7	Table 3.7
Equivalent strut width coefficient	-	-	-	-	0.175	-	-	0.175

Table 3.14 Simulated versus in-situ natural vibration periods.

		Natural vibration periods (s)		
		Forced Vibration	Model	
Mode	Direction		#1	#2
1	y (N-S)	0.27	0.20	0.22
2	x (E-W)	0.27	0.18	0.19
3	θ	0.21	0.15	0.16

Table 3.15 presents the modal mass participation ratios for the first three vibration modes for model #2. Mode #1 was the first translational mode in the N-S direction. The first translational mode in the E-W direction (i.e., mode #2) and the torsional mode (i.e., mode #3) were coupled.

Table 3.15 Modal mass participation ratios for model #2.

	Modal mass participation (%)		
Mode	x (E-W)	y (N-S)	θ
1	-	65	-
2	38	-	28
3	25	-	26

Cracked section properties were incorporated in models #3 and #4, where the superimposed dead loads were defined as 2.4 kPa. Models #3 and #4 used the effective section stiffness multipliers for service and frequent earthquakes (see Table 3.6) and design earthquake (see Table 3.7), respectively. Partition walls were then incorporated in model #5 with an equivalent strut width coefficient of 0.175. Table 3.16 compares the natural vibration periods determined with the in-situ periods.

Table 3.16 Simulated versus in-situ natural vibration periods.

		Natural vibration periods (s)			
		Forced Vibration	Model		
Mode	Direction		#3	#4	#5
1	y (N-S)	0.27	0.21	0.26	0.25
2	x (E-W)	0.27	0.19	0.24	0.22
3	θ	0.21	0.16	0.20	0.18

Model #3 periods were 5% longer than those determined from model #1, in which the gross section properties were used (cf. Table 3.16). Model #4 periods, on the other hand, were 33% longer. The periods determined from model #5, in which the partition walls were modeled, were only shorter 0.01–0.02 s than model #4 periods. Hence, the contribution of partition walls to the lateral stiffness of a shear-wall building is not as noteworthy as a moment-resisting frame building.

Table 3.17 presents the modal mass participation ratios for models #3–5. In models #3 and #4, where partition walls were not modeled, the first E-W translational and torsional modes (i.e., modes #2 and #3) were coupled. Modal mass participations for these modes are quite close to each other. In model #5, where partition walls were modeled, the coupling between the first E-W translational and torsional modes was reduced. Figure 3.19 presents the first three vibration mode shapes determined from model #4.

Table 3.17 Modal mass participation ratios for models #3, #4 and #5.

Mode	Modal mass participation (%)								
	Model #3			Model #4			Model #5		
	x (E-W)	y (N-S)	θ	x (E-W)	y (N-S)	θ	x (E-W)	y (N-S)	θ
1	-	64	-	-	0.65	-	-	0.66	-
2	32	-	31	32	-	33	39	-	28
3	29	-	21	31	-	21	25	-	27

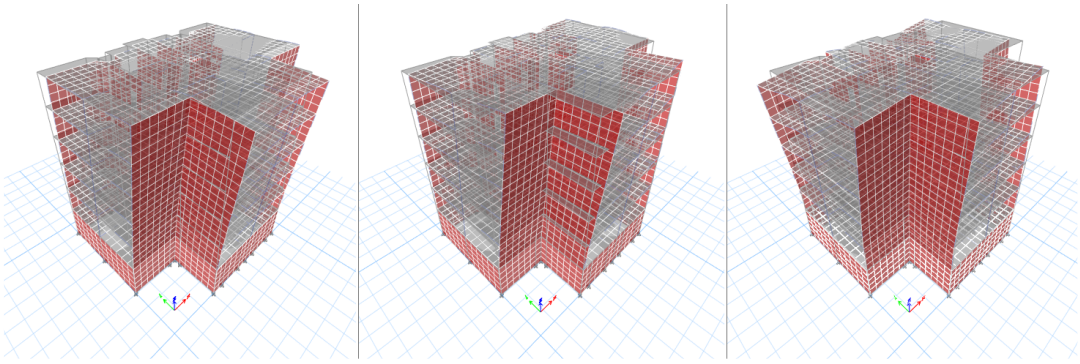

(a) (b) (c)

Figure 3.19 Vibration mode shapes from model #4: (a) mode #1, (b) mode #2 and (c) mode #3.

The above comparisons were respectively repeated by defining the superimposed dead loads as 4.2 kPa in models #6–8. Table 3.18 compares the natural vibration periods determined with the in-situ periods. Table 3.19 presents the modal mass participation ratios for models #6–8. Figure 3.20 presents the first three vibration mode shapes determined from model #8.

Table 3.18 Simulated versus in-situ natural vibration periods.

Mode	Direction	Natural vibration periods (s)			
		Forced Vibration	Model		
			#6	#7	#8
1	y (N-S)	0.27	0.23	0.28	0.27
2	x (E-W)	0.27	0.20	0.25	0.24
3	θ	0.21	0.17	0.22	0.20

Table 3.19 Modal mass participation ratios for model #6, #7 and #8.

Mode	Modal mass participation (%)								
	Model #6			Model #7			Model #8		
	x (E-W)	y (N-S)	θ	x (E-W)	y (N-S)	θ	x (E-W)	y (N-S)	θ
1	-	64	-	-	65	-	-	66	-
2	35	-	29	35	-	31	44	-	26
3	27	-	23	29	-	23	23	-	29

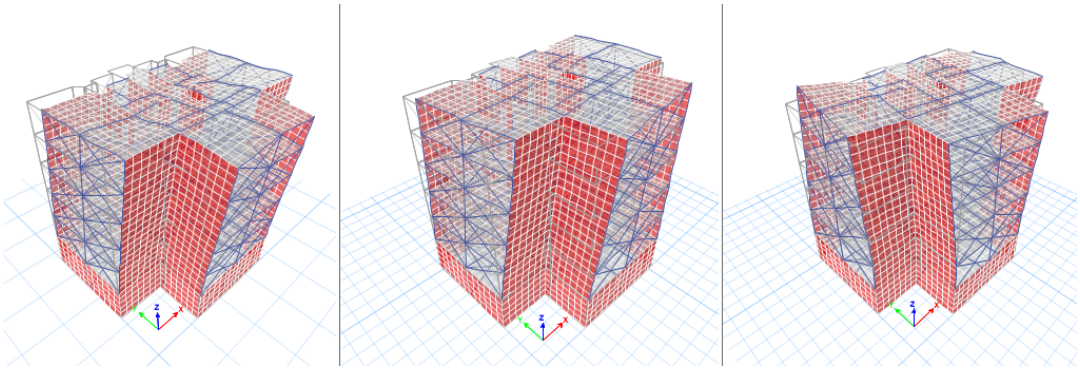

(a) (b) (c)

Figure 3.20 Vibration mode shapes from model #8: (a) mode #1, (b) mode #2 and (c) mode #3.

Model #4 and #8 periods were the closest to those identified from forced vibration tests. These two models had different stiffness and mass properties. When the natural vibration mode shapes identified from the forced vibration test were compared with those determined from models #4 and #8, shown in Figure 3.21 and Figure 3.22, respectively, model #8 mode shapes showed a closer match with those from the forced vibration test. Note that, these mode shapes values were taken at grid C-5 (see Figure 3.7 for gridlines).

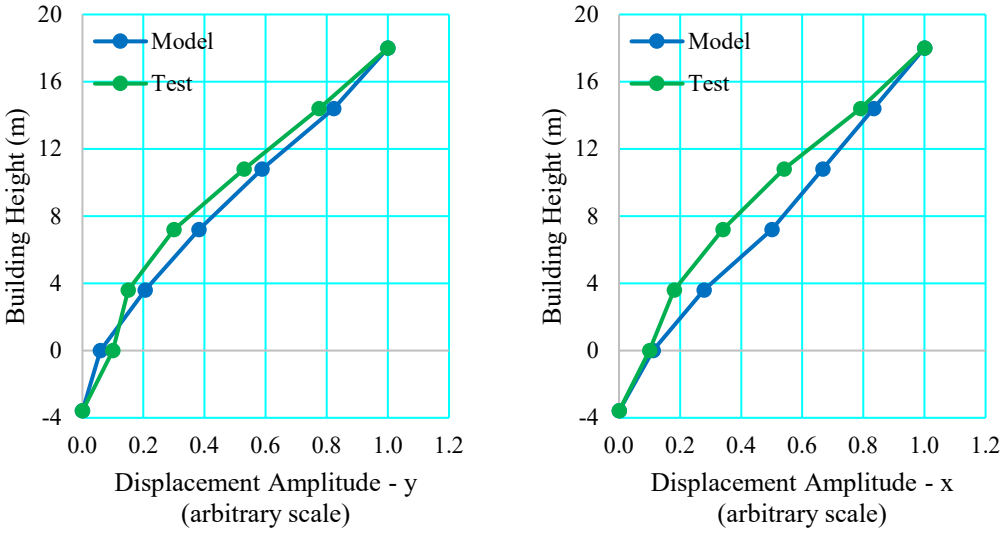

(a) (b)

Figure 3.21 Model #4 mode shapes (a) mode #1 and (b) mode #2.

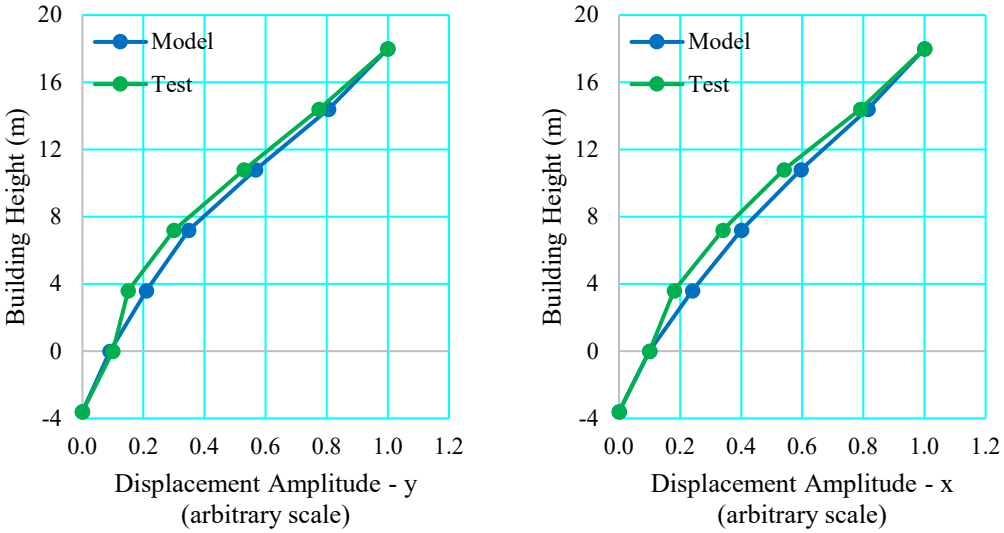

(a) (b)

Figure 3.22 Model #8 mode shapes (a) mode #1 and (b) mode #2.

In any case, merely comparing the dynamic properties can be misleading as different combinations of the modeling parameters may produce similar dynamic properties. Therefore, steady-state analyses [Celik 2016] in the N-S and E-W directions were carried out using models #4 and #8 to simulate the acceleration-frequency response curves for comparison with those from the forced vibration test. Steady state analysis

is the simulation of forced vibration test on a finite element model. It was performed on SAP2000 software [Computers and Structures, Inc. 2020]. Models #4 and #8 were selected since they had the closest natural vibration periods to those from the forced vibration test. The sinusoidal force given in Equation 3.1, by which the building was excited in the E-W and N-S directions during the forced vibration test, was applied in the finite element models. Modal damping was approximated by using stiffness proportional hysteretic damping with coefficient twice the modal damping ratio in frequency-domain analysis [Computers and Structures, Inc. 2020]. Note that modal damping ratios identified from the forced vibration test were presented in Table 3.2.

Figure 3.23 shows the experimental acceleration–frequency response curves for the N-S excitation (see Figure 3.12 for the accelerometer numbers) [Celik and Gulkan 2021]. Those determined from models #4 and #8 are plotted in Figure 3.24 and Figure 3.25, respectively. Table 3.20 compares the maximum acceleration values from models #4 and #8 and the forced vibration test. Model #8 accelerations matched the experimental amplitudes better.

Figure 3.26 shows the experimental acceleration–frequency response curves for the E-W excitation [Celik and Gulkan 2021]. Those determined from models #4 and #8 are plotted in Figure 3.27 and Figure 3.28, respectively. Table 3.21 compares the maximum acceleration values from models #4 and #8 and the forced vibration test. Model #8 accelerations also matched the experimental amplitudes better.

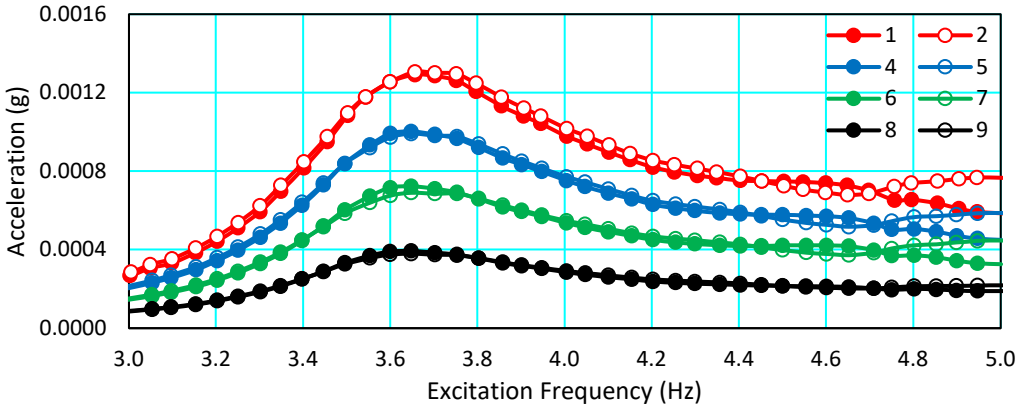

Figure 3.23 Experimental acceleration-frequency response curves for the N-S excitation [Celik and Gulkan 2021].

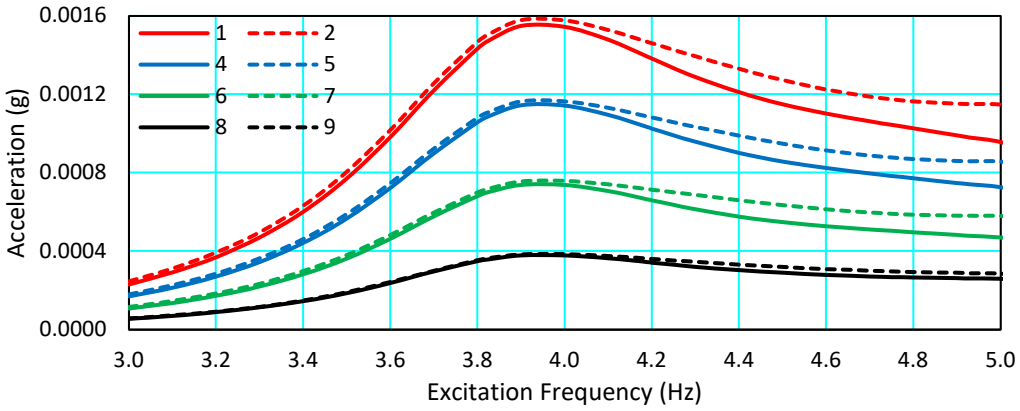

Figure 3.24 Simulated acceleration-frequency response curves for the N-S excitation from model #4.

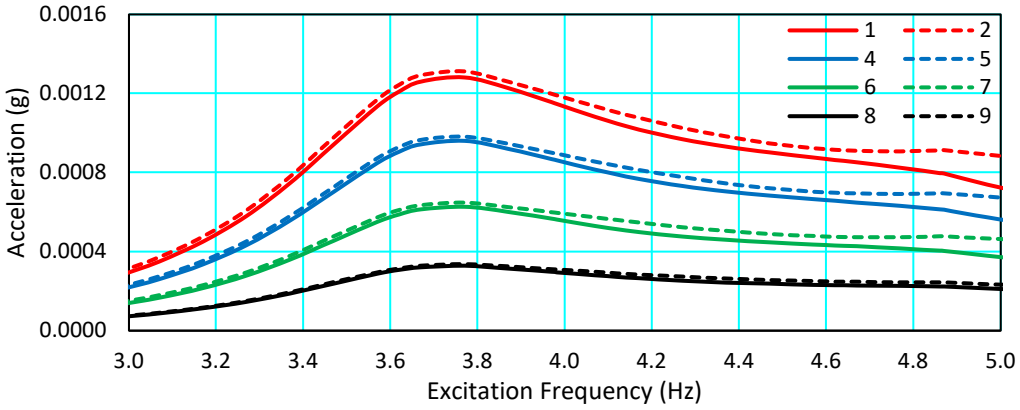

Figure 3.25 Simulated acceleration-frequency response curves for the N-S excitation from model #8.

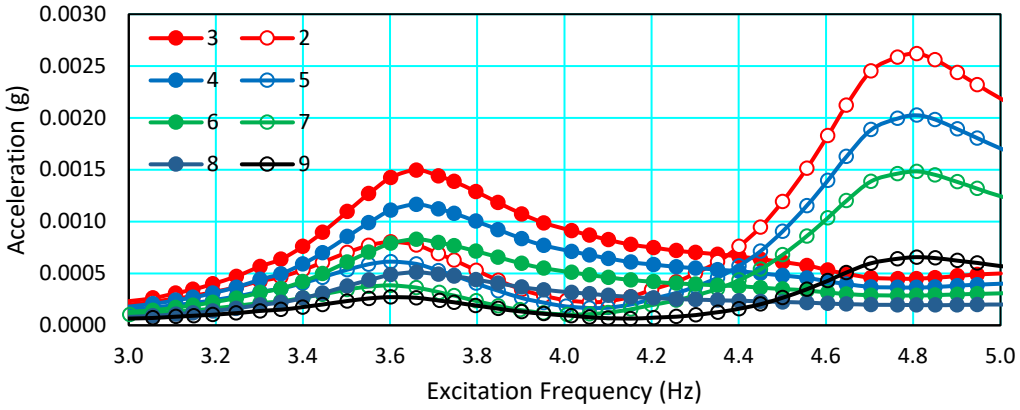

Figure 3.26 Experimental acceleration-frequency response curves for the E-W excitation [Celik and Gulkan 2021].

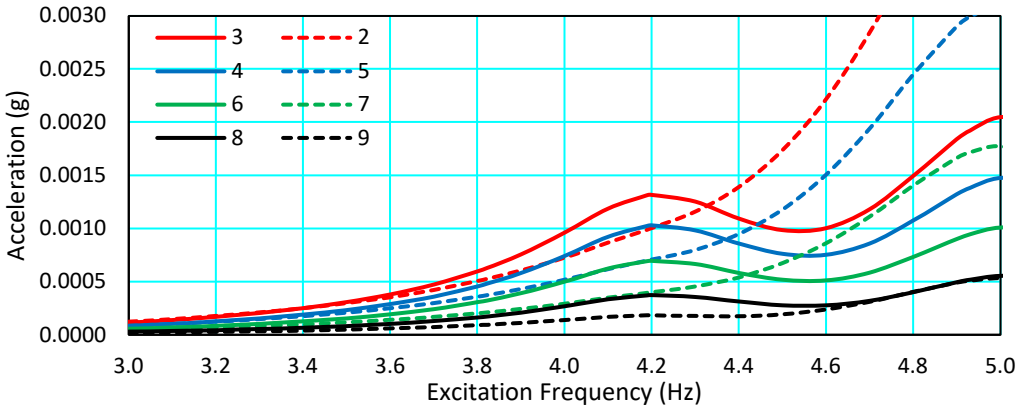

Figure 3.27 Simulated acceleration-frequency response curves for the E-W excitation from model #4.

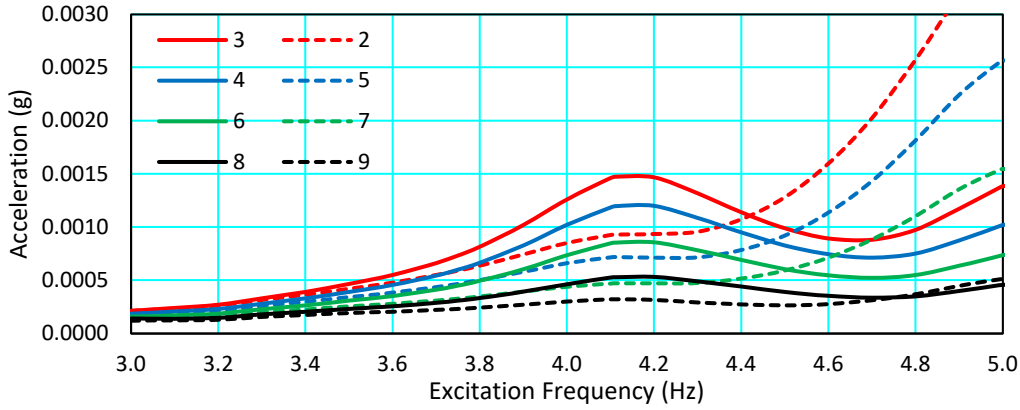

Figure 3.28 Simulated acceleration-frequency response curves for the E-W excitation from model #8.

Table 3.20 Maximum acceleration value comparison for N-S direction.

Accelerometer	Acceleration (g)			Error (%)	
	Test	Model #4	Model #8	Model #4	Model #8
1	0.0013	0.0016	0.0013	20	0
2	0.0013	0.0016	0.0013	22	2
4	0.0010	0.0012	0.0010	17	1
5	0.0010	0.0012	0.0010	18	0
6	0.0007	0.0008	0.0007	7	7
7	0.0007	0.0008	0.0007	10	4
8	0.0004	0.0004	0.0003	5	8
9	0.0004	0.0004	0.0003	8	6

Table 3.21 Maximum acceleration value comparison for E-W direction.

Accelerometer	Acceleration (g)			Error (%)	
	Test	Model #4	Model #8	Model #4	Model #8
2	0.0013	-	0.0009	-	6
3	0.0013	0.0013	0.0015	12	2
4	0.0010	0.0010	0.0012	14	0
5	0.0010	-	0.0008	-	24
6	0.0007	0.0007	0.0009	13	7
7	0.0007	-	0.0005	-	14
8	0.0004	0.0004	0.0005	26	4
9	0.0004	-	0.0003	-	7

3.6 Summary

3-D finite element structural models for the as-built and post-retrofit states of the instrumented building were developed. Mass and stiffness parameters that were used in the finite element models were presented. For the as-built building, natural vibration periods identified from the ambient vibration test and those determined from the finite element models were compared. Model #6 which uses gross section properties, an equivalent strut width coefficient of 0.27 and a superimposed dead

load of 2.4 kPa has the closest natural vibration periods. For the post-retrofit building, natural vibration periods, mode shapes and acceleration-frequency response curves determined from the forced vibration test and the finite element models were compared. Model #8 which uses the effective section stiffness multipliers for the design earthquake, an equivalent strut width coefficient of 0.175 and a superimposed dead load of 4.2 kPa has the closest match. Models #6 and #8 will be used as the base models for the seismic risk assessment of the as-built and post-retrofit buildings, respectively.

CHAPTER 4

SEISMIC RISK ASSESSMENT PER BUILDING CODES

4.1 Introduction

Seismic risk assessment of the Belkis Sabanci Dormitory was performed for the as-built and post-retrofit states of the building using past and current building codes. For the as-built building, the goal is to evaluate the retrofit decision. For post-retrofit building, the goal is to evaluate the effectiveness of the retrofit and to compare the seismic risk assessment procedures in MPWS [2007] and AFAD [2018]. Finite element models that were developed and updated to match the dynamic properties identified from the previous ambient and forced vibration tests of the building were used with some modifications as required per the building codes.

For the as-built building, a rapid assessment per MEUCC [2021] was initially performed followed by a more detailed linear elastic assessment per MPWS [2007]. Eventually, the retrofit decision was evaluated for the as-built building. For the post-retrofit building, similar steps were followed skipping the rapid assessment as it is not applicable to retrofitted buildings. Finally, a nonlinear assessment of the post-retrofit building was performed per AFAD [2018] using the selected 11 ground motion pairs. Eventually, the post-retrofit state of the building was evaluated.

The elastic design response spectrum per MPWS [2007] for local site class Z2 and seismic zone 1, which is associated with a 10% probability of exceedance (PE) in 50 years, is plotted in Figure 4.1. This earthquake is defined as the design-basis earthquake (DBE). The maximum considered earthquake (MCE) is defined as 1.5 times the DBE earthquake and is also plotted in Figure 4.1.

There are four earthquake ground motion levels defined in AFAD [2018]:

- DD-1 is a very rare earthquake hazard, also known as the MCE, associated with a 2% PE in 50 years, i.e., 2475-year return period.
- DD-2 is a rare earthquake hazard, also known as the DBE, associated with a 10% PE in 50 years, i.e., 475-year return period.
- DD-3 is a frequent earthquake hazard, associated with a 50% PE in 50 years, i.e., 72-year return period.
- DD-4 is a very frequent earthquake hazard, also known as the service earthquake, associated with a 68% PE in 50 years or a 50% PE in 30 years, i.e., 43-year return period.

The elastic response spectra for these hazard levels per AFAD [2018] for local site class ZD are plotted in Figure 4.1. Response reduction factor, R, was used as 1 in all seismic assessment methods.

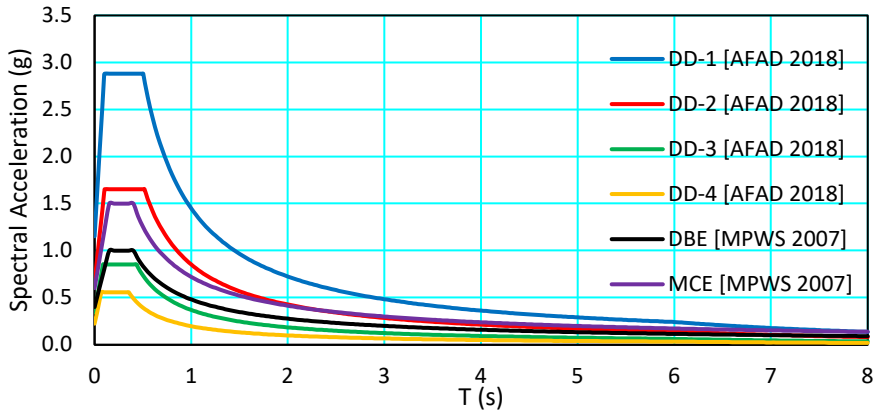

Figure 4.1 Elastic response spectra per MPWS [2007] and AFAD [2018].

4.2 As-Built Building

The superimposed dead load is calculated as 2.4 kPa for the as-built building and 4.2 kPa for the post-retrofit building (see Chapter 3). The live load is defined as 3.5 kPa and 1.5 kPa for typical floors and roofs, respectively [Turkish Standards Institute

1997], with a participation coefficient, n, of 0.6 for this dormitory building [AFAD 2018; MPWS 2007].

4.2.1 Rapid assessment per MEUCC [2021]

The rapid seismic risk assessment method by MEUCC [2021] applies to low-rise intact (undamaged, not strengthened) buildings that are shorter than 30 m and have less than 10 stories. This method is not applicable for school or dormitory buildings; however, the as-built building, with its overall height of 25.2 m over the first basement level and 8 floors in total, satisfies these size requirements. Linear elastic response spectrum analysis was performed under the DD-3 earthquake hazard level, with short-period (F_s) and 1.0 s-period site coefficients (F_1) of 1.0 (see Figure 4.2).

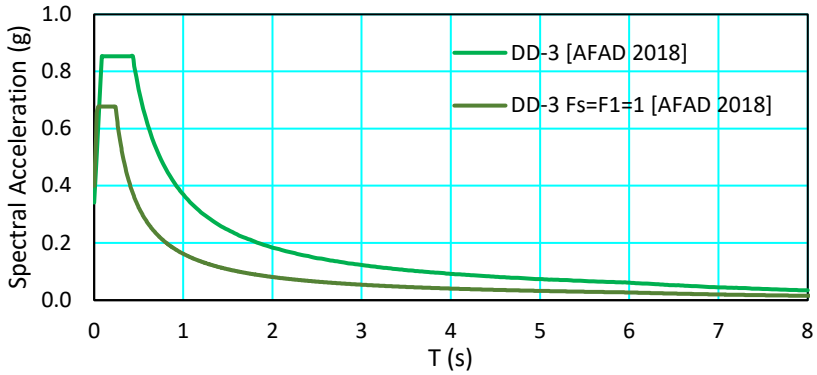

Figure 4.2 Elastic response spectra per MEUCC [2021] and AFAD [2018].

Existing concrete compressive strength, f_{cm}, was defined as 25 MPa [Gulkan et al. 1994]. The modulus of elasticity for concrete was calculated as 25000 MPa using

$$E = 5000\sqrt{f_{cm}} \tag{4.1}$$

Equations 4.2 and 4.3 provide the effective bending rigidities for beams, shear walls, slabs and for columns, respectively:

$$(EI)_e = 0.3(EI)_o \tag{4.2}$$

$$(EI)_e = 0.5(EI)_o \tag{4.3}$$

where $(EI)_o$ is the bending rigidity for the gross section.

Interstory drift ratios throughout the building height under the $G + nQ \mp E$ load combination (G is the dead load, Q is the live load and E is the earthquake load) are shown in Figure 4.3.

Seismic assessment was performed by comparing the axial load ratios on the columns and shear walls, N_d/N_0, with the axial load ratio limits:

$$(N_d/N_0)_{limit} = \begin{cases} 0.7 & (\delta/h)_{cr} < 0.25 \\ 0.7 \cdot \dfrac{0.25}{(\delta/h)_{cr}} & 0.25 \leq (\delta/h)_{cr} \leq 1.75 \\ 0.1 & (\delta/h)_{cr} > 1.75 \end{cases} \tag{4.4}$$

where N_d is the axial load under the gravity loads ($G + nQ$), N_0 is the axial load capacity, δ is the floor displacement, h is the floor height and $(\delta/h)_{cr}$ is the critical interstory drift ratio in %.

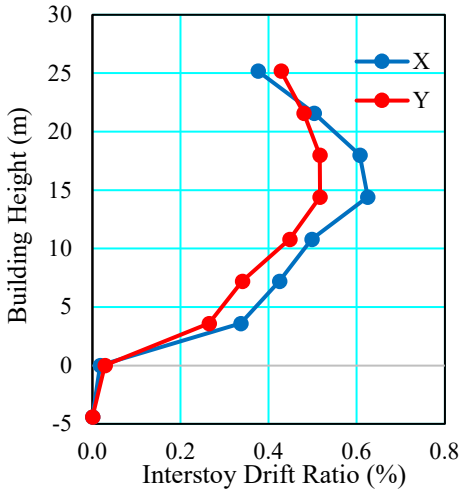

Figure 4.3 Interstory drift ratios in X and Y directions under the $G + nQ \mp E$ combination.

Table 4.1 shows the critical interstory drift ratios, the axial load ratio limits and the critical axial load ratios, $(N_d/N_0)_{cr}$, defined as the average of the largest 30% of the axial load ratio values. Figure 4.4 compares the critical axial load ratios with the limits as a function of the critical interstory drift ratios. All critical axial load ratios

are smaller than the limiting values, which calls for an elaborate seismic risk assessment [MEUCC 2021].

Table 4.1 Building critical axial load ratio, drift ratio and axial load limit.

Floor	$(N_d/N_0)_{cr}$	$G + nQ \mp E_x$		$G + nQ \mp E_y$	
		$(\delta/h)_{cr}$	$(N_d/N_0)_{limit}$	$(\delta/h)_{cr}$	$(N_d/N_0)_{limit}$
6	0.03	0.38	0.47	0.43	0.41
5	0.07	0.50	0.35	0.48	0.36
4	0.10	0.61	0.29	0.52	0.34
3	0.14	0.62	0.28	0.52	0.34
2	0.18	0.50	0.35	0.45	0.39
1	0.20	0.42	0.41	0.34	0.51
B1	0.23	0.34	0.52	0.26	0.66
B2	0.40	0.02	0.70	0.03	0.70

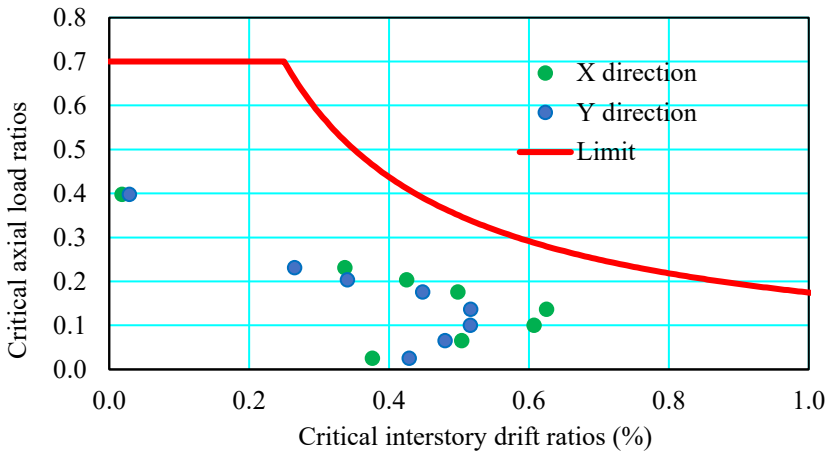

Figure 4.4 Comparison of the critical axial load ratios with the limits.

4.2.2 Linear assessment per MPWS [2007]

Linear elastic seismic risk assessment of the as-built building was performed per Chapter 7 of the 2007 Turkish Earthquake Code [MPWS 2007]. Structural drawings of the as-built building as well as its dynamic properties from an ambient vibration test were available, thus the level of information about the building was assumed as comprehensive.

There are three damage limits (performance levels): immediate occupancy (IO), life safety (LS) and collapse prevention (CP), and four damage states: minimum, significant, advanced and collapse, defined for ductile members (see Figure 4.5).

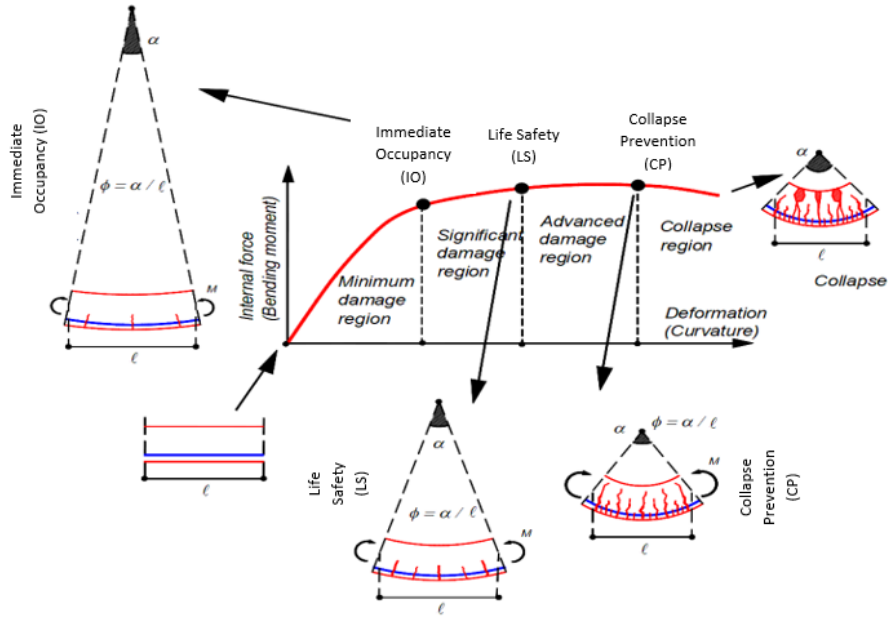

Figure 4.5 Damage states for ductile members [Celep 2014].

Performance objectives for buildings are set based on their occupancy. Dormitory buildings are expected to meet the IO performance level, i.e., remain safe to occupy with only slight structural damage, when subjected to a DBE ground motion, associated with a 10% PE in 50 years, and they are expected to meet the LS performance level, i.e., sustain significant structural damage with a substantial reduction in their stiffness and strength but retain a significant margin against collapse, when subjected to an MCE, associated with a 2% PE in 50 years.

Seismic assessment was performed for examining the IO performance objective. To satisfy this objective, a maximum of 10% of the beams on a single floor can sustain significant damage while all other structural members can only suffer minimum damage.

Cracked section effective bending rigidities were used for beams:

$$(EI)_e = 0.4\,(EI)_o \tag{4.5}$$

and for shear walls and columns:

$$\begin{aligned} (EI)_e &= 0.4\,(EI)_o \;\; if \;\; \frac{N_d}{A_c f_{cm}} \leq 0.1 \\ (EI)_e &= 0.8\,(EI)_o \;\; if \;\; \frac{N_d}{A_c f_{cm}} \geq 0.4 \end{aligned} \tag{4.6}$$

where A_c is the cross-sectional area of the member.

In the finite element analysis, model #6 (see Chapter 3) was used as the base model. The contribution of partition walls was not considered since there is no procedure defined in seismic assessment section of MPWS [2007]. Effective section stiffness multipliers were incorporated per Equations 4.5 and 4.6. Table 4.2 presents the natural vibration periods and modal mass participation ratios.

Table 4.2 Natural vibration periods and modal mass participation ratios of the as-built building for the seismic assessment per MPWS [2007].

Mode	Natural vibration periods (s)	Modal mass participation ratios (%)		
		x (E-W)	y (N-S)	θ
1	1.02	46	-	14
2	0.97	-	59	-
3	0.89	9	-	34

Gravity load analysis was performed under the $G + nQ$ load case. For earthquake load analysis, there are two linear elastic analysis procedures permitted: the equivalent lateral force procedure and the response spectrum analysis. To use the equivalent lateral force procedure, the torsional irregularity coefficient, η_{bi} should be less than 1.4. However, this coefficient was calculated as 1.92 in the X direction (see Table 4.3). Hence, linear elastic response spectrum analysis was performed for earthquake load analysis.

Table 4.3 Torsional irregularity coefficient in the X and Y directions for the as-built building.

	X direction		Y direction	
Floor	η_{bi}	Check	η_{bi}	Check
Roof	1.11	OK	1.00	OK
6	1.06	OK	1.00	OK
5	1.05	OK	1.00	OK
4	1.1	OK	1.00	OK
3	1.07	OK	1.00	OK
2	1.51	NO GOOD	1.00	OK
1	1.92	NO GOOD	1.00	OK
B1	1.31	OK	1.00	OK

The internal forces and deflections, B_B, were amplified using

$$B_D = \frac{\beta V_t}{V_{tB}} B_B \tag{4.7}$$

where B_D is the amplified internal force or deflection, β is the coefficient used for the lower bound value of the mode combination method. V_t is the base shear calculated per the equivalent lateral force procedure: 17000 kN and 22000 kN in the X and Y directions, respectively. V_{tB} is the base shear calculated per the response spectrum analysis: 10000 kN and 15000 kN in the X and Y directions, respectively. In the response spectrum analysis, 24 modes were used to achieve 90% mass participation in both directions.

β is dependent on the A1, B2 and B3 type irregularities. A1 is the torsional irregularity and the limiting η_{bi} value is 1.2. There is torsional irregularity only in the X direction of the building (see Table 4.3). B2 is the soft story irregularity and the limiting η_{ki} value is 2.0. η_{ki} values for each floor are calculated as the ratios of interstory drift ratios of two consecutive floors. There is no soft story irregularity in either direction of the building (see Table 4.4). B3 is an in-plane discontinuity in vertical lateral force-resisting element irregularity. This irregularity does not exist in the building. β is 0.8 in the X direction and 0.9 in the Y direction. Amplification coefficients were calculated as 1.53 and 1.17 in the X and Y directions, respectively.

Table 4.4 Soft story irregularity coefficients in the X and Y direction for the as-built building.

	X direction				Y direction			
Floor	η_{ki}	Check	η_{ki}	Check	η_{ki}	Check	η_{ki}	Check
6	-	-	0.82	OK	-	-	0.93	OK
5	1.22	OK	0.88	OK	1.07	OK	0.96	OK
4	1.14	OK	1.03	OK	1.04	OK	1.02	OK
3	0.97	OK	1.06	OK	0.98	OK	1.16	OK
2	0.94	OK	1.67	OK	0.86	OK	1.32	OK
1	0.6	OK	1.93	OK	0.76	OK	1.56	OK
B1	0.52	OK	-	-	0.64	OK	-	-

The assessment of ductile beams, columns and shear walls was performed by comparing the demand-to-capacity ratios, r, with the limiting demand-to-capacity ratios, r_{limit}, defined for the assigned performance objective. Demand-to-capacity ratio is calculated by dividing the internal moment due to the earthquake loads, M_E, by the residual moment capacity, M_A, of the member. The residual moment capacity is the vectorial difference between the moment capacity at the end of the member and the internal moment calculated under gravity loads.

Limiting demand-to-capacity ratios for ductile beams depend on the reinforcement ratio, confinement and shear force as shown in Table 4.5. For ductile columns, they depend on the axial load ratio, confinement and shear force as shown in Table 4.6. For ductile shear walls, they depend on the confinement as shown in Table 4.7.

Table 4.5 Demand-to-capacity ratio limits for ductile beams.

Ductile Beam			Damage Limits (r_{limit})		
$\frac{\rho-\rho'}{\rho_b}$	Confinement	$\frac{V_e}{b_w d f_{ctm}}$	IO	LS	CP
≤0	Yes	≤0.65	3	7	10
≤0	Yes	≥1.3	2.5	5	8
≥0.5	Yes	≤0.65	3	5	7
≥0.5	Yes	≥1.3	2.5	4	5
≤0	No	≤0.65	2.5	4	6
≤0	No	≥1.3	2	3	5
≥0.5	No	≤0.65	2.5	4	6
≥0.5	No	≥1.3	1.5	2.5	4

Table 4.6 Demand-to-capacity ratio limits for ductile columns.

Ductile Column			Damage Limits (r_{limit})		
$\frac{N_k}{A_c f_{cm}}$	Confinement	$\frac{V_e}{b_w d f_{ctm}}$	IO	LS	CP
≤ 0.1	Yes	≤0.65	3	6	8
≤ 0.1	Yes	≥1.3	2.5	5	6
≥0.4 and ≤ 0.7	Yes	≤0.65	2	4	6
≥0.4 and ≤ 0.7	Yes	≥1.3	1.5	2.5	3.5
≤ 0.1	No	≤0.65	2	3.5	5
≤ 0.1	No	≥1.3	1.5	2.5	3.5
≥0.4 and ≤ 0.7	No	≤0.65	1.5	2	3
≥0.4 and ≤ 0.7	No	≥1.3	1	1.5	4
≥0.7	-	-	1	1	1

Table 4.7 Damage-to-capacity ratio limits for ductile shear walls.

Ductile Shear Walls	Damage Limits (r_{limit})		
Confinement	IO	LS	CP
Yes	3	6	8
No	2	4	6

First, beams were classified as ductile or brittle. If the shear demand on the beam, V_e, is less than the shear capacity, V_r, the beam is ductile; otherwise, brittle. Shear demand is a function of the end moment capacities and internal shear forces, and is calculated as shown in Figure 4.6. V_c is the shear capacity of concrete calculated per TS500 [Turkish Standards Institute 2000], M_c is the moment capacity at the beam ends and V_{dy} is the shear force due to gravity loads.

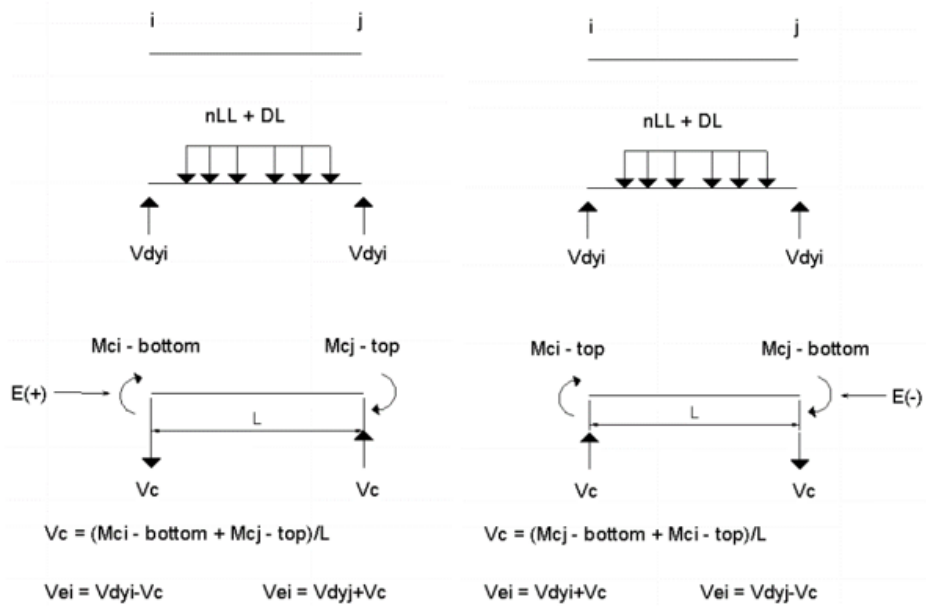

Figure 4.6 Shear demand calculation at the end of the beams.

The shear capacity of the beams is calculated by

$$V_r = 0.52 f_{ctm} b_w d + \frac{A_{sw}}{s} f_{ywm} d \tag{4.8}$$

where f_{ctm} is the tensile strength of concrete and f_{ywm} is the yield strength of the stirrup steel.

Figure 4.7 and Figure 4.8 present the demand-to-capacity ratios and compare them with the limiting values for the second-floor beams in the X and Y directions, respectively.

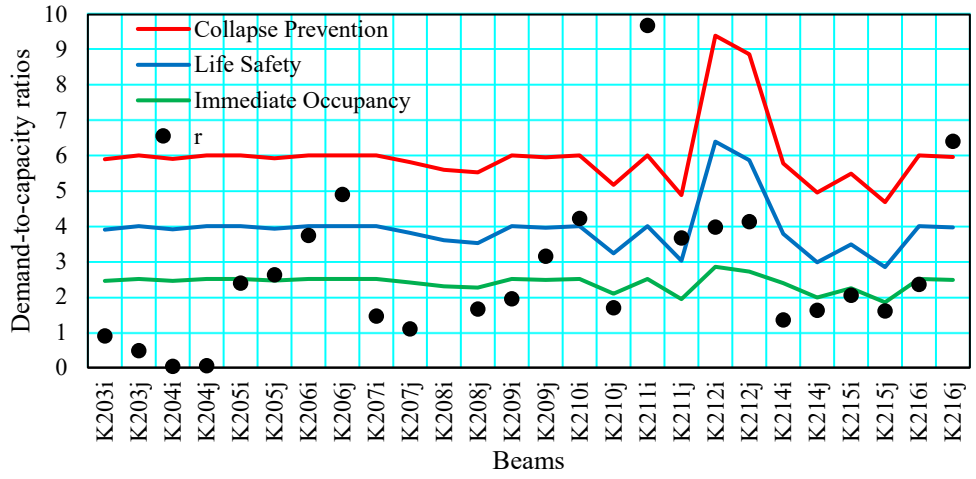

Figure 4.7 Demand-to-capacity ratios for the second-floor beams of the as-built building, X direction.

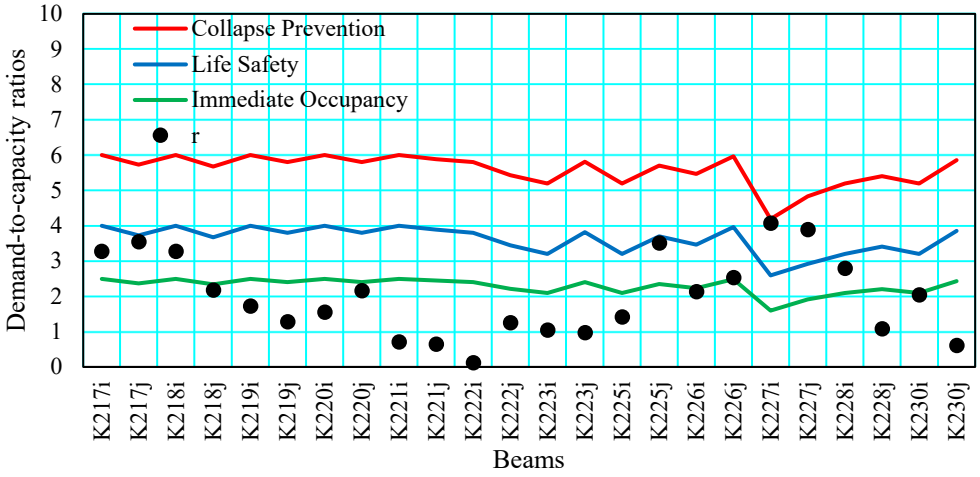

Figure 4.8 Demand-to-capacity ratios for the second-floor beams of the as-built building, Y direction.

Columns were also classified as ductile or brittle. If the shear demand on the column, V_e, is less than the shear capacity, V_r, the column is ductile; otherwise, brittle. Column shear capacity is calculated by

$$V_r = 0.52 f_{ctm} b_w d(1 + \gamma \frac{N_K}{A_c}) + \frac{A_{sw}}{s} f_{ywm} d \qquad (4.9)$$

where b_w is the width and d is the effective depth of column section, N_K is the axial load on column, A_c is the cross sectional area of column and A_{sw} is the transverse

reinforcement area. Figure 4.9 shows the elevation and section of column S19 and Table 4.8 tabulates the shear capacity of this column at each story.

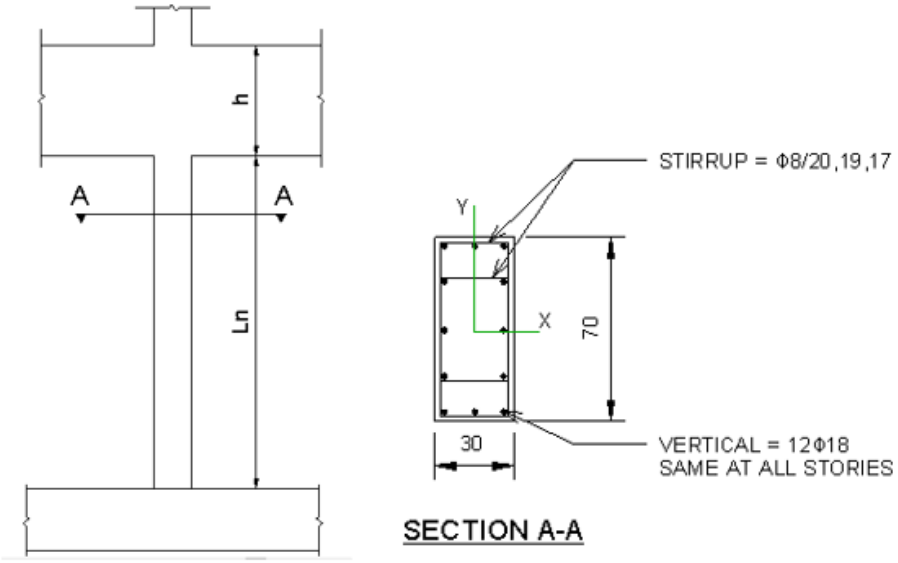

Figure 4.9 Elevation and section of column S19 (dimensions in cm).

Table 4.8 Shear capacity of column S19.

Column	bw (mm)	h (mm)	N (kN)	ϕ (mm)	s (mm)	γ	Vr (kN)
B1S19	700	300	718	8	200	0.07	318
1S19	700	300	610	8	200	0.07	312
2S19	700	300	497	8	200	0.07	306
3S19	700	300	389	8	190	0.07	306
4S19	700	300	288	8	170	0.07	314
5S19	700	300	188	8	170	0.07	308
6S19	700	300	86	8	170	0.07	303

The expected shear force for the column is calculated by

$$V_e = \frac{M_{bottom} + M_{top}}{l_n} \tag{4.10}$$

where M_{bottom} and M_{top} are the moments at the bottom and top of the column. The ductility check for column S19 is presented in Table 4.9.

Table 4.9 Ductility check for column S19.

	All moments in kNm						
	$M_{eq,bottom}$ (B1S19)	$M_{eq,top}$ (NA)	M_{bottom}	L_n (m)	V_e (kN)	V_r (kN)	Check
	353		162				
B1S19	$M_{eq,bottom}$ (1S19)	$M_{eq,top}$ (B1S19)	M_{top}	2.7	85	318	DUCTILE
	418	180	68				
	$M_{eq,bottom}$ (1S19)	$M_{eq,top}$ (B1S19)	M_{bottom}	Ln (m)	Ve (kN)	Vr (kN)	Check
	418	180	68				
1S19	$M_{eq,bottom}$ (2S19)	$M_{eq,top}$ (1S19)	M_{top}	2.7	75	312	DUCTILE
	347	211	135				
	$M_{eq,bottom}$ (2S19)	$M_{eq,top}$ (1S19)	M_{bottom}	Ln (m)	Ve (kN)	Vr (kN)	Check
	347	211	171				
2S19	$M_{eq,bottom}$ (3S19)	$M_{eq,top}$ (2S19)	M_{top}	3.1	102	306	DUCTILE
	204	175	141				
	$M_{eq,bottom}$ (3S19)	$M_{eq,top}$ (2S19)	M_{bottom}	Ln (m)	Ve (kN)	Vr (kN)	Check
	204	175	111				
3S19	$M_{eq,bottom}$ (4S19)	$M_{eq,top}$ (3S19)	M_{top}	3.1	46	306	DUCTILE
	186	154	29				
	$M_{eq,bottom}$ (4S19)	$M_{eq,top}$ (3S19)	M_{bottom}	Ln (m)	Ve (kN)	Vr (kN)	Check
	186	154	29				
4S19	$M_{eq,bottom}$ (5S19)	$M_{eq,top}$ (4S19)	M_{top}	3.1	20	314	DUCTILE
	142	137	32				
	$M_{eq,bottom}$ (5S19)	$M_{eq,top}$ (4S19)	M_{bottom}	Ln (m)	Ve (kN)	Vr (kN)	Check
	142	137	32				
5S19	$M_{eq,bottom}$ (6S19)	$M_{eq,top}$ (5S19)	M_{top}	3.1	20	308	DUCTILE
	130	105	29				
	$M_{eq,bottom}$ (6S19)	$M_{eq,top}$ (5S19)	M_{bottom}	Ln (m)	Ve (kN)	Vr (kN)	Check
	130	105	29				
6S19	$M_{eq,bottom}$ (NA)	$M_{eq,top}$ (6S19)	M_{top}	3.1	34	303	DUCTILE
		130	77				

The assessment of ductile columns and shear walls was performed as follows. First, the interaction diagram was constructed. Then, axial load and moment values under the earthquake load (N_e, M_e) and gravity load (N_d, M_d) were marked on the interaction diagram. A line was drawn between these axial load and moment pairs. The axial load and moment capacity pair (N_k, M_k) was marked at the intersection of this line with the interaction diagram. Finally, the residual axial load and moment (N_a, M_a) capacity pairs were calculated as the vectorial difference between the capacity pair values (N_k, M_k) and the gravity pair values (N_d, M_d). Demand-to-capacity ratio for ductile columns was calculated by

$$r = \frac{M_E}{M_A} = \frac{N_E}{N_A} \tag{4.11}$$

Figure 4.10 shows the demand-to-capacity ratio calculation for column S19 for floor B1 and Figure 4.11 presents the demand-to-capacity ratios of column S19 and compares them with limiting values.

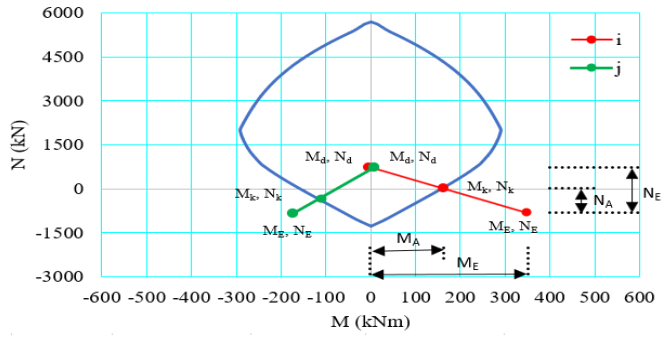

Figure 4.10 Demand-to-capacity ratio calculation for column S19 at floor B1.

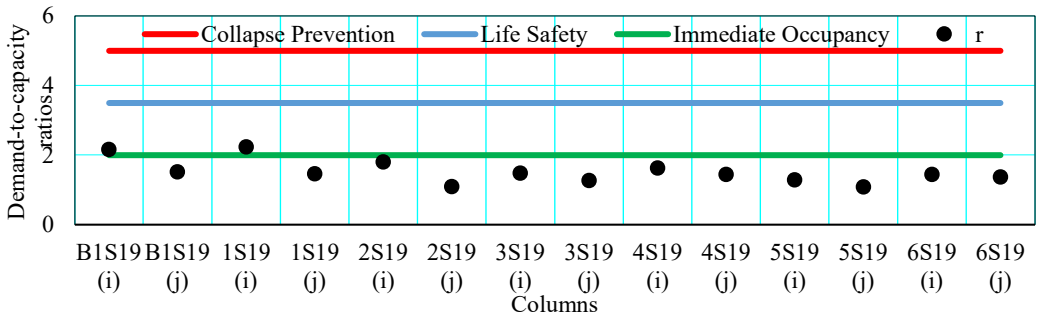

Figure 4.11 Demand-to-capacity ratios for column S19 of the as-built building.

Figure 4.12 and Figure 4.13 summarize the beam assessment in the +Y and +X directions, respectively. As more than 10% of the beams sustained significant damage, the IO performance objective was not satisfied for the beams.

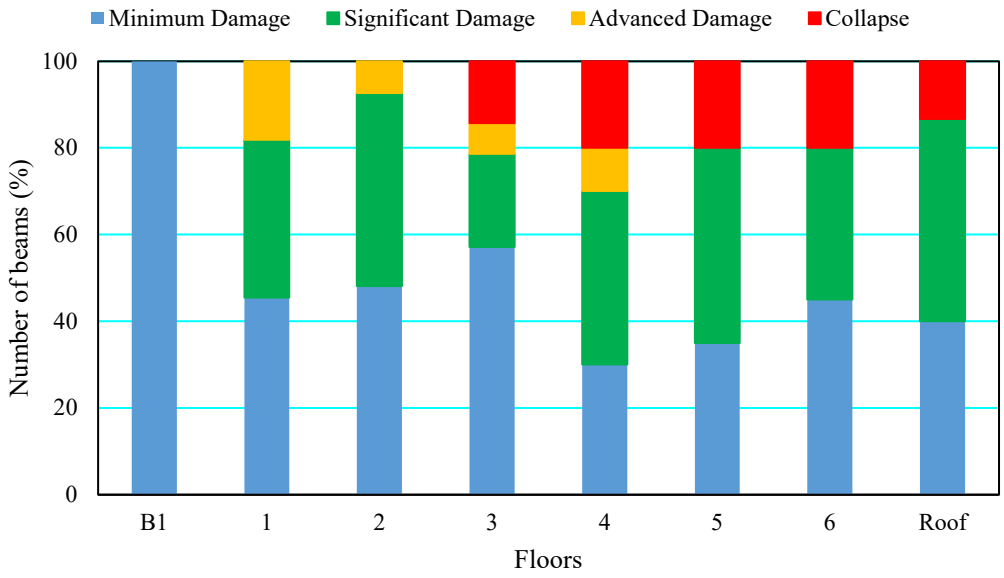

Figure 4.12 As-built building beam assessment for +Y direction.

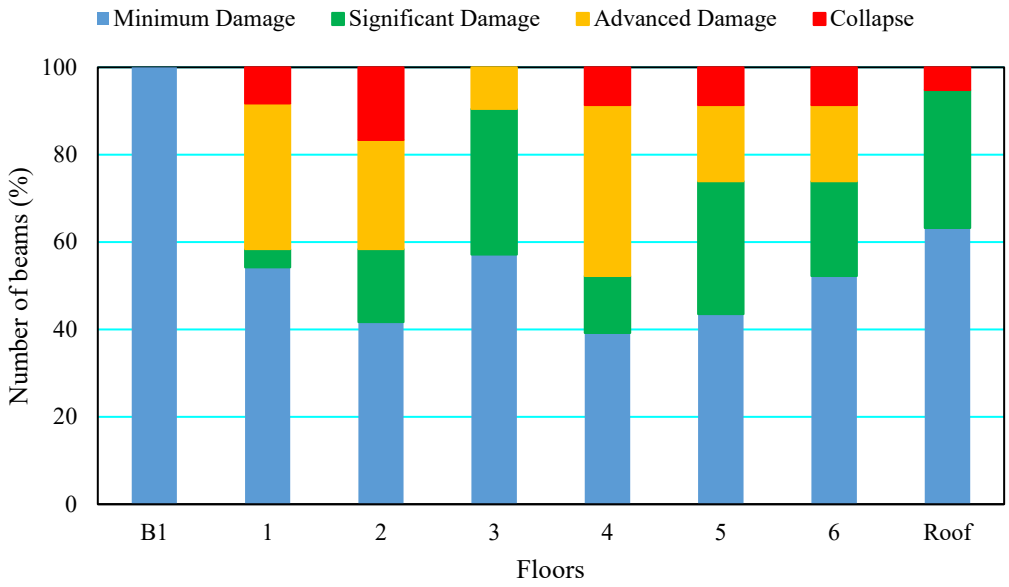

Figure 4.13 As-built building beam assessment for +X direction.

Figure 4.14 and Figure 4.15 summarize the column assessment for the +Y and +X directions, respectively. Since several columns sustained significant or advanced damage, the IO performance objective was not satisfied for the columns.

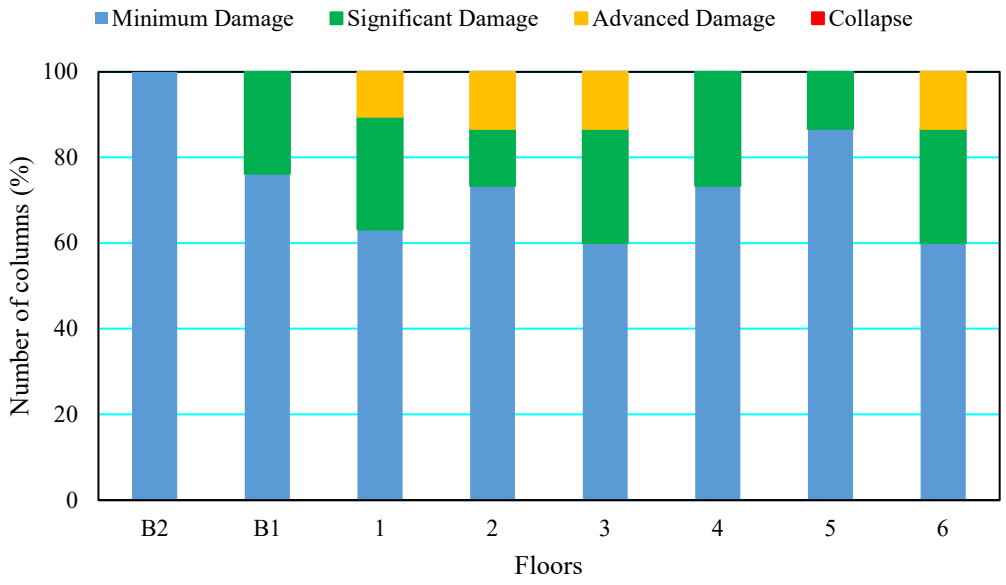

Figure 4.14 As-built building column assessment for +Y direction.

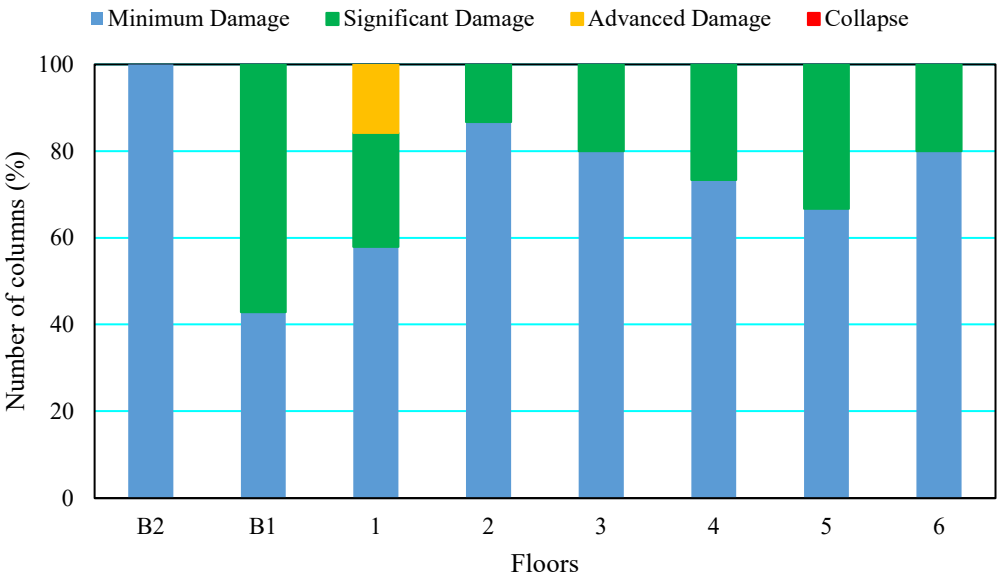

Figure 4.15 As-built building column assessment for +X direction.

Figure 4.16 and Figure 4.17 summarize the shear wall assessment for +Y and +X directions, respectively. Since most of the shear walls sustained significant damage, the IO performance objective was not satisfied for the shear walls.

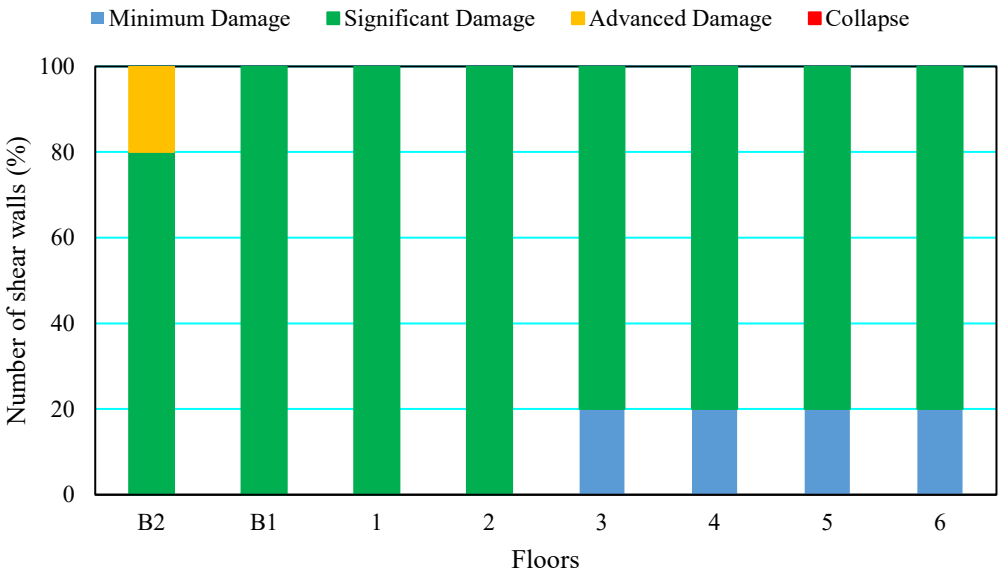

Figure 4.16 As-built building shear wall assessment for +Y direction.

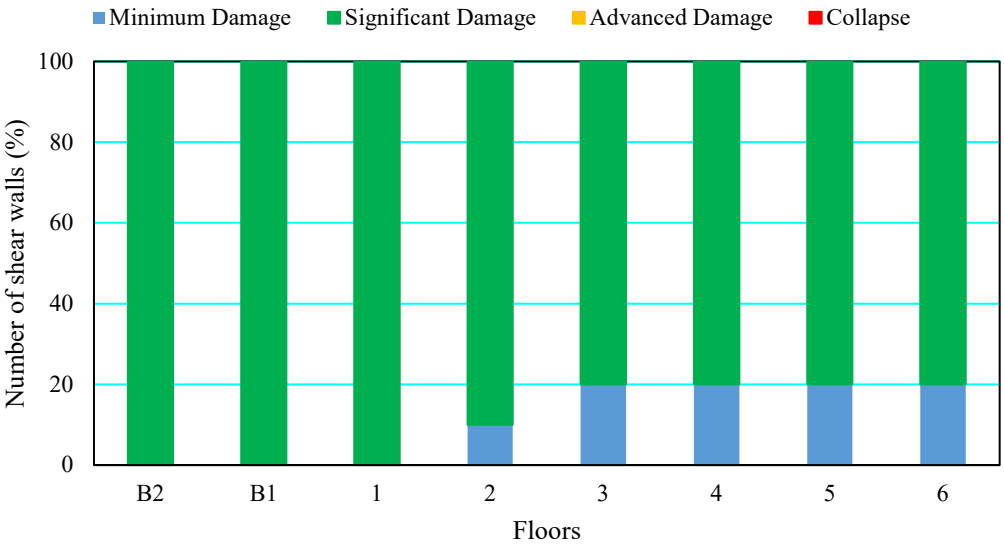

Figure 4.17 As-built building shear wall assessment for +X direction.

IO performance limit for interstory drift ratio is defined as 1%. Figure 4.18 presents the building interstory drifts in the +X and +Y directions. The as-built building does not satisfy the IO performance objective for interstory drift.

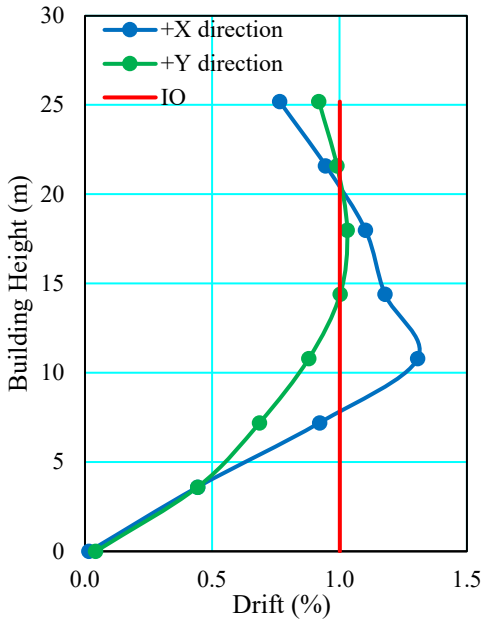

Figure 4.18 Seismic assessment of the as-built building based on interstory drifts.

Beam, column, shear wall and drift criteria were not satisfied for the IO performance objective. Thus, the as-built building did not have satisfactory performance for the IO performance objective.

LS performance objective does not allow any of the structural members sustain collapse under the MCE. As several structural members sustain collapse under the DBE, it can be concluded that the as-built building did not have satisfactory performance for the LS performance objective.

To sum up, the as-built state of the building did not satisfy the IO and LS performance objectives. Therefore, the retrofit decision for the as-built building was verified.

4.3 Post-Retrofit Building

4.3.1 Linear assessment per MPWS [2007]

In the linear seismic assessment of the post-retrofit building, similar steps were followed. During the retrofit, the objective was to support all lateral loads with the newly added RC shear wall system, ignoring the contribution of the boundary frame. To do so, minimum anchor reinforcement was provided between the boundary column and the infill. Hence, boundary columns were not considered in the seismic assessment.

In the finite element analysis, model #8 (see Chapter 3) was used as the base model. The contribution of partition walls was not considered. Effective section stiffness multipliers were incorporated. Table 4.10 presents the natural vibration periods and modal mass participation ratios.

Table 4.10 Natural vibration periods and modal mass participation ratios for the post-retrofit building per [MPWS 2007].

Mode	Natural vibration period (s)	Modal mass participation ratios (%)		
		x (E-W)	y (N-S)	θ
1	0.28	-	63	-
2	0.25	41	-	22
3	0.23	17	-	29

The post-retrofit overall height of the building is 18 m and the number of total floors is 6. The torsional irregularity coefficient, η_{bi}, was calculated as 1.71 in the X direction (see Table 4.11). Hence, linear elastic response spectrum analysis was performed for earthquake load analysis.

Table 4.11 Torsional irregularity coefficient in the X and Y directions for the post-retrofit building.

	X direction		Y direction	
Floor	η_{bi}	Check	η_{bi}	Check
Roof	1.02	OK	1.00	OK
4	1.10	OK	1.00	OK
3	0.99	OK	1.00	OK
2	1.06	OK	1.00	OK
1	1.71	NO GOOD	1.00	OK
B1	1.27	OK	1.00	OK

For the post-retrofit building, the base shear calculated per the equivalent lateral force procedure is 37000 kN in both directions. The base shear calculated per the response spectrum analysis is 21000 kN and 24000 kN in the X and Y directions, respectively. In the response spectrum analysis, 24 modes were used to achieve 90% mass participation in both directions.

There is torsional irregularity only in the X direction of the building (see Table 4.11), no soft story irregularity in either direction of the building, and no in-plane discontinuity in vertical lateral force-resisting element irregularity. β is 0.8 in the X direction and 0.9 in the Y direction. Amplification coefficients were calculated as 1.59 and 1.23 in the X and Y directions, respectively

Figure 4.19 and Figure 4.20 present the demand-to-capacity ratios and compare them with the limiting values for the second-floor beams in X and Y directions, respectively. Seismic assessment was performed for examining the IO performance objective under the DBE.

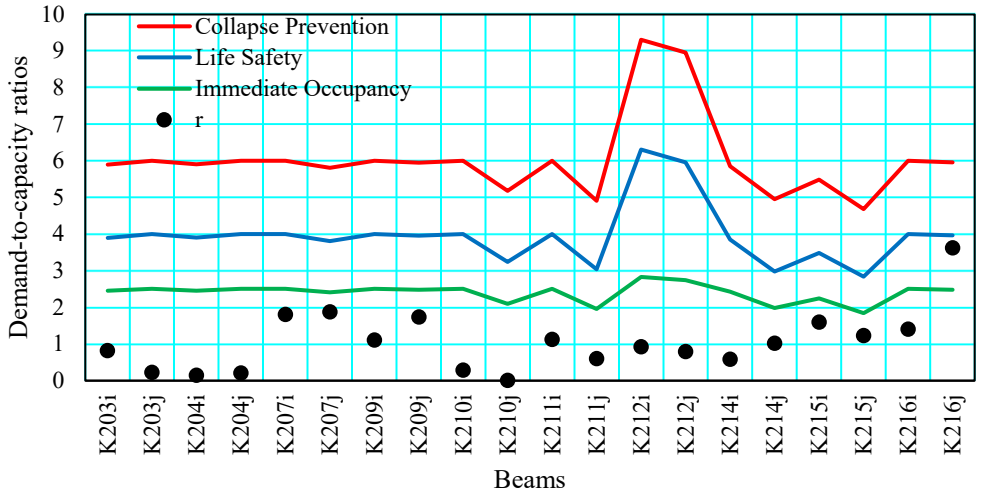

Figure 4.19 Demand-to-capacity ratios for the second-floor beams of the post-retrofit building, X direction.

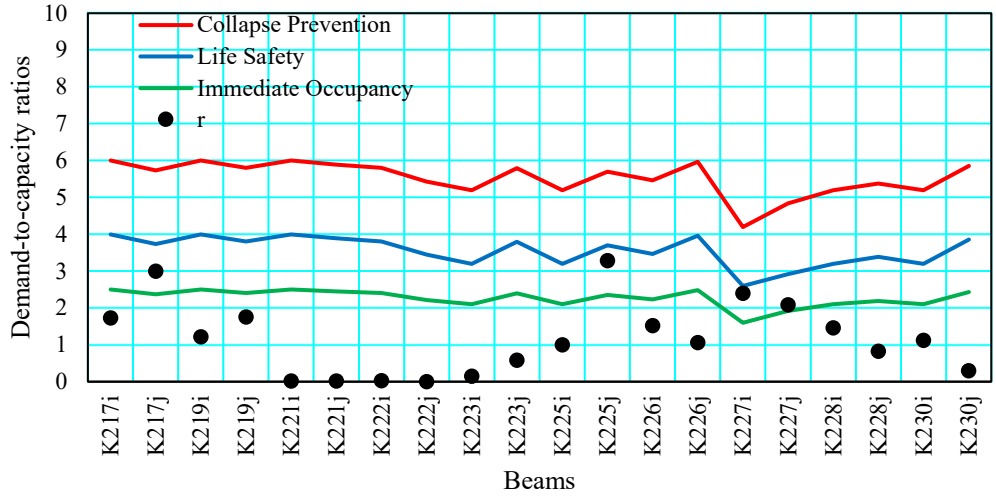

Figure 4.20 Demand-to-capacity ratios for the second-floor beams of the post-retrofit building, Y direction.

Figure 4.21 shows seismic demand-to-capacity ratio calculation for column S16 on the first floor. i and j are top and bottom ends of the column, respectively. Axial load and moment values under the earthquake load (N_e, M_e) is within the interaction diagram. Thus, this column shows satisfactory performance. Figure 4.22 presents the demand-to-capacity ratios of column S16 and compare them with limiting values.

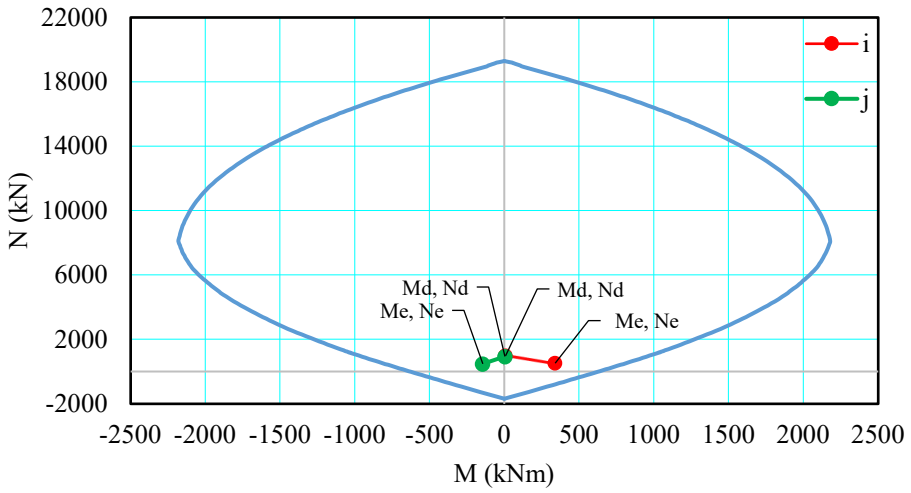

Figure 4.21 Demand-to-capacity ratio calculation for column S16 on the first floor.

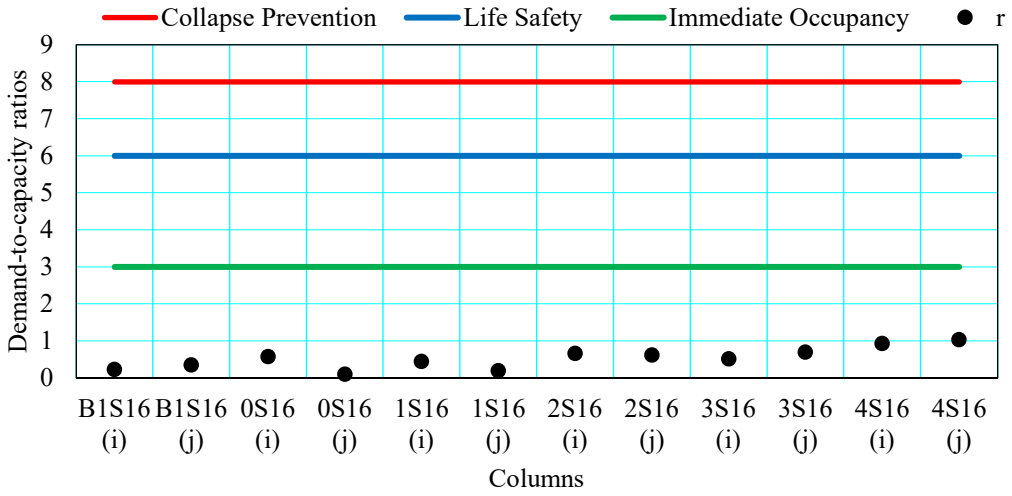

Figure 4.22 Demand-to-capacity ratio for column S16 of the post-retrofit building.

Figure 4.23 shows shear wall PB11' assessment on the second floor. i and j are top and bottom ends of the shear wall, respectively. Figure 4.24 shows shear wall PB11' assessment results for all floors.

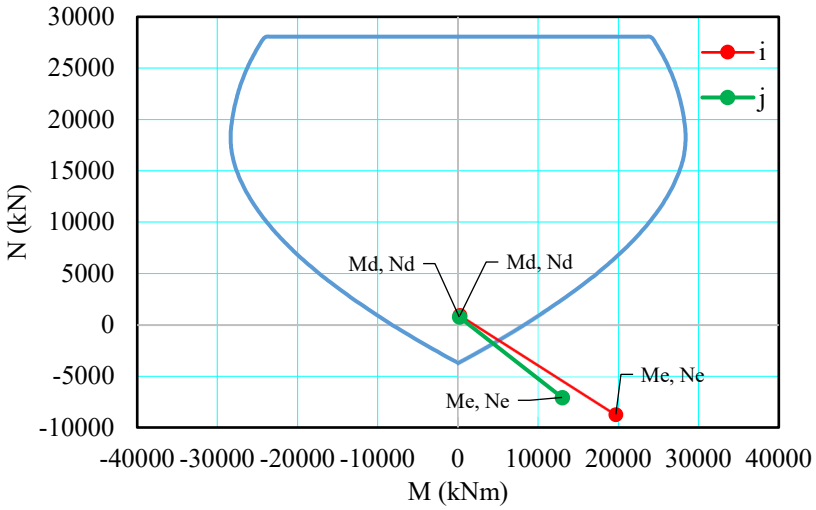

Figure 4.23 Demand-to-capacity ratio calculation for column PB11' on the second floor.

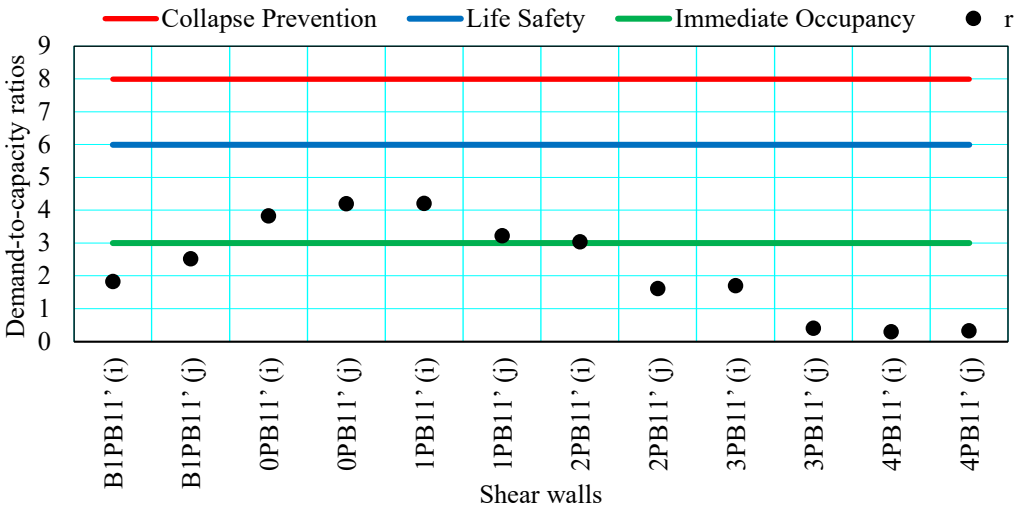

Figure 4.24 Demand-to-capacity ratio for shear wall PB11' of the post-retrofit building.

Figure 4.25 and Figure 4.26 summarize the beam assessment in the +Y and +X directions, respectively. As more than 10% of the beams sustained significant damage, the IO performance objective was not satisfied for the beams.

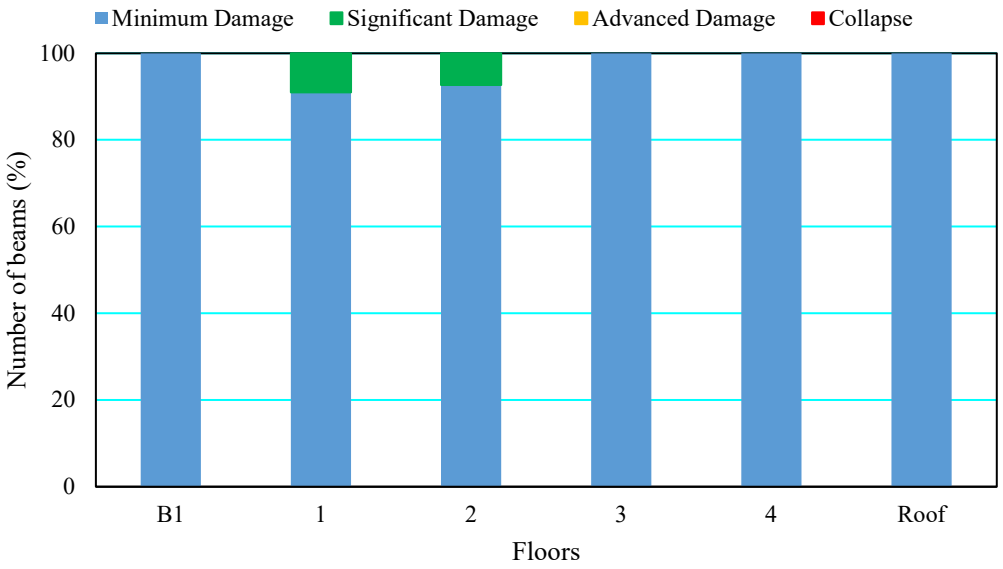

Figure 4.25 Post-retrofit building beam assessment for +Y direction.

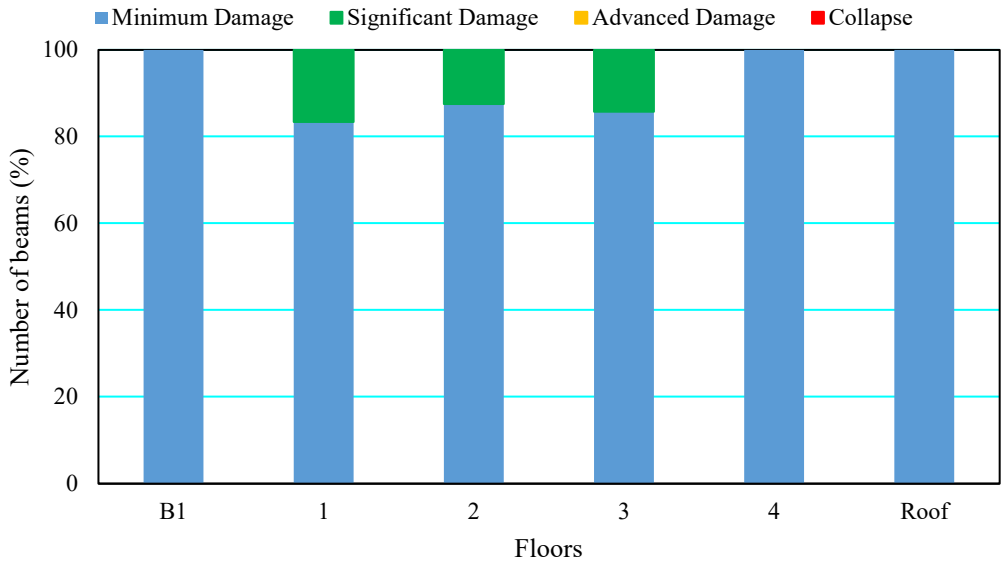

Figure 4.26 Post-retrofit building beam assessment for +X direction.

Figure 4.27 and Figure 4.28 summarize the column assessment for +Y and +X directions, respectively. As none of the columns sustained critical damage, the IO performance objective was satisfied for the columns.

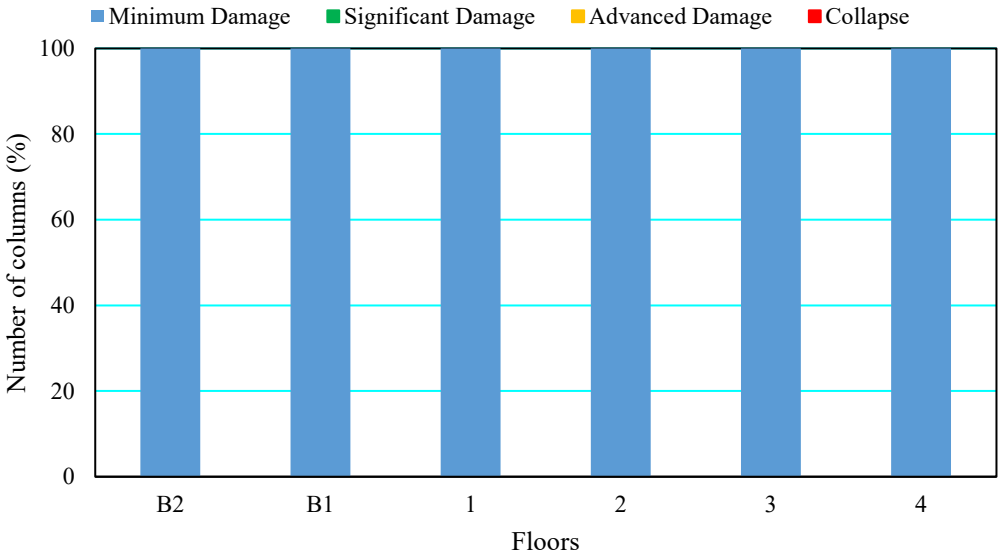

Figure 4.27 Post-retrofit building column assessment for +Y direction.

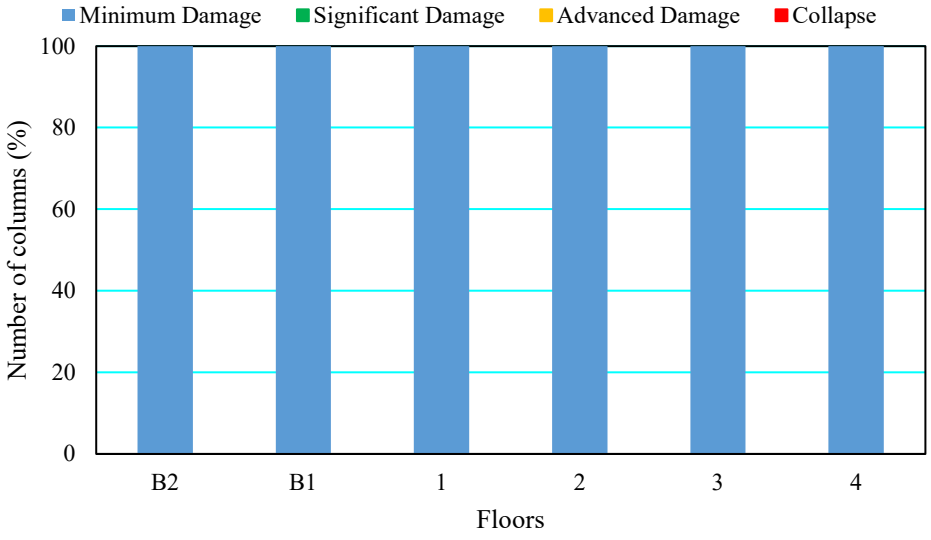

Figure 4.28 Post-retrofit building column assessment for +X direction.

Figure 4.29 and Figure 4.30 summarize the shear wall assessment for +Y and +X directions, respectively. Since most of the shear walls sustained significant damage, the IO performance objective was not satisfied for the shear walls.

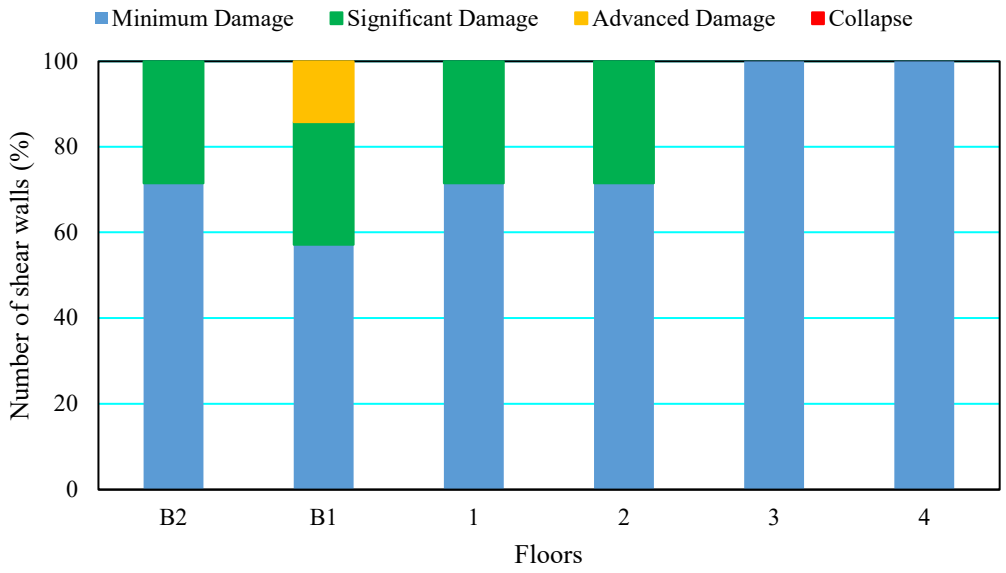

Figure 4.29 Post-retrofit building shear wall assessment for +Y direction.

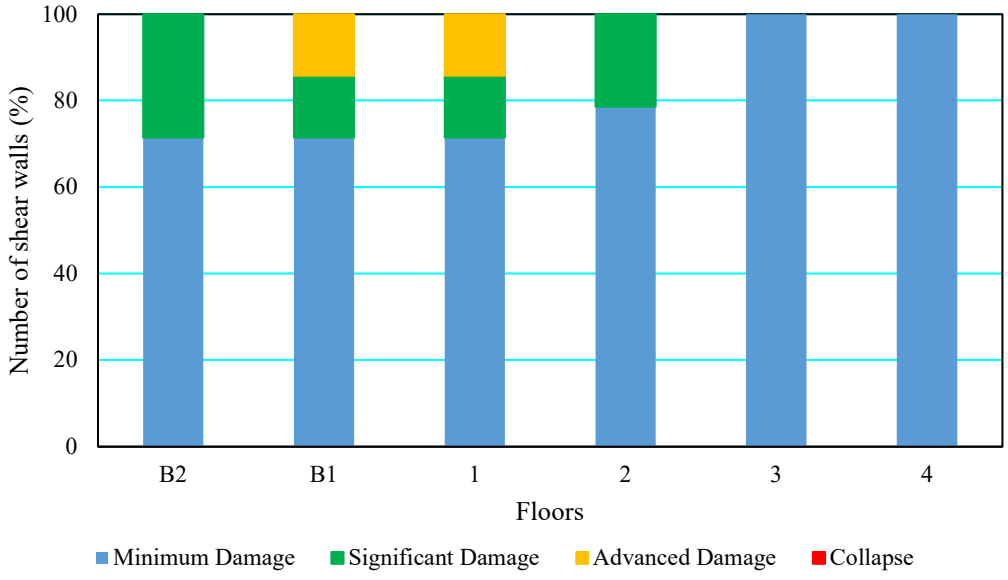

Figure 4.30 Post-retrofit building shear wall assessment for +X direction.

Figure 4.31 presents the building interstory drifts in the +X and +Y directions. The post-retrofit building satisfied the IO performance objective for interstory drift.

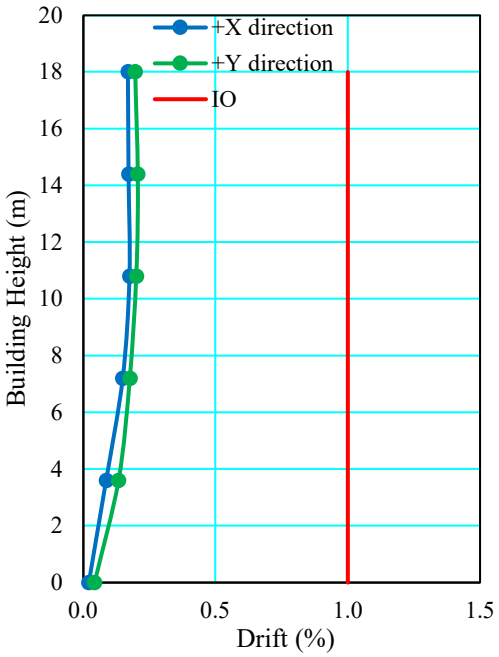

Figure 4.31 Seismic assessment of the post-retrofit building based on interstory drifts.

Column and drift criteria were satisfied for the IO performance objective. However, beam and shear walls did not satisfy the IO performance objective. Hence, the post-retrofit building did not have satisfactory performance for the IO performance objective.

LS performance objective does not allow any of the shear walls sustain significant damage under the MCE. As several of the shear walls sustain significant damage under the DBE, it can be concluded that the post-retrofit building did not have satisfactory performance for the LS performance objective.

4.3.2 Nonlinear assessment per AFAD [2018]

To perform linear assessment per AFAD [2018] all of the following requirements shall be satisfied.

- Building Height Class (BHC) shall not be smaller than 5. BHC is 5 for the post-retrofit building. Thus, this requirement is satisfied.
- There should not be any discontinuity of vertical elements (B3 irregularity). There is no such irregularity in the post-retrofit building.
- On any floor other than the top floor of the building, the average demand-to-capacity ratio scaled by the shear force of the vertical ductile elements shall not be greater than the average demand-to-capacity ratio of the beams. This requirement is not satisfied for the first three floors.

Thus, the linear assessment was not performed for the post-retrofit building.

To perform pushover analysis, modal mass participation in principal modes shall be at least 70%, which is not satisfied (see Table 4.10). Thus, pushover analysis was not performed for the post-retrofit building.

4.3.2.1 Selection of Earthquake Ground Motions

Earthquake ground motions were selected by considering the earthquake magnitudes, fault distances, source mechanisms and local soil conditions. Past earthquake records from the building location were selected first. Maximum three records from the same earthquake are allowed.

The building under investigation is in Gerede, Bolu, a seismically active region controlled by the North Anatolian Fault, which is a strike slip fault [Jackson and McKenzie 1984]. This fault is literally astride of the building [Celik and Gulkan 2021]. Thus, fault distances smaller than 10 km were considered. Soil profile of the building is consisting of dense sand and clay [Gulkan et al. 1994]. The shear wave velocity $(V_s)_{30}$ is between 180–360 m/s. Earthquakes with moment magnitudes of

M_w 6.5–7.9 were considered. With these criteria, unscaled ground motions were selected from the PEER NGA-West2 ground motion database (http://ngawest2.berkeley.edu) and presented in Table 4.12. Peak ground accelerations for the selected grounds motions range from 0.12 to 0.82 g.

Table 4.12 Selected earthquake ground motion records per AFAD [2018].

Earthquake #	Record Sequence Number (RNS)	Earthquake Name	Year	Station Name	Magnitude	Mechanism	R_{rup} (km)	$(V_s)_{30}$ (m/s)
1	1602	"Duzce_ Turkey"	1999	"Bolu"	7.1	strike slip	12.0	294
2	6	"Imperial Valley-02"	1940	"El Centro Array #9"	7.0	strike slip	6.1	213
3	160	"Imperial Valley-06"	1979	"Bonds Corner"	6.5	strike slip	2.7	223
4	181	"Imperial Valley-06"	1979	"El Centro Array #6"	6.5	strike slip	1.4	203
5	182	"Imperial Valley-06"	1979	"El Centro Array #7"	6.5	strike slip	0.6	211
6	723	"Superstition Hills-02"	1987	"Parachute Test Site"	6.5	strike slip	1.0	349
7	821	"Erzican_ Turkey"	1992	"Erzincan"	6.7	strike slip	4.4	352
8	1176	"Kocaeli_ Turkey"	1999	"Yarimca"	7.5	strike slip	4.8	297
9	1605	"Duzce_ Turkey"	1999	"Duzce"	7.1	strike slip	6.6	282
10	1615	"Duzce_ Turkey"	1999	"Lamont 1062"	7.1	strike slip	9.1	338
11	2114	"Denali_ Alaska"	2002	"TAPS Pump Station #10"	7.9	strike slip	2.7	329

During the service life of the building, the largest earthquake within the proximity of the building occurred in Duzce (40.806° N, 31.187° E) on 12 November 1999 with a moment magnitude of M_w 7.1 [AFAD-TADAS 2022]. The epicenter of the earthquake is 84 km away from the building. The nearest strong ground motion station (#1401) that recorded the Duzce earthquake was in Bolu, which is 36 km away from the epicenter and 49 km away from the building (see Figure 4.32). This is the strongest earthquake ground motion recorded in the proximity to the building. Thus, this record was selected first and listed in Table 4.12. R_{rup} is the closest distance to the earthquake rupture plane (km). Figure 4.33 shows the unscaled

(square root of the sum of squares, SRSS) elastic 5% damped response spectra for the selected 11 ground motions. Time step sizes for these records were 0.005 and 0.01 s.

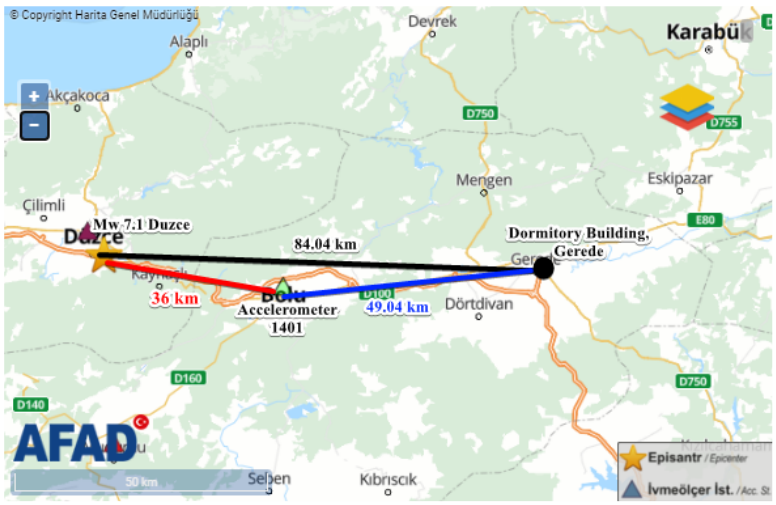

Figure 4.32 Epicenter of the 1999 M_w 7.1 Duzce earthquake and the nearest strong ground motion station.

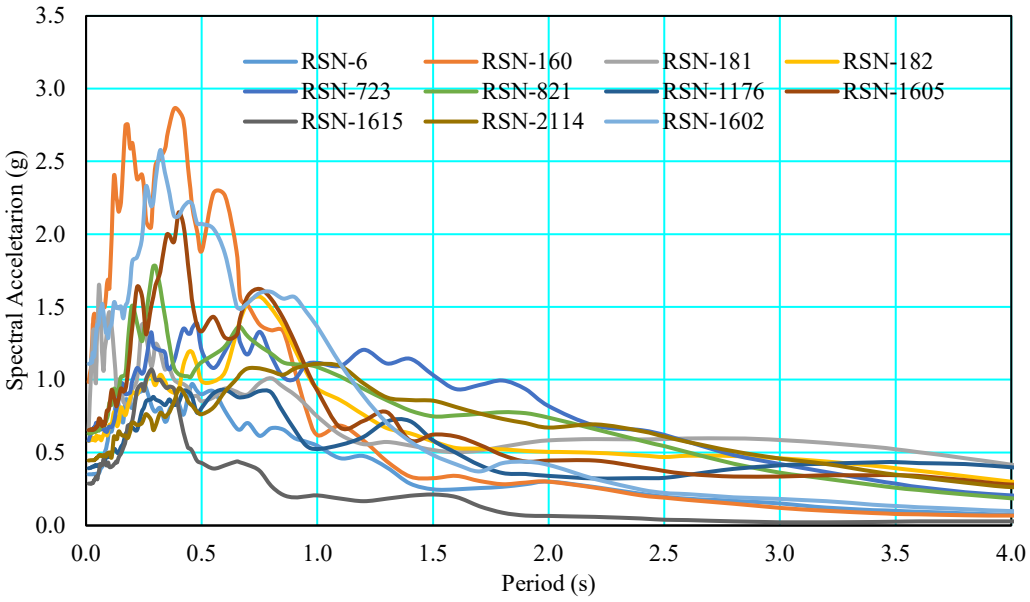

Figure 4.33 SRSS unscaled elastic 5% damped response spectra for 11 selected ground motions.

Figure 4.34 shows the N-S and E-W components of the 1999 M_w 7.1 Duzce earthquake recorded in Bolu station #1401 (RNS1602). Peak ground accelerations

are 0.74 g and 0.82 g in the N-S and E-W directions, respectively. The length of the records is 56 s. Figure 4.35 shows the elastic 5% damped spectral accelerations.

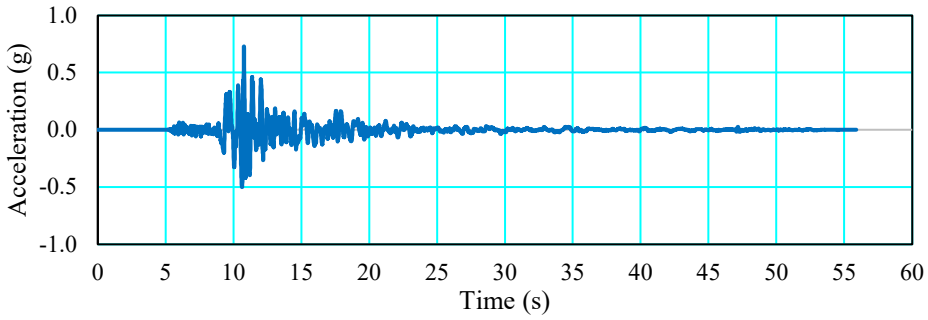

(a)

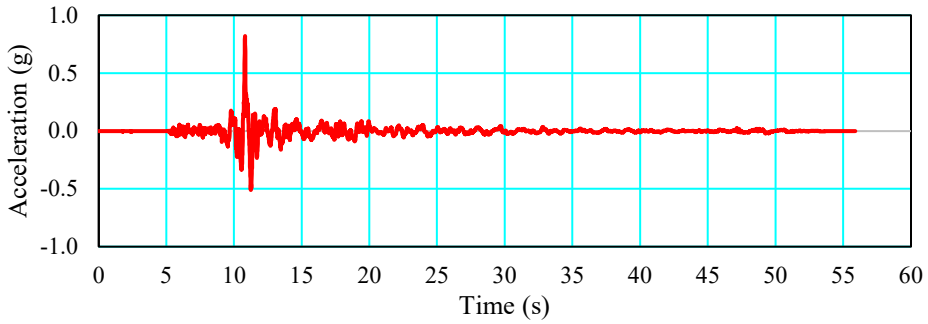

(b)

Figure 4.34 (a) N-S and (b) E-W components of the 1999 M_w 7.1 Duzce earthquake record (Bolu station #1401).

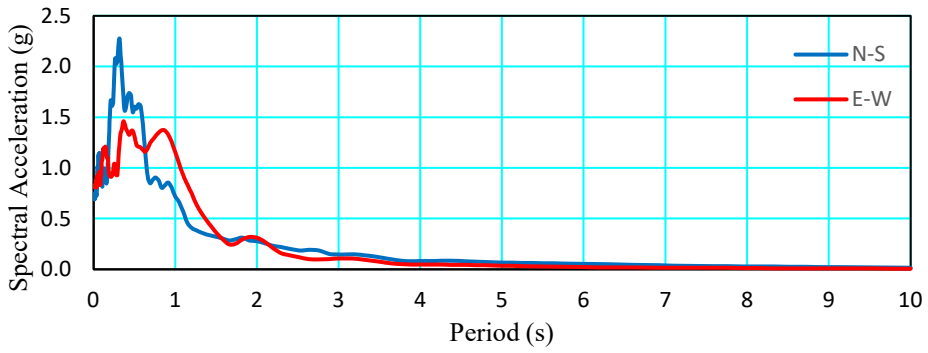

Figure 4.35 Elastic 5% damped response spectra of the 1999 M_w 7.1 Duzce earthquake record (Bolu station #1401).

Arias intensity, which is a measure of the strength of a ground motion, is given by

$$I_A = \frac{\pi}{2g}\int_0^{t_f} \ddot{u}^2\, dt \tag{4.12}$$

where g is the acceleration of gravity, ü is the ground motion acceleration, and t_f is the final time [Arias 1970]. Figure 4.36 shows the normalized Aris intensities for the N-S and E-W components of the 1999 M_w 7.1 Duzce earthquake record (Bolu station #1401).

To shorten the analysis time for the nonlinear time history analysis (NTHA) presented subsequently, ground motions were truncated when both components achieve their 99.5% of Arias intensities, which is calculated as 38 s. This calculation was repeated for all selected ground motions.

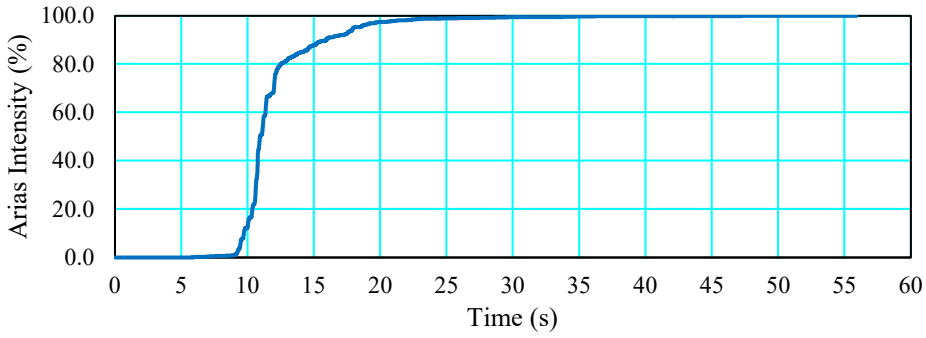

(a)

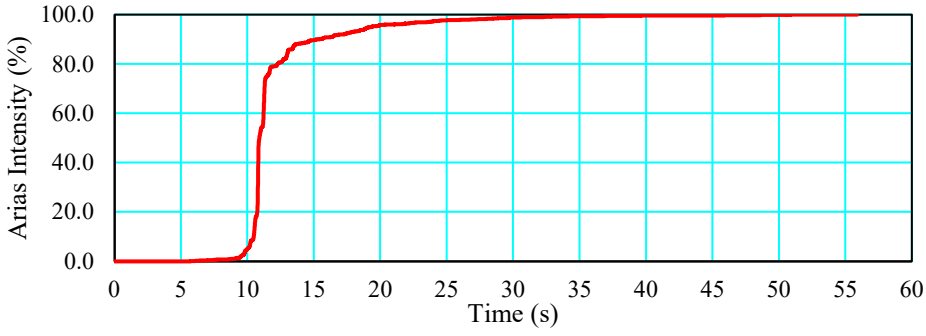

(b)

Figure 4.36 (a) N-S and (b) E-W components of the Arias Intensity (%) - time curves for the 1999 M_w 7.1 Duzce earthquake record (Bolu station #1401)

4.3.2.2 Section limit states and damage regions

There are three new limit states for ductile sections defined in AFAD [2018]. LD, CD and CP stand for limited damage, controlled damage and collapse prevention. LD and CD limit states are equivalent to the IO and LS used in MPWS [2007], respectively. Thus, for consistency, IO, LS and CP limit state definitions will be used.

4.3.2.3 Performance objectives

Performance objectives defined in AFAD [2018] depend on the building occupancy class, short period design spectral acceleration coefficient (S_{DS}) for the DD-2 earthquake and building height, H_N. The building is a dormitory; hence, the building occupancy class is 1 and the building importance factor is 1.5. S_{DS} is 1.652 for the DD-2 earthquake; hence, the seismic design class is 1a. H_N is 18 m; hence, the building height class is 5. Two applicable advanced performance objectives are defined for the building: LD under the DD-3 earthquake and CD under the DD-1 earthquake, which are equivalent to IO and LS performance objectives in MPWS [2007], respectively.

In IO performance objective, maximum 20% of the beams can sustain significant damage. All other vertical members shall sustain minimum damage. In LS performance objective, maximum 35% of the beams can sustain advanced damage. Additionally, maximum 35% of the vertical members can sustain advanced damage.

4.3.2.4 Material modeling

The concrete grade is C25 and the steel grade is S420 for all structural members. In the assessment, expected material strengths are to be used. Expected strength for concrete and steel are 32.5 MPa and 504 MPa, respectively. For the nonlinear concrete model, Mander et al. [1988] is used to account for the effect of concrete

confinement as shown in Figure 4.37. Table 4.13 presents the nonlinear rebar model parameters and Figure 4.38 shows the nonlinear rebar model.

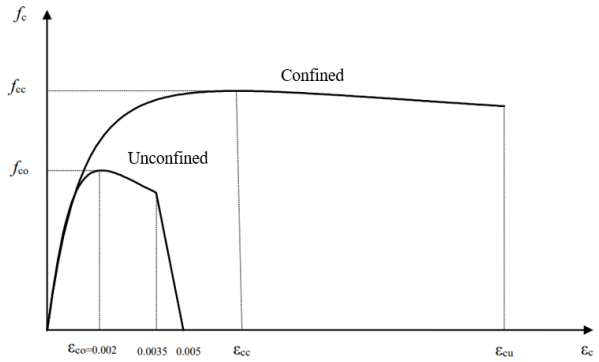

Figure 4.37 Nonlinear unconfined and confined concrete models [AFAD 2018].

Table 4.13 Nonlinear rebar model parameters.

Grade	f_{sye} (MPa)	ε_{sy}	ε_{sh}	ε_{su}	f_{sue}/f_{sye}
S420	504	0.0021	0.008	0.08	1.25

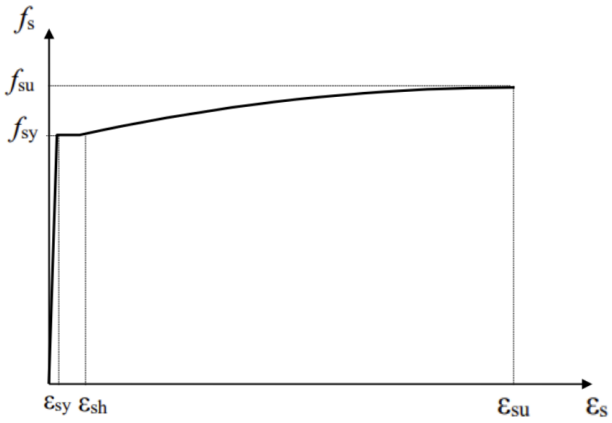

Figure 4.38 Nonlinear rebar model [AFAD 2018].

Limiting concrete strains for the CP, LS and IO limit states are defined in Equations 4.12–4.14, respectively. These limits depend on the confinement of the member. Figure 4.39 shows the second-floor beam strain limits. Due to the old construction practice, it can be seen that most of the beams are unconfined. Figure 4.40 shows the nonlinear concrete model and limit states for column S16, which is strengthened during the retrofit.

$$\varepsilon_c^{(CP)} = 0.0035 + 0.07\sqrt{\omega_{we}} \leq 0.018 \tag{4.13}$$

where ω_{we} is an effective confinement reinforcement mechanical ratio.

$$\varepsilon_c^{(LS)} = 0.75\varepsilon_c^{(CP)} \tag{4.14}$$

$$\varepsilon_c^{(IO)} = 0.0025 \tag{4.15}$$

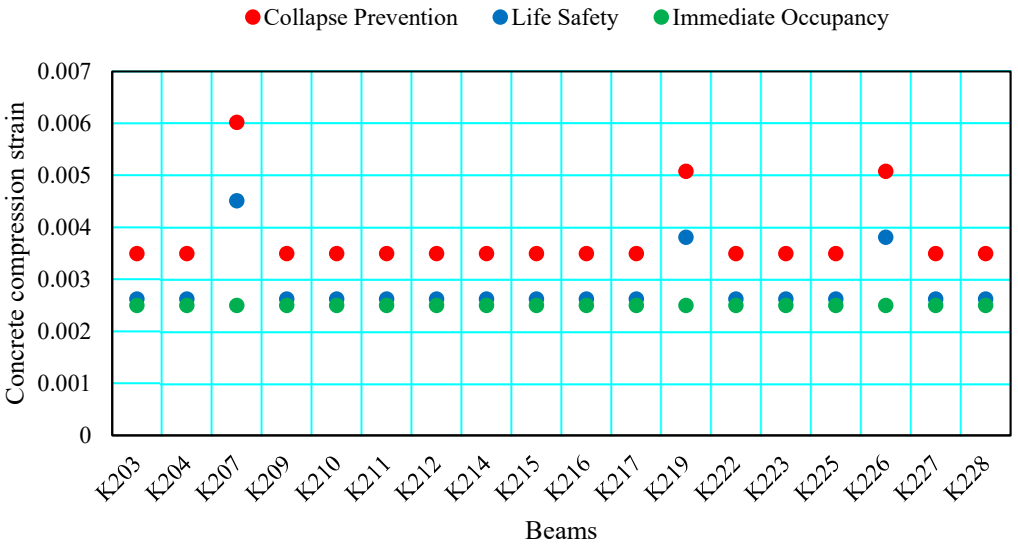

Figure 4.39 Limiting concrete strains for the second floor beams.

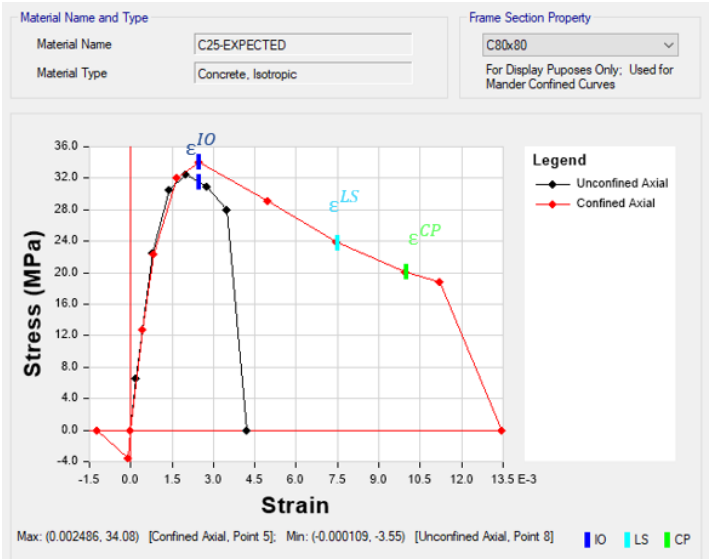

Figure 4.40 Expected concrete unconfined and confined models for S16 column.

Limiting steel strains for the CP, LS and IO limit states are defined in Equations 4.16–4.18, respectively and are shown in Figure 4.41.

$$\varepsilon_S^{(CP)} = 0.4\varepsilon_{su} \tag{4.16}$$

$$\varepsilon_S^{(LS)} = 0.75\varepsilon_S^{(CP)} \tag{4.17}$$

$$\varepsilon_c^{(IO)} = 0.0075 \tag{4.18}$$

where ε_{su} is the ultimate strain of the steel reinforcement.

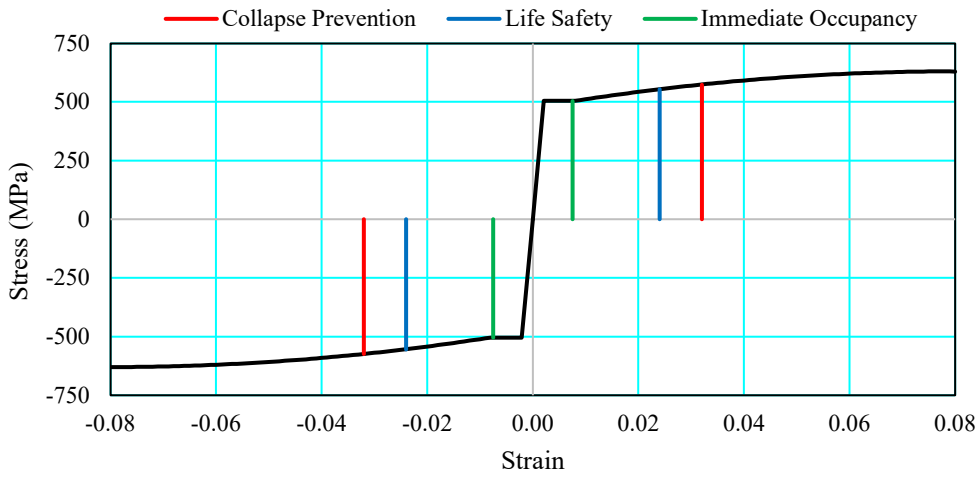

Figure 4.41 Nonlinear rebar model and the limiting steel strains.

4.3.2.5 Finite element structural modeling

There are two methods defined in AFAD [2018] for nonlinear modeling of structural members: lumped and distributed plasticity methods. In lumped plasticity models, end regions of structural elements are modeled as potential plastic hinges capable of resisting effective yield moment M_y and undergoing plastic rotations. Intermediate elements are modeled as elastic with effective section rigidities (see Figure 4.42). The damage limits defined for the rotation of these nonlinear hinge models are given by

$$\theta^{(CP)} = \frac{2}{3}\left[(\phi_u - \phi_y)L_p\left(1 - 0.5\frac{L_p}{L_s}\right) + 4.5\phi_u d_b\right] \quad (4.19)$$

$$\theta^{(LS)} = 0.75\theta^{(CP)} \quad (4.20)$$

$$\theta^{(IO)} = 0 \quad (4.21)$$

where ϕ_u is the ultimate curvature, ϕ_y is the yield curvature, L_p is the plastic hinge length, L_s is the shear span and d_b is the average diameter of the longitudinal reinforcement. L_p was defined equal to half of the cross-sectional dimension h of the beam ($L_p = 0.5h$). L_s was defined as half the clear span of the beam. Moment-curvature curves for all beam sections were computed using SAP2000 [Computers and Structures 2020].

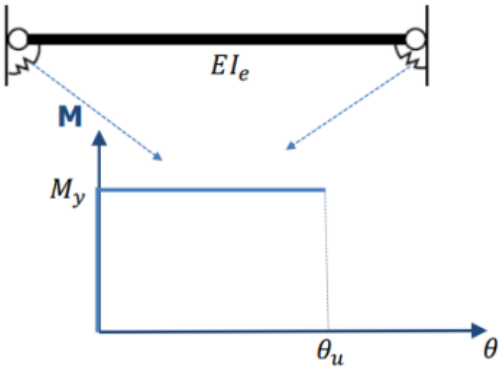

Figure 4.42 Lumped plasticity model.

The idealized moment-curvature of a section was obtained by minimizing the ratio of the area under the actual and idealized moment-curvature curves. Figure 4.43 shows the actual and idealized moment-curvature curves for beam K117. The plastic hinge model for beam K117 is given in Figure 4.44. Takeda et al. [1970] was used for the hysteretic behavior.

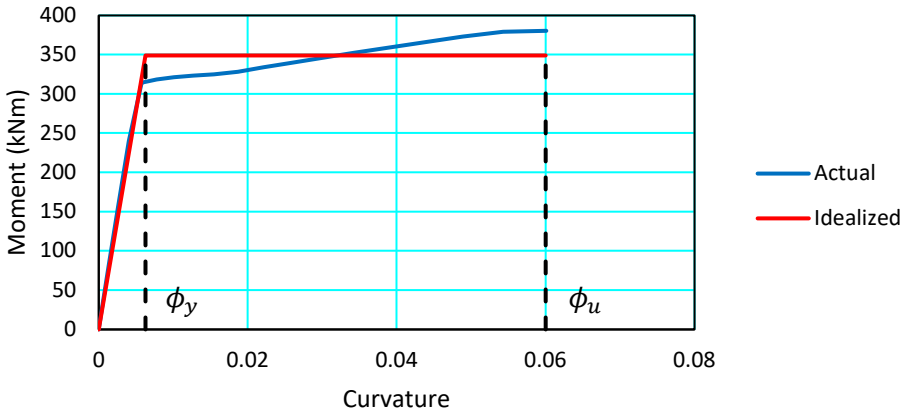

Figure 4.43 Moment-curvature for beam K117

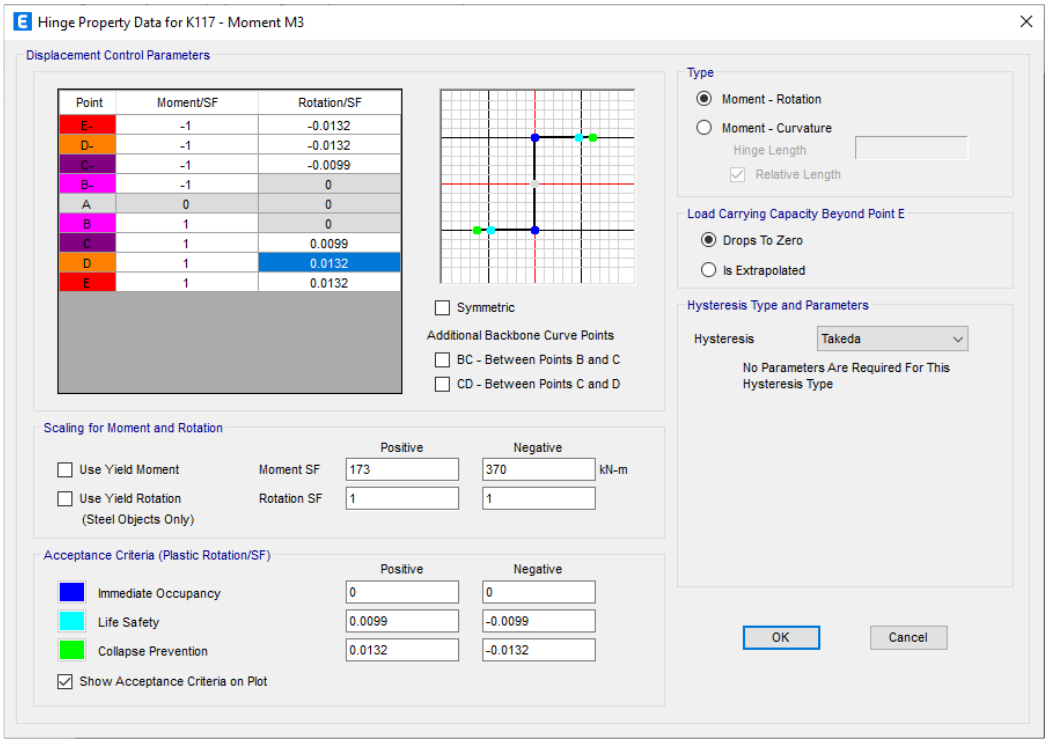

Figure 4.44 Nonlinear hinge model for beam K117.

Shear walls and columns were modeled with distributed plasticity. Shear wall and column sections were divided into fiber concrete and rebar elements. Figure 4.45 shows the fiber discretization for the shear wall P2-ED.

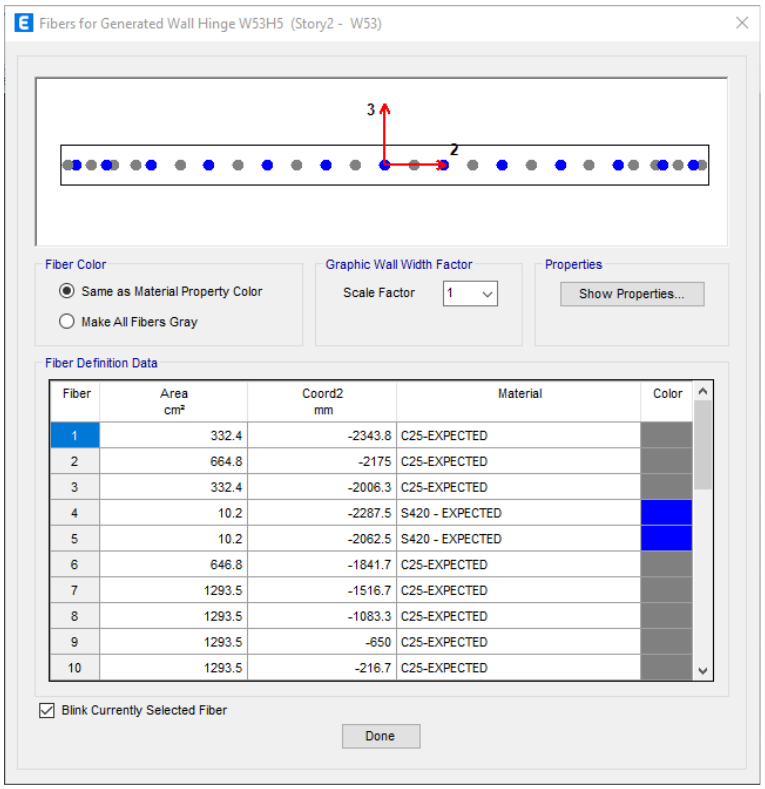

Figure 4.45 Fiber model definition for a shear wall.

Effective section rigidities to be used in lumped plasticity model for beams are calculated by

$$(EI)_e = \frac{My}{\theta_y}\frac{L_s}{3} \tag{4.22}$$

$$\theta_y = \frac{\phi_y L_s}{3} + 0.0015\eta\left(1 + 1.5\frac{h}{L_s}\right) + \frac{\phi_y\, d_b f_{ye}}{8\sqrt{f_{ce}}} \tag{4.23}$$

where My is the effective yielding moment of plastic hinge, θ_y is the yielding rotation of plastic hinge, L_s is the shear span of beams, which is half of the span, ϕ_y is the yield curvature of plastic hinge section, η=1 for columns and beams, h is the section height, and d_b is the average diameter of the longitudinal rebar. f_{ce} and f_{ye} are the expected concrete and steel strengths, respectively. Table 4.14 presents the effective section rigidities for second floor beams.

Table 4.14 Effective section rigidities for second floor beams.

Beams	ϕ_y (1/m)	My (kNm)	L (m)	L_s (m)	L_p (m)	d_b (mm)	θ_y (rad)	$(EI)_e$ (kNm^2)
K203	0.003	88	3.0	1.5	0.5	12	0.0046	9651
K204	0.003	88	3.0	1.5	0.5	12	0.0046	9651
K207	0.008	95	3.0	1.5	0.2	12	0.0069	6927
K209	0.005	78	4.5	2.3	0.3	14	0.0062	9491
K210	0.005	284	6.1	3.1	0.3	18	0.0084	34244
K211	0.006	268	3.3	1.6	0.3	18	0.0063	23006
K212	0.005	227	3.0	1.5	0.3	22	0.0062	18368
K214	0.005	286	4.5	2.3	0.3	16	0.0074	29112
K215	0.005	280	3.0	1.5	0.3	22	0.0063	22255
K216	0.003	271	6.0	3.0	0.5	16	0.0056	48016
K217	0.003	217	6.0	3.0	0.5	14	0.0056	38769
K219	0.005	155	6.0	3.0	0.3	16	0.0074	21033
K222	0.005	228	2.9	1.5	0.3	20	0.0061	18193
K223	0.005	228	5.7	2.9	0.3	20	0.0080	26939
K225	0.005	107	6.1	3.1	0.3	14	0.0075	14472
K226	0.005	155	5.5	2.8	0.3	16	0.0070	20229
K227	0.005	227	2.0	1.0	0.3	22	0.0058	13119
K228	0.006	250	5.7	2.9	0.3	16	0.0081	29379

4.3.2.6 Scaling of ground motions

Ground motions were scaled per the simple scaling method in AFAD [2018]. First, the SRSS for horizontal components of ground motions was calculated. Then, SRSS of ground motion was scaled such that the spectral acceleration values between $0.2T_p$ and $1.5T_p$ are larger than 1.3 times the corresponding earthquake level.

Figure 4.46 shows the scaling of ground motions to DD-1 and DD-3 earthquake levels. Single scale factors are 4.1 and 1.33 for the DD-1 and DD-3 earthquake levels, respectively.

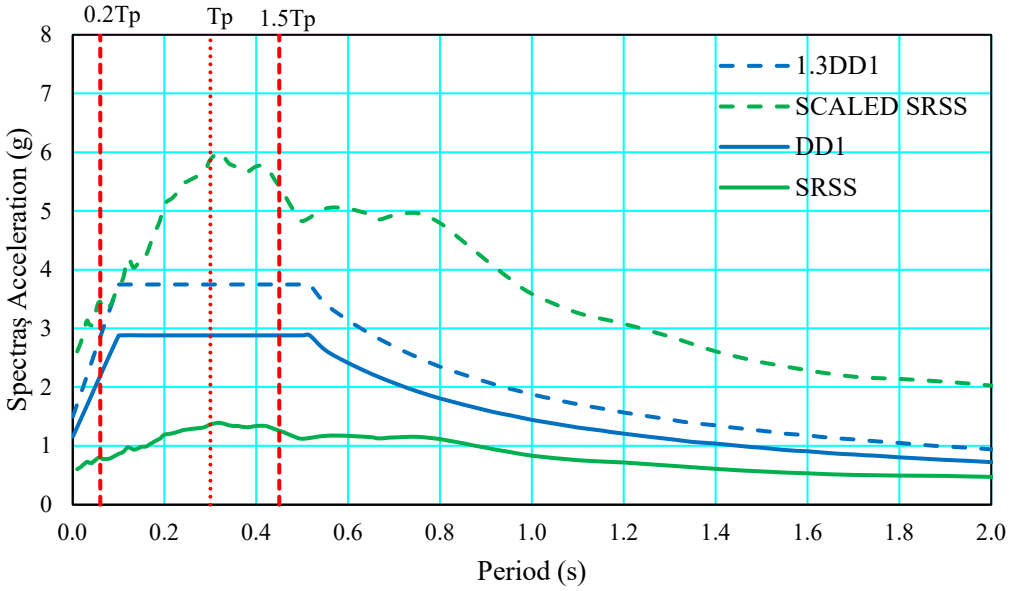

(a)

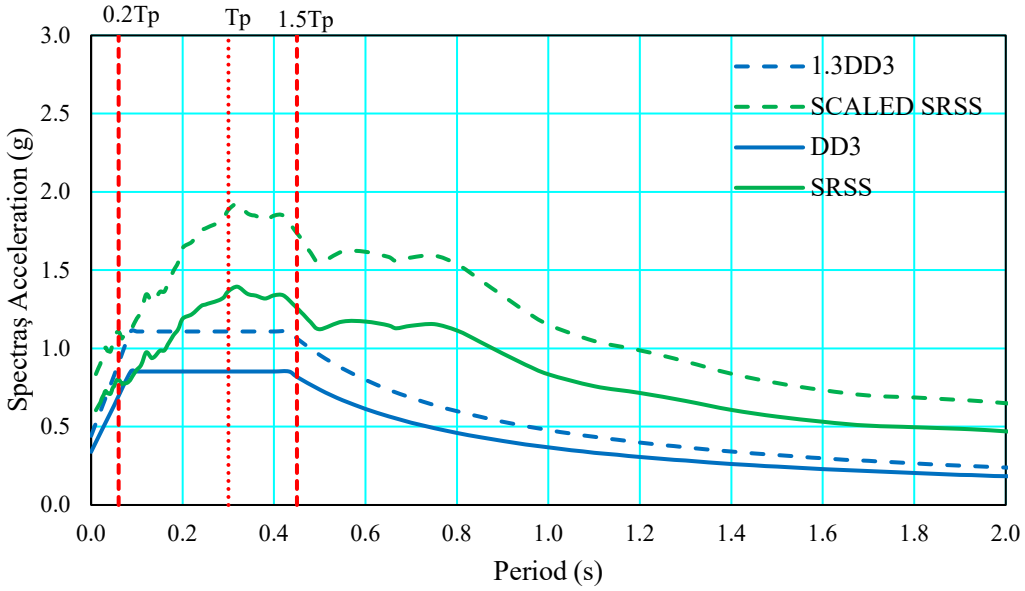

(b)

Figure 4.46 Scaling of ground motions to (a) DD-1 level earthquake and (b) DD-3 level earthquake.

4.3.2.7 Rayleigh damping

Rayleigh damping, which consists of mass- and stiffness-proportional damping matrices, was used for the NTHA:

$$\mathrm{C} = \mathrm{a}_0\mathrm{M} + \mathrm{a}_1\mathrm{K} \tag{4.24}$$

where M is the mass matrix, K is the stiffness matrix, a_0, and a_1 are the mass and stiffness coefficients, respectively. Hence, nth mode damping ratio ζ_n is

$$\zeta_n = \frac{a_0}{2}\frac{T_n}{2\pi} + \frac{a_1}{2}\frac{2\pi}{T_n} \tag{4.25}$$

where T_n is the natural vibration period. If it is assumed that ith and jth modes have the same damping ratios, a_0 and a_1 are calculated using

$$\mathrm{a}_0 = \xi_\mathrm{s}\frac{4\pi\frac{1}{T_iT_j}}{\left(\frac{1}{T_i}+\frac{1}{T_j}\right)}; \qquad \mathrm{a}_1 = \xi_\mathrm{s}\frac{1}{\pi\left(\frac{1}{T_i}+\frac{1}{T_j}\right)} \tag{4.26}$$

To have reasonable values of damping for the modes that contribute to the response, ith and jth modes shall be selected accordingly [Chopra 2012]. Table 4.15 presents the modal mass participation ratios for the first 12 modes. The first three modes are fundamental modes in Y, X, and torsional directions, respectively. When first three modes are considered, damping ratio values for these modes are close. However, for higher modes, damping ratios are overestimated. Second modes in Y, X, and torsional directions are the fourth, fifth, and sixth modes. These modes have 8-10% mass participation ratios. Rayleigh damping curve for first six modes is plotted in Figure 4.47. In this case, damping ratio values for the first six modes are estimated closely. Thus, this case was used in the damping modeling.

Table 4.15 Modal mass participation rations for the first 12 modes.

Mode	Period (s)	UX	SumUX	UY	SumUY	RZ	SumRZ
1	0.30	0.01	0.01	0.64	0.64	0.00	0.00
2	0.28	0.38	0.39	0.01	0.65	0.25	0.26
3	0.27	0.21	0.61	0.00	0.65	0.26	0.52
4	0.08	0.05	0.65	0.04	0.69	0.04	0.56
5	0.08	0.02	0.67	0.11	0.80	0.02	0.57
6	0.06	0.08	0.75	0.00	0.80	0.06	0.64
7	0.04	0.01	0.76	0.00	0.80	0.02	0.66
8	0.04	0.00	0.76	0.04	0.84	0.00	0.66
9	0.04	0.03	0.79	0.00	0.84	0.00	0.67
10	0.03	0.00	0.79	0.00	0.84	0.02	0.69
11	0.03	0.00	0.79	0.02	0.86	0.00	0.69
12	0.02	0.01	0.80	0.00	0.86	0.00	0.69

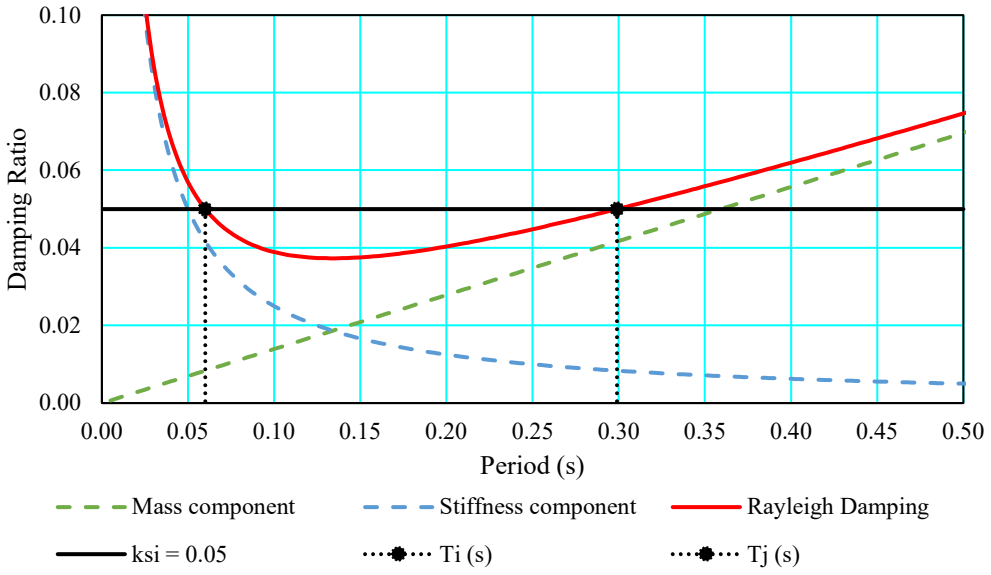

Figure 4.47 Rayleigh damping for the first six modes.

4.3.2.8 Results

In the NTHA, nonlinear direct integration was used. Time integration was performed by the Newmark's method. At the beginning of the analysis, nonlinear static analysis

was performed using $G + nQ + 0.3E^Z$ load case, where E^Z is the contribution of the vertical earthquake component:

$$E^Z = \left(\frac{2}{3}\right) S_{DS} G \tag{4.27}$$

S_{DS} values were 2.883 and 0.853 for the DD-1 and DD-3 earthquake levels, respectively. Consequently, $0.3E^Z$ was calculated as $0.577G$ and $0.171G$ for the DD-1 and DD-3 earthquake levels, respectively.

11 selected earthquakes have two perpendicular horizontal components. These acceleration records were applied simultaneously in the X and Y directions (case 1). Then, these records were rotated by 90° and the analysis was repeated (case 2). In total 2×11 load cases were defined for each earthquake level. In the assessment of the member, the average of 22 load cases was considered.

Table 4.16 and Table 4.17 present the maximum base shears under the DD-1 and DD-3 earthquake ground motions, respectively.

Table 4.16 Maximum base shears under the DD-1 earthquake ground motions.

Earthquake #	Case 1		Case 2	
	F_x (kN)	F_y (kN)	F_x (kN)	F_y (kN)
1	104000	67800	78600	82700
2	48700	39100	42800	46400
3	88300	65800	70700	63000
4	52200	68000	72700	52400
5	48400	75600	79800	50900
6	60800	43500	42500	72300
7	57800	63500	60900	57100
8	42700	43400	49900	43800
9	64300	74100	85500	77000
10	47600	17900	15500	45100
11	60100	44300	44900	54000

Table 4.17 Maximum base shears under the DD-3 earthquake ground motions.

Earthquake #	Case 1		Case 2	
	Fx (kN)	Fy (kN)	Fx (kN)	Fy (kN)
1	34900	35700	37400	40800
2	16200	16400	13400	21000
3	31500	42500	39900	40500
4	23100	24000	22100	23900
5	18700	31100	29500	20800
6	24100	21500	21300	31000
7	29600	27300	26900	33300
8	16800	20200	18900	20100
9	20300	24700	22700	21700
10	19100	9000	8600	25800
11	22200	14100	11800	23500

The averages of the maximum base shears in the X and Y directions are 60000 kN and 56500 kN, respectively, under the DD-1 earthquake ground motions. They are 23000 kN and 26000 kN, respectively, under the DD-3 earthquake ground motions. On the other hand, the elastic base shears are 100000 kN and 30000 kN for the DD-1 and DD-3 earthquakes, respectively.

Figure 4.48 summarizes the beam assessment for the DD-1 earthquake level. As more than 35% of the beams sustained advanced damage and several beams sustained collapse, the LS performance objective was not satisfied for the beams. Figure 4.49 summarizes the vertical member assessment for the DD-1 earthquake level. As several vertical members sustained collapse, the CP performance objective was not satisfied for the vertical members.

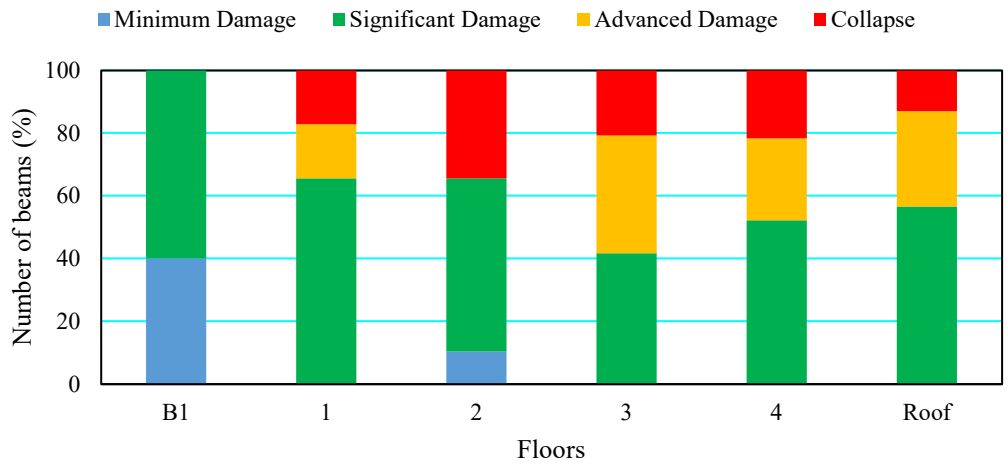

Figure 4.48 Post-retrofit building beam assessment for the DD-1 earthquake.

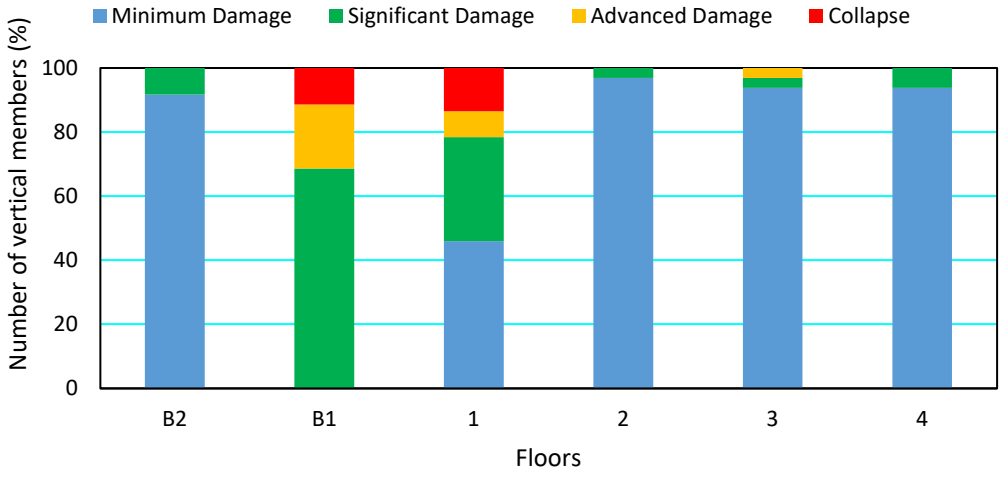

Figure 4.49 Post-retrofit building vertical member assessment for the DD-1 earthquake.

Figure 4.50 summarizes the beam assessment for the DD-3 earthquake level. As more than 20% of the beams sustained significant damage, the IO performance objective was not satisfied for the beams. Figure 4.51 summarizes the vertical member assessment for the DD-3 earthquake level. As several vertical members sustained significant damage, the IO performance objective was not satisfied for the vertical members.

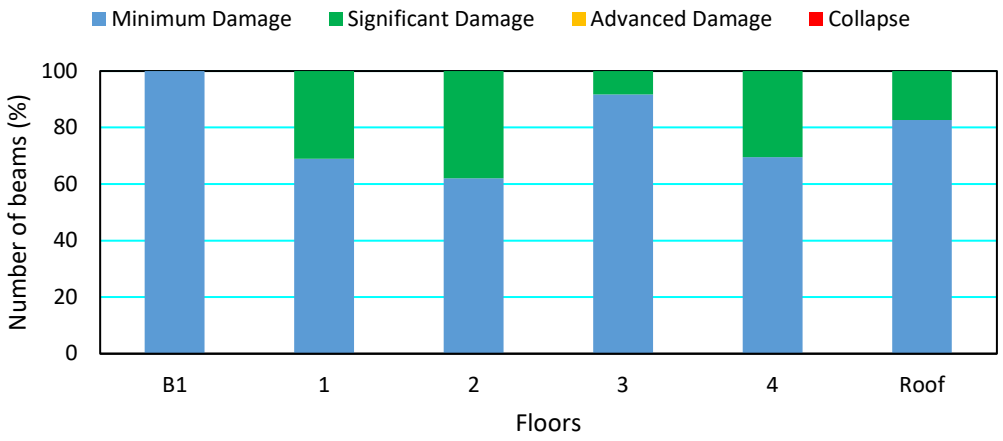

Figure 4.50 Post-retrofit building beam assessment for the DD-3 earthquake.

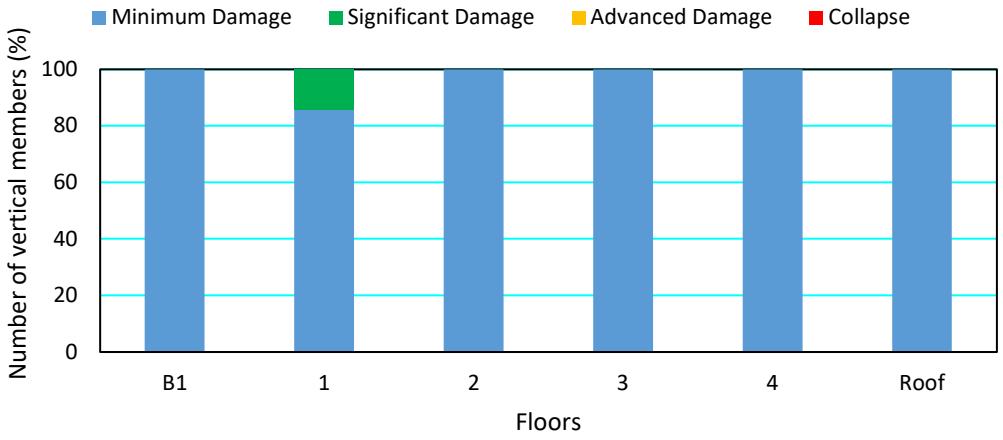

Figure 4.51 Post-retrofit building vertical member assessment for the DD-3 earthquake.

As IO and LS performance objectives were not satisfied, the post-retrofit building does not have adequate performance per AFAD [2018].

4.4 Summary

Seismic assessments for the as-built and post-retrofit states of the building were performed. For the as-built building, a rapid assessment was performed first and the building showed satisfactory performance. This method is based on the axial load ratios of vertical members and uses the DD-3 earthquake per AFAD [2018] with short-period and 1.0 s-period site coefficients of 1.0. Satisfactory performance in rapid assessment calls for an elaborate seismic risk assessment. Thus, a more detailed linear elastic method per MPWS [2007] was used in the assessment of the building. The IO performance objective was evaluated for the DBE level as defined in MPWS [2007]. Results have shown that the building did not satisfy the IO performance objective. Based on the analysis results under the DBE, the LS performance objective would not be satisfied under a higher earthquake level, i.e., the MCE. Hence, the retrofit decision for the as-built building was verified.

For the post-retrofit building, the linear elastic method per MPWS [2007] was performed first. The IO and LS performance objectives were not satisfied. Then, a nonlinear assessment was performed per AFAD [2018] using 11 earthquake ground motions scaled to the DD-3 and DD-1 earthquake levels. The post-retrofit building did not satisfy the IO and LS performance objectives.

CHAPTER 5

SUMMARY, DISCUSSIONS, CONCLUSIONS AND FUTURE RESEARCH

5.1 Summary

In this study, the finite element model of the first instrumented building in Turkey was updated using its dynamic properties that were previously identified from its in-situ dynamic tests [Gulkan et al. 1994; Celik and Gulkan 2021]. Then, seismic risk assessment of the building using past and current building codes in Turkey was performed. There were two different states of the building: the as-built and post-retrofit states. The as-built building had six stories above and two stories below the ground level and the overall height was 29.6 m. During the retrofit process, the top two stories were removed, and the building was strengthened by adding RC infill shear walls along both directions and shear walls around the elevator shaft. However, beams were not strengthened by any means. The overall height for the post-retrofit building was reduced to 22.4 m after strengthening. An ambient vibration test was performed on the as-built building, while a forced vibration test was performed in 2013 on the post-retrofit building.

For the as-built building, natural vibration periods determined from the finite element models with varying mass and stiffness properties were compared to those identified from the ambient vibration test. The finite element model with gross section properties, equivalent strut model coefficient of 0.27 and 2.4 kPa superimposed dead load had the closest natural vibration periods to those identified from the ambient vibration test. For the post-retrofit building, natural vibration periods, mode shapes, and acceleration-frequency response curves determined from the finite element model with varying mass and stiffness properties were compared to those identified from the forced vibration test. The finite element model with effective section stiffness multipliers for the DBE, equivalent strut model coefficient of 0.175 and 4.2

kPa superimposed dead load had the closest dynamic characteristics to those identified from the forced vibration test.

Subsequently, seismic risk assessment of the as-built building was performed first using the rapid assessment method per MEUCC [2021] and then using the linear method per MPWS [2007]. The rapid assessment method, which is based on the axial load ratios on the members, did not reveal inadequate performance about the building. However, the components of the structural system: shear walls, columns and beams, had inadequate seismic performance per the linear method. Moreover, the lateral stiffness of the building was inadequate to satisfy the lateral drift requirements. Thus, the linear method per MPWS [2007], which is based on the member demand-to-capacity ratios, revealed the inadequate performance of the as-built building. Performance objectives defined in MPWS [2007] were not satisfied. Thus, the retrofit decision for the as-built building was verified.

For the post-retrofit building, seismic risk assessment was performed first using the linear method per MPWS [2007]. Newly added RC infill shear walls were a lot stiffer than the existing moment frames. Hence, the seismic demand on the moment frames was reduced. The linear assessment method showed that the beams and columns had satisfactory performance, whereas the shear walls were inadequate. Then, a nonlinear assessment was performed using 11 selected earthquake ground motions per AFAD [2018]. Since the building is a dormitory, it has two advanced performance objectives: the IO performance objective under the DD-3 earthquake and the LS performance objective under the DD-1 earthquake. These performance objectives were not satisfied. Both the linear seismic assessment per MPWS [2007] and nonlinear seismic assessment per AFAD [2018] revealed that the post-retrofit building did not have satisfactory performance.

5.2 Discussions

- The calculations required in seismic risk assessment methods per MPWS [2007] and AFAD [2018] are overwhelming. The linear assessment method per MPWS [2007] requires the identification of ductile members, and the calculation of demand-to-capacity ratios and their limiting values. For these steps, expected axial load, shear and moment demands and capacities, reinforcement ratios and confinement need to be calculated for all structural members. The nonlinear assessment method per AFAD [2018] requires nonlinear material and member modeling, and effective section calculations. For these steps, nonlinear hinge rotation, concrete and steel strain demands and capacities, and moment-curvature relations need to be calculated for all structural members. For the building investigated in this study, most of the members had different section dimensions and reinforcement configurations. Thus, it was challenging to perform all these calculations.
- The scaling factors of 11 selected ground motions were controlled by the 0.1 s corner period of the target spectrums, which resulted in spectral acceleration values at fundamental periods to be calculated about 50% more than the target spectrum values (see Figure 4.46).
- During the retrofit, RC infill shear walls were added to the structural system and the top two stories were removed. The building became considerably stiffer and hence the seismic demand on the building was increased significantly.
- Beams and slabs were not retrofitted by any means. 10 cm thick slab was thin to provide the rigid diaphragm behavior.

5.3 Conclusions

Two different superimposed dead loads were considered for the finite element model calibrations. A smaller superimposed dead load provided more accurate results for the as-built building. On the contrary, a larger superimposed dead provided more

accurate results for the post-retrofit building. Architectural drawings for the post-retrofit building showed that floor and wall covers were added. Thus, having a larger superimposed dead load for the post-retrofit state was verified.

The finite element model of the as-built building with gross section properties resulted in closer natural vibration periods to those identified from the ambient vibration test. On the contrary, the finite element model of the post-retrofit building with effective section stiffness multipliers resulted in closer natural vibration periods, mode shapes, and acceleration-frequency responses to those identified from the forced vibration test. The contribution of the partition walls to the stiffness of the as-built building, where the structural system was more flexible, was more than that in the post-retrofit building, where the structural system was stiffer because of the added RC shear walls.

The DBE defined in MPWS [2007] is equivalent to the DD-2 earthquake defined in AFAD [2018]. When the response spectra for these two earthquake levels that are associated with the same hazard level, 10% PE in 50 years, are compared in Figure 4.1, it can be seen that earthquake loads were considerably increased in AFAD [2018].

During the retrofit of the building, the top two stories were removed and the structural system was strengthened by adding RC infill shear walls. This intervention increased the stiffness of the building significantly and thus, the building would be subjected to a higher seismic load when compared to its as-built state. This is because the fundamental periods were moved to the flat portion of the response spectrum for the post-retrofit state of the building.

The IO performance objective in MPWS [2007] allows 10% of the beams to sustain significant damage, whereas 20% of the beams are allowed to sustain significant damage in AFAD [2018]. Both codes require that all other members sustain minimum damage. The assessment was performed for the DBE and DD-3 earthquake in MPWS [2007] and AFAD [2018], respectively. Hence, the IO performance objective defined in AFAD [2018] is less strict than that is defined in MPWS [2007].

The LS performance objective in MPWS [2007] allows 30% of the beams and 20% of the columns to sustain advanced damage and all the shear walls to sustain significant or minimum damage. On the other hand, AFAD [2018] allows 35% of the beams, 20% of the columns and shear walls to sustain advanced damage. The assessment was performed for the MCE and DD-1 earthquake in MPWS [2007] and AFAD [2018], respectively. When the response spectra for the MCE and DD-1 earthquake levels that are associated with the same hazard level, 2% PE in 50 years, are compared in Figure 4.1, it can be seen that the spectral acceleration values at the flat portion of the DD-1 response spectrum are about twice of the MCE response spectrum. Hence, the LS performance objective defined in AFAD [2018] is more strict than that is defined in MPWS [2007].

In the as-built building, there were no confinement zones at the critical ends of the structural members. Moreover, the longitudinal and shear reinforcement amounts were low. Thus, most of the structural members had low ductility and poor seismic detailing.

The average of the maximum base shears under the DD-1 earthquake ground motions is about half of the elastic base shears from elastic analysis (R = 1). Figure 4.48 and Figure 4.49 summarize the linear seismic assessment for the DD-1 earthquake, which predicted major nonlinearity in structural members. Thus, smaller base shears calculated in the nonlinear assessment were verified.

The average of the maximum base shears under the DD-3 earthquake ground motions is close to the elastic base shears from elastic analysis (R = 1). Figure 4.50 and Figure 4.51 summarize the linear seismic assessment for the DD-3 earthquake, which predicted minor nonlinearity in structural members. Thus, similar base shears calculated in the nonlinear assessment were verified.

5.4 Future Research

The following tasks are suggested for future research based on the scope and limitations of this work:

- Perform seismic assessment using a finite element model where the contribution of the partition walls is accounted for.
- Perform seismic assessment per ASCE standards, where nonlinear hinge parameters are different, and compare the results with AFAD [2018].
- Use spectral matching in scaling the earthquake ground motions to the design spectrum as defined in AFAD [2018].

REFERENCES

AFAD [2018] Turkish Building Earthquake Code 2019, Official Gazette, No: 30364 (in Turkish). Ankara, Turkey.

AFAD-TADAS [2018] Seismic hazard maps of Turkey. Disaster and Emergency Management Authority, Ankara, Turkey. https://tadas.afad.gov.tr. Accessed 10 August 2022.

Aldemir A, Binici B, Canbay E, Yakut A [2017] Lateral load testing of an existing two story masonry building up to near collapse. *Bulletin of Earthquake Engineering*, 15: 3365–3383.

ASCE [2007] Seismic Rehabilitation of Existing Buildings, ASCE standard ASCE/SEI 41-06, American Society of Civil Engineers, Reston, Virginia.

Asteris PG [2003] Lateral stiffness of brick masonry infilled plane frames. *Journal of Structural Engineering*, 129(8): 1071–1079.

Asteris PG, Antoniou ST, Sophianopoulos DS, Chrysostomou CZ [2011] Mathematical macromodeling of infilled frames: State of the art. *Journal of Structural Engineering*, 137(12): 1508–1517.

Beolchini GC, Vestroni F [1997] Experimental and analytical study of dynamic behaviour of a bridge. *Journal of Structural Engineering*, 123(11): 1506–1511.

Celep Z [2014] Structural Dynamics (in Turkish) Beta Publication.

Celik OC [2016] Effect of AAC infill walls on structural system dynamics of a concrete building. *Journal of Earthquake Engineering*, 20(5): 738–748.

Celik OC, Gulkan HP [2021] Processing forced vibration test records of structural systems using the analytic signal. *Journal of Vibration and Control*, 27(19–20): 2253–2267.

Celik OC, Sucuoglu H, and Akyuz U [2015] Forced vibration testing and finite element modeling of a nine-story reinforced concrete flat plate-wall building.

Earthquake Spectra, 31(2): 1069–1081.

Chaker AA, Cherifati A [1999] Influence of masonry infill panels on the vibration and stiffness characteristics of R/C frame buildings. *Earthquake Engineering and Structural Dynamics*, *28*(9): 1061–1065.

Chopra, AK [2012] Dynamics of Structures, Prentice Hall, Upper Saddle River, New Jersey.

Chrysostomou CZ, Asteris PG [2012] "On the in-plane properties and capacities of infilled frames," *Engineering Structures* 41, 385–402

Ciongradi A [1983] Cours de GeHnie Parasismique, Earthquake Engineering Training Course, Organisme de Contro (leTechnique de la Construction, Alger, Algeria

Clinton JF, Bradford SC, Heaton TH, Favela J [2006] The observed wander of the natural frequencies in a structure. *Bulletin of the Seismological Society of America*, 96(1): 237–257.

Computers and Structures, Inc. [2019] ETABS, Walnut Creek, California.

Computers and Structures, Inc. [2020] SAP2000, Walnut Creek, California.

El-Dakhakhni WW, ElgaalyM, Hamid AA [2003] Three-strut model for concrete masonry-infilled frames. *Journal of Structural Engineering*, 129(2): 177–185.

El-Dakhakhni WW, Hamid AA, Hakam ZHR, Elgaaly M [2006] Hazard mitigation and strengthening of unreinforced masonry walls using composites. *Compos. Struct*., 73(4): 458–477.

Genes MC, Bikce M, Kacin S, Akyuz U, Gulkan HP, Abrahamczyk L, Schwarz J [2008] Building Monitoring for Seismic Risk Assessment (II): Instrumental Testing of RC Frame Structures and Analytical Reinterpretation of Response Characteristics. *Proceedings of the 14th World Conference on Earthquake Engineering*, Paper no: 09-01-0173, Beijing, China.

Guler K, Yuksel E, Kocak A. [2008] Estimation of the fundamental vibration period of existing RC buildings in Turkey utilizing ambient vibration records. *Journal of Earthquake Engineering*, 12(S2): 140–150.

Gulkan HP, Sucuoglu H, Sonuvar O, Incekaya CO, Baulke N, Mengi Y [1994] Analysis of Instrumented Building Response to Strong Ground Motions at Very Short Distances to the Causative Fault. Project no. INTAG 506 (YAG-40). Ankara, Turkey: The Scientific and Technical Research Council of Turkey.

Hashemi A, Mosalam KM [2007] Seismic evaluation of reinforced concrete buildings including effects of masonry infill walls. PEER Report 2007/100, Pacific Earthquake Engineering Research Center, University of California, Berkeley, California.

Hudson DE [1970] Dynamic tests of full-scale structures. In: Wiegel, R.L., editor. Earthquake engineering. Englewood Cliffs, NJ: Prentice Hall, p. 127–149 (chap. 7).

Jackson J, McKenzie D [1984] Active Tectonics of the Alpine-Himalayan Belt between Western Turkey and Pakistan. *Geophysical Journal International*, 77: 185–264.

Mainstone RJ [1974] Supplementary note on the stiffnesses and strengths of infilled frames, CP 13/74, *Building Research Station*, Garston, United Kingdom.

Mander JB, Priestley MJN, Park R [1988] Theoretical Stress-Strain Model for Confined Concrete. *Journal of Structural Engineering-Asce*, *114*(8), 1804–1826

MEUCC [2021] Draft version of Law on Transformation of Areas under Disaster Risk. Official Gazette, Ministry of Environmental, Urbanization and Climate Change, Ankara, Turkey.

Mosalam KM [1996] Modeling of the nonlinear seismic behavior of gravity load designed frames. *Earthquake Spectra*, 12(3): 479–492.

MPWS [1975] Specification for Buildings to be Built in Seismic Zones, Ministry of Public Works And Settlement, Ankara, Turkey.

MPWS [2007] Specification for Buildings to be Built in Seismic Zones, Ministry of Public Works and Settlement, Ankara, Turkey.

Pan TC, You X, Brownjohn JMW [2006] Effects of infill walls and floor diaphragms on the dynamic characteristics of a narrow-rectangle building. *Earthquake Engineering and Structural Dynamics*, *35*(5): 637–651.

PEER [2022] Strong motion database [10 October 2022].

Soyoz S, Taciroglu E, Orakcal K, Nigbor R, Skolnik D, Lus H, Safak E [2013] Ambient and forced vibration testing of reinforced concrete building before and after its seismic retrofitting. *Journal of Structural Engineering*, 139(10): 1741–1752.

Stafford Smith B, Carter C [1969] "A method of analysis for infilled frames," *ICE Proceedings* 44(1), 31–48.

Sucuoglu H, Akkar S [2014] Basic Earthquake Engineering from Seismology to Analysis and Design. *Springer International Publishing*.

Tahar [1984] Interaction entre ossature en behton armeh et maionnerie de briques creuses sous sollicitations de type sismique. Docteur-IngeHnieur thesis, Ecole Nationale des Ponts et ChausseHes, Paris.

Takeda T, Sozen MA, Neilsen NN [1970]. Reinforced concrete response to simulated earthquakes. *ASCE J. Struct*. Div., 96(12): 2557–2573.

Tiruvengadam V [1985] On the natural frequencies of infilled frames. *Earthquake Engng. Struct. Dyn.*, 13.

Trifunac MD, Todorovska MI [1999] Recording and interpreting earthquake response of full-scale structures. *Proc. NATO Workshop on Strong Motion Instrumentation for Civil Engineering Structures*, 2–5 June, Istanbul, Turkey.

Kluwer.

Turkish Standards Institute [1997] Design Loads for Buildings, TS 498, Ankara, Turkey.

Turkish Standards Institute [2000] Requirements for Design and Construction of Reinforced Concrete Structures, TS 500, Ankara, Turkey.

Vestroni F, Beolchini GC, Antonacci E, Modena C [1996] Identification of dynamic characteristics of masonry buildings from forced vibration tests. *Proceedings of the 11th World Conference on Earthquake Engineering.*

APPENDIX A

BEAM SIZES

In the reference documents, beam sizes for basement floor were not provided. Thus, for first basement level beam sizes was assumed to be same with the one on first level.

Table A1. Beam sizes.

Beam ID	Section Dimensions	
	b_w (mm)	h (mm)
K102	200	600
K105	350	600
K106	200	600
K107	200	600
K108	300	600
K109	300	600
K110	300	900
K111	300	900
K113	300	600
K114	200	800
K115	200	600
K116	300	600
K117	300	600
K118	200	600
K119	200	600

Table A1. Beam sizes (continued).

Beam ID	Section Dimensions		Beam ID	Section Dimensions	
	b_w (mm)	h (mm)		b_w (mm)	h (mm)
K203	300	1000	K301	200	550
K204	200	1000	K302	300	550
K205	200	600	K303	300	550
K206	300	600	K304	300	550
K207	300	400	K305	200	600
K208	300	550	K306	200	600
K209	200	600	K307	200	600
K210	200	800	K308	200	600
K211	200	800	K311	300	550
K212	200	600	K313	300	550
K214	200	600	K314	300	900
K215	200	600	K315	300	550
K216	300	900	K316	200	800
K217	300	900	K317	200	800
K218	300	600	K318	200	550
K219	300	600	K319	200	550
K220	300	600	K320	200	600
K221	200	600	K321	200	550
K222	200	600	K322	200	550
K223	200	600	K323	200	550
K225	200	600	K324	200	550
K226	300	600	K325	200	600
K227	200	600	K328	200	550
K228	200	600	K329	200	550
K230	200	600			

Table A1. Beam sizes (continued).

Beam ID	Section Dimensions		Beam ID	Section Dimensions	
	b_w (mm)	h (mm)		b_w (mm)	h (mm)
K401	200	550	K501	200	550
K402	300	550	K502	300	550
K403	300	550	K503	300	550
K404	300	550	K504	300	550
K405	200	600	K505	200	600
K406	200	800	K506	200	800
K407	200	600	K507	200	600
K408	600	400	K508	600	400
K410	200	600	K510	200	600
K411	200	600	K511	200	600
K412	200	800	K512	200	800
K413	200	800	K513	200	800
K414	300	550	K514	300	550
K415	300	550	K515	300	550
K416	200	800	K516	200	800
K417	200	800	K517	200	800
K418	200	600	K518	200	600
K419	200	600	K519	200	600
K420	300	600	K520	300	600
K421	200	600	K521	200	600
K423	200	800	K523	200	800

Table A1. Beam sizes (continued).

Beam ID	Section Dimensions		Beam ID	Section Dimensions	
	b_w (mm)	h (mm)		b_w (mm)	h (mm)
K601	200	550	K701	200	550
K602	300	550	K702	300	550
K603	300	550	K703	300	550
K604	300	550	K704	300	550
K605	200	600	K705	200	800
K606	200	800	K706	200	600
K607	200	600	K707	600	400
K608	600	400	K708	200	800
K610	200	600	K709	200	800
K611	200	600	K710	700	550
K612	200	800	K711	200	800
K613	200	800	K712	200	600
K614	300	550	K713	200	600
K615	300	550	K714	200	1000
K616	200	800			
K617	200	800			
K618	200	600			
K619	200	600			
K620	300	600			
K621	200	600			
K623	200	800			